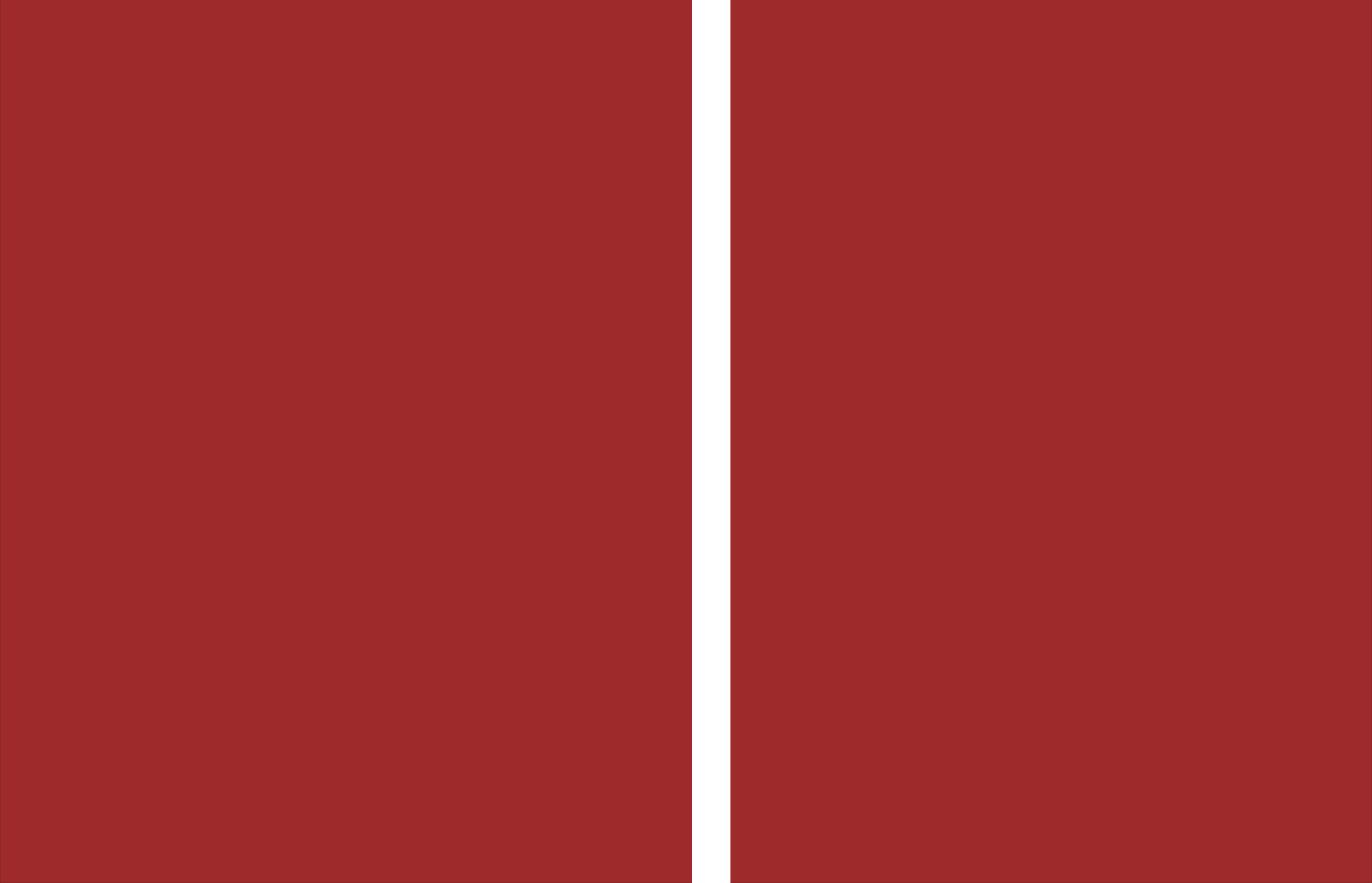Veniero Lenzi
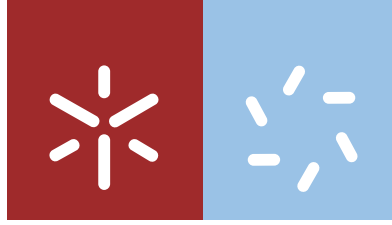
Multiscale modelling and simulation of soft matter systems

Veniero Lenzi   Multiscale modelling and simulation of soft matter systems

UMinho | 2020

maio de 2020

Universidade do Minho
Escola de Ciências

Veniero Lenzi

**Multiscale modelling and simulation
of soft matter systems**

Tese de Doutoramento
Doutoramento em Ciências
Especialidade em Física

Trabalho efetuado sob a orientação do
Professor Doutor Luís Silvino Alves Marques
e da
Professora Doutora Marta Maria Duarte Ramos

maio de 2020

DIREITOS DE AUTOR E CONDIÇÕES DE UTILIZAÇÃO DO TRABALHO POR TERCEIROS

Este é um trabalho académico que pode ser utilizado por terceiros desde que respeitadas as regras e boas práticas internacionalmente aceites, no que concerne aos direitos de autor e direitos conexos.

Assim, o presente trabalho pode ser utilizado nos termos previstos na licença abaixo indicada.

Caso o utilizador necessite de permissão para poder fazer um uso do trabalho em condições não previstas no licenciamento indicado, deverá contactar o autor, através do RepositóriUM da Universidade do Minho.

Licença concedida aos utilizadores deste trabalho

Acknowledgements

I am deeply grateful to my supervisors, prof. Luís S. A. Marques and prof. Marta M. D. Ramos, not only for their continuous support, guidance and stimulus, but also for giving me the opportunity to start a PhD program in Portugal, and to get in touch with this beautiful country and its people. Through an ITN grant, I had the unique opportunity to meet many capable colleagues and scientists, and I thank them all for those exciting years. I also acknowledge the fundamental role of Piet Driest and dr. Dirk Dijkstra, from Covestro Deutschland AG, which performed the experiments mentioned in this thesis and always fostered stimulating discussions and new ideas. I'm very grateful to the members of the computational and theoretical physics laboratory of university of Minho. I hope I could give back to them all the support and kindness that I've received in these years.

Statement of integrity

I hereby declare having conducted this academic work with integrity. I confirm that I have not used plagiarism or any form of undue use of information or falsification of results along the process leading to its elaboration. I further declare that I have fully acknowledged the Code of Ethical Conduct of the University of Minho.

Resumo

Modelação e simulação multiescalar de sistemas de matéria mole   *Veniero Lenzi*

Esta tese é dedicada à simulação e modelação de poliisocianatos alifáticos, uma família de moléculas de reticulação usada na produção de poliuretanos. O seu uso é limitado pela sua elevada viscosidade, e entender a origem deste facto é essencial para sintetizar poliisocianatos de baixa viscosidade, permitindo processos mais sustentáveis com um uso reduzido de compostos químicos e solventes. O conhecimento fundamental sobre a viscosidade desta família molecular é escasso, e uma ampla gama de técnicas de simulação, abrangendo diferentes escalas, é utilizada para preencher essa lacuna.

Um campo de força clássico para isocianatos foi desenvolvido e testado para permitir simulações de dinâmica molecular fiáveis da fase líquida. Os resultados da simulação reproduzem de forma excelente as viscosidades experimentais de poliisocianatos e sugerem a presença de interações peculiares entre anéis de isocianurato e os grupos isocianato, sendo possivelmente responsáveis pela origem da viscosidade dos poliisocianatos.

A presença e o papel dessas interações são investigados usando uma ampla gama de métodos ab initio e de dinâmica molecular, revelando que os anéis de isocianurato são realmente capazes de fortes ligações não covalentes e que a interação isocianato-isocianurato é responsável pelo aumento viscosidade dos poliisocianatos. Este resultado encorajou a exploração da possibilidade de usar isocianuratos para a funcionalização não covalente de materiais 2D, e resultados promissores foram obtidos.

Foi feita a simulação da formação de redes poliméricas reticuladas usando cadeias funcionalizadas nos extremos com isocianatos, usando o método da dinâmica de partículas com dissipação, conjugado com a modelação da reação de reticulação. Estudou-se as propriedades topológicas e capacidade de dilatação destas redes, demonstrando-se que esta nova abordagem permite obter redes poliméricas reticuladas cujas propriedades são muito próximas às obtidas com métodos tradicionais de processamento.

Esta tese clarifica a ligação existente entre interações moleculares e as propriedades macroscópicas dos poliisocianatos, revelando o mecanismo responsável pelo comportamento da viscosidade dos poliisocianatos e fornecendo, ao mesmo tempo, ferramentas de simulação eficazes para o estudo futuro de materiais baseados nesta família de moléculas.

Palavras-chave: dinâmica molecular, métodos ab initio, poliisocianatos, viscosidade.

Abstract

Multiscale modelling and simulation of soft matter systems   *Veniero Lenzi*

This thesis is devoted to the simulation and modelling of aliphatic polyisocyanates, a family of crosslinking molecules which is the basic building block of polyurethane materials. Their use is limited by their high viscosity, and understanding its origin is fundamental to devise low-viscosity polyisocyanates, allowing for more sustainable processes with a reduced use of chemical compounds and solvents. Up to now, this knowledge was missing, and a wide range of simulation techniques, embracing different scales, is employed here to fill this gap.

A classical force field for isocyanates is developed and tested to enable reliable liquid phase simulations using all-atom molecular dynamics. Simulation results reproduce very well the experimental viscosities of polyisocyanates and suggest the presence of peculiar interactions between isocyanurate rings and isocyanate groups, possibly involved in determining the isocyanates' viscosity.

The presence and role of these interactions is investigated using a wide range of ab initio methods and molecular dynamics free energy estimations, revealing that isocyanurate rings are indeed capable of strong non-covalent bindings, and that the isocyanate-isocyanurate interaction is responsible for the increased viscosity of polyisocyanates. Encouraged by this, we explore the possibility of using isocyanurates for non-covalent functionalization of 2D materials, and promising results are shown.

Dissipative particle dynamics simulations, conjugated with a crosslinking reaction modelling, are employed to simulate the formation of polymer networks using isocyanate end-functionalized chains and study their swelling and topological properties. It is demonstrated that using the end-functionalized chains approach provides networks with properties very close to those obtained with traditional processing routes.

This thesis clarifies the connection between molecular interactions and macroscopic properties of polyisocyanate systems, revealing the mechanism responsible of viscosity behaviour of polyisocyanates and providing, at the same time, effective simulation tools for further research.

Keywords: ab initio methods, molecular dynamics, polyisocyanates, viscosity.

Contents

List of Figures

List of Tables

Chapter 1

Introduction

This chapter is devoted to the review of present experimental and theoretical research on isocyanates and polyisocyanates, with a focus on aliphatic ones. The first section introduces the isocyanates and derived molecules, as well as their reactivity. The following one illustrates their role in current research, spanning several disciplines of chemistry and physics. Next, an overview of computational studies is presented, highlighting those areas in which the literature is scarce and further work is welcome. Finally, the aim and scopes of the present thesis are introduced, along with a description of the main case study considered.

1.1   Isocyanates and polyisocyanates

Isocyanates are a well known family of molecules, firstly synthesized in the middle of ninetieth century by C. A Wurtz [1]. Many years later, in 1932, Otto Bayer discovered a method to produce polyurethanes (PU) [2], which uses isocyanates as a basic building block. Since then, their use exploded due to the unique versatility of PU materials and nowadays they are employed in a very diverse range of applications, from construction blocks to coatings for cars, planes and satellites, from flame retardants to biomaterials [3, 4, 5], to thermal shielding for heavy-lift launch vehicles [6], and their global production is nevertheless expected to steadily rise in the next years [7].

All isocyanates possess the very active isocyanate group, capable to react with several chemical groups [8, 4]. In general, they react quickly at mild conditions with all types of nucleophiles. The most renown reaction is certainly the urethane formation, occurring when an isocyanate reacts with an alcohol group, forming an urethane linkage. Similarly, an NCO group can strongly react with amine groups, in which case an urea linkage is formed instead. Moreover, they strongly react with water, which decompose the NCO group into an amine, with the release of gaseous carbon dioxide. Isocyanates are usually classi-

fied depending on the nature of the molecule that carries them: aromatic isocyanates contains aromatic groups, such as toluene or diphenyl diisocyanates, while aliphatic isocyanates contains only alkyl chains, such as the hexamethylene diisocyanate.

The functionality ν is defined as the number of NCO groups in an isocyanate. $\nu > 2$ isocyanates, namely $\nu = 3$, are used as crosslinkers and are obtained through the cyclotrimerization of di-isocyanates. As suggested by the name, this process results in the formation of a ring structure, termed isocyanurate. Aliphatic isocyanurates are particularly appealing, since they show excellent thermal and chemical stability [9], and their presence in PUs confers them flame-retardant properties, as well as improved mechanical properties. In addition, they have a high resistance to degradation by environmental factors. Clearly, mono-functional isocyanates could also undergo cyclotrimerization, but the final molecule would have no functionality, bearing little interest for further applications.

The ring formation is known to occur spontaneously, although slowly. Beside this, isocyanates could also dimerize, resulting in the formation of a difunctional uretdione. These reactions are responsible for the relatively low shelf lifetimes of isocyanates [8]. In the production of isocyanurate crosslinkers, uretdiones generally constitute unwanted byproducts. Moreover, the cyclotrimerization will produce higher functionality isocyanurates, in a measure proportional to the reaction time [10]. A wide range of catalysts might be employed to accelerate the cyclotrimerization, such as Lewis bases, rare earth and main group complexes [4].

1.2   Applications and current research trends

Despite the long-time knowledge and application of isocyanate, the research on them still is a vibrant field across several areas, ranging from advanced materials development to astrophysics and astrochemistry.

When aliphatic isocyanates and isocyanurates are employed, materials with better properties are generally obtained, when compared with other families. They are at the basis of high-performance coatings [11, 12, 13] and porous materials [14] with excellent mechanical properties. Moreover, it has been demonstrated that trimer-based materials could display a room-temperature activated shape-memory effect [15]. Further, it was shown that isocyanate trimers could be used to form a stable matrix for non liner optically (NLO) active devices [16]. Due to the superior performance they are able to confer to the final material, aliphatic isocyanurates are also at the basis of bio-based polyurethane coatings made using starch as a polyol [17].

Environmental and sustainability concerns are finally coming into a more general attention, therefore

research efforts are directed towards the development and definition of processes that consume less water and potentially polluting chemical compounds, and on the search of renewable, petrol-free, sources for the reactants. Regarding this, it was recently shown that aliphatic isocyanates could be obtained through green chemistry routes [18] and in 2015 [19] the first commercial bio-based aliphatic polyisocyanate product was introduced in the market. In the same line, the search of more efficient and better isocyanurate production routes represents a very active field. Ideal catalysts should have a high efficiency and good activity at mild conditions, conjugated with low formation rates of uretdiones. Very promising catalysts have been recently found, including complexes containing transition metals [20, 21] and first group elements [22, 23], and olefins [24].

From a more general point of view, the unique chemistry and reactivity of isocyanates makes them very appealing for advanced applications, such as the functionalization of surfaces and nanocarriers [25, 26, 27], immobilization of proteins [28]. In these applications, the strong reactivity of isocyanates is exploited to covalently attach isocyanate-functionalized molecules to a substrate, resulting e.g. in the grafting of fluorinated polymers to a silica surface, providing anti-fogging and anti-moisture protection. In the same way, isocyanates can be used to modify the surface of cellulose and nano-cellulose [29]. Hexamethylene diisocyanate has been used to create cathode protective layers in lithium ion batteries, improving their performance stability [30, 31, 32]. Although not really capable of click chemistry reactions [33] because of the isocyanate group poor selectivity, they are effectively applied in a similar, click-like, fashion for the design of complex surfaces through post-polymerization [34], synthesis of artificial proteins [35].

Remarkably, isocyanates have also an important role in the processing of graphene-based materials. They are used to functionalize graphene oxide [36] in order to exfoliate it and make it more soluble. Moreover, isocyanate-functionalized graphene oxide was used to craft flexible energy storage devices [37] and nanocatalysts [38]. An aliphatic isocyanate trimer reinforced graphene aerogel has been synthesized, showing good adsorption properties towards crude oil [39], with potential application for storage and clean-up of organic pollutants.

A very interesting class of materials is constituted by PU-based hydrogels, which possess attractive properties as biomaterials, due to their intrinsic versatility [40] and biocompatibility [5]. In this regard, it has been shown that they can be obtained by employing a cyclotrimerization as crosslinking reaction of aliphatic isocyanate-functionalized polyethylene glycol and polycaprolactone chains [41], yielding a cros-slinked material with a very well-defined network structure, as well as improved mechanical properties, especially in the swollen state. PU-based microgels, that is polymer networks of micrometer scale dimensions [42], have been synthesized and used for several biomedical applications, such as targeted drug

delivery [43, 44, 45], vascular embolization [46], improving lifespan of shape memory biomaterials [47].

Isocyanate microcapsules [48] constitute another interesting example of isocyanate-based microstructures, and are used to produce smart coatings with self-healing and self-lubricating capabilities. These microcapsules contain unreacted isocyanates in their core that are released upon breaking and allowed to react with the surrounding material. Their use is particularly fit for coatings exposed to wet environments, due to the water-isocyanate reaction. Aliphatic [49] and non aliphatic isocyanates [50, 51, 52] have been used for this purpose, showing excellent performance. Other uses of isocyanate microcapsules comprise functional crosslinking agents in wood adhesives [53], due to their improved stability and controlled release of isocyanate content.

The use of isocyanates for advanced materials is expected to grow as new synthesis routes [54, 55, 41] and novel processing and handling techniques, such as molecular layer deposition [56], are continuously developed. The possibility of employing isocyanates in reactive inkjet 3D printing processes has also been investigated [57].

Finally, it is worth mentioning how the research on aliphatic isocyanates is recently blooming in the astrophysical community, following the discovery of methyl isocyanate on the comet 67P/Churyumov–Gerasimenko by the Philae lander of the Rosetta spacecraft [58]. It was further identified through spectroscopic observation in interstellar medium and protostar gas clouds [59], and there is evidence regarding the presence of ethyl isocyanate as well. Isocyanates play a very important role in prebiotic chemical reactions as building blocks of more complex peptides [60], several recent studies are aimed at understanding their formation and stability under astrophysical conditions [61, 62]. It was shown that methyl isocyanate/water mixtures could form stable ices at temperatures up to 20 K.

1.3   Theoretical and modelling studies

Literature regarding theoretical, modelling and simulation studies of aliphatic isocyanates from the atomistic point of view is not as vast as expected from their importance. Isocyanate ion (NCO^-)and isocyanic acid ($HNCO$) have been thoroughly studied using quantum mechanical calculations, but the same does not hold for more complex isocyanates and polyisocyanates, especially aliphatic ones. Additionally, most of the computational works on complex isocyanates are targeted towards understanding the chemical reactions of isocyanates, rather than their interactions in gas and condensed phase. Therefore, while there is a good understanding on the chemistry of isocyanates and on their reaction mechanisms, little is known about their liquid-phase properties.

A number of theoretical studies employing density functional theory can be found, revolving around the interactions between the isocyanate ion and metallic systems. This is due to the presence of isocyanate as an intermediate compound during catalytic processes [63] involving carbon monoxide and nitrogen oxide. In this sense, studies comprise copper, both as small clusters [64, 65] and as periodic surface [66], palladium [67], silver [68], aluminium oxide [69], gold [70]. All these studies demonstrate strong chemisorption between the ion and the metallic substrate, which always occurs by a bond involving the nitrogen atom. In the case of gold, the formation of cyanuric acid, that is the cyclic trimer of isocyanic acid, occurring at the interface was also reported [71]. In a similar fashion, the adsorption of isocyanic acid has been studied in titanium dioxide and aluminium oxide [72, 73], due to its role in the selective catalytic reduction (SCR) process employed to treat diesel engines exhausts. Computational studies on isocyanic acid crystal structure were performed only recently [74], showing strong similarities with that of carbon dioxide.

Due to its presence in the interstellar medium and its alleged role in the chemistry of interstellar ices and comets [75], several works used ab-initio methods to study isocyanic acid properties in this context. The stable geometries of isocyanic acid-water clusters was explored by means of quantum calculations [76, 77]. Coupled-cluster calculations were employed to calculate the potential energy surface of the non-covalent interaction between isocyanic acid and molecular hydrogen, with the aim to calculate the inelastic scattering cross section and scattering rates between the two species [78]. Following to their recent discovery in interstellar medium, the crystal structure of methyl isocyanate was calculated using density functional theory to calculate its vibrational spectrum [61] in order to relate it with astrophysical observations. It is worth noting that in their work, Maté and collaborators guessed the methyl isocyanate crystal structure starting from the isocyanic acid one.

Most of the literature concerning aliphatic isocyanates and isocyanurates focuses on the study of cyclotrimerization reaction. Its mechanism has been firstly elucidated using Density Functional Theory methods by Okumoto and Yambe [9], which studied the ring formation with and without catalyst. They showed how the presence of a catalyst is fundamental in promoting the cyclotrimerization, while the dimer formation is unlikely to happen at any condition. A later study [79] pointed out that, without a catalyst, the ring formation could still occur, employing uretdione as an intermediate. Both works agree into suggesting that, when a catalyst is present, cyclotrimerization occurs through an activated catalyst-isocyanate complex, with uretdione still being reversibly formed. Similar conclusions were reached by further computational studies which investigated cyclotrimerization reaction kinetics with different catalysts [80, 81]. All of these studies are based on the determination of the geometry of the intermediate states and the

calculation of their energy. Energy differences between reactants, intermediates and products are then evaluated to assess the reaction probability.

Other reactions were investigated as well. The reaction between isocyanates and alcohols, at the basis of polyurethane synthesis, has been only recently studied using both experimental and theoretical calculations [82]. The adhesion properties of phenyl isocyanates species and the obtained urethanes on metal surfaces were studied for aluminium [83] and steel [84], but these studies did not consider aliphatic species. To our knowledge, non-covalent interactions of isocyanurates on any surface were never addressed. Likewise, a study on the possible interactions between aliphatic isocyanates and polyisocyanates is mostly missing. Concerning aromatic ones, a recent study [85] investigated the relative stability of diphenyl diisocyanate uretdiones, showing how the presence of noncovalent interactions, such as aromatic π stacking and van der Waals forces, helps in stabilizing the dimer. However, their conclusions are based solely upon energy calculations and do not investigate the nature of these bindings. Isocyanurate ring interactions have been recently investigated for the case of isocyanuric acid and it was shown that, due to hydrogen bonds, complex supramolecular structures could be formed, such as rosetta motifs [86] or molecular cages [87]. In both cases, the structures are held together by hydrogen bonds, and it is pointed out that the ring-based π interactions are responsible for holding small moieties within the cage.

The most surprising absence in aliphatic isocyanates literature is the one regarding atomistic molecular dynamics studies. This is probably the only computational tool capable to accurately predict macroscopic liquid properties and, most importantly, connect them with an understanding of the microscopic interactions. Still, as testified by the absence of dedicated force-fields parametrizations, there are no molecular dynamics studies addressing the isocyanates and polyisocyanates liquid properties, either aliphatic or aromatic. The reason of this lacking of information may be traced back to two factors: on one hand, isocyanate compounds are not involved in biological processes, making them to fall aside from the major classical force field parametrizations, historically developed for studying small organic molecules of biological interest [88, 89, 90, 91]. On the other hand, theoretical and computational research mainly addressed the final state of isocyanate-based products, obtained once that the isocyanate content has been already spent and is available as crosslinking points and/or urethane bonds.

In fact, systems such as polyurethanes have been the subject of many simulation works and generated a very large literature, the review of which falls out the scope of this thesis. Notwithstanding, it is important to draw the attention on these works that, apart from final material properties, also address the formation process itself, hence providing a modelling for the reactivity as well. Restricting the field to isocyanate-crosslinked systems, mesoscale coarse-grained simulations employing dissipative particle dynamics were

used to study the formation and morphology of isocyanate-crosslinked networks at their free surface [92, 93, 94], polycarbonate-polyurethane crosslinked materials [95], polyethylene glycol hydrogels [96, 97]. In all these works, the starting point is a mixture of some linear polymer and aliphatic isocyanate trimers. The reaction between isocyanates and the alcohols is simplified as a bond formation between the involved chemical species, triggered by their proximity. It has been shown that within this simple scheme, the reaction parameters do not influence the final structure and properties [98]. None of the above-mentioned works contemplates the cyclotrimerization as possible crosslinking mechanism.

Apart from dissipative dynamics studies, a MARTINI [99] coarse-grained parametrization was recently developed and used to investigate the polyurethane crosslinking process [100]. In their work, Ghermez-cheshme and collaborators derived MARTINI force field parameters starting from fully atomistic simulations performed using the OPLS-AA [101] force field, and noted that it performs poorly in predicting the isocy-anate properties. In their case, however, isocyanates constitute only a small fraction of the systems, and the parametrization error can be ignored. This last example best underlines how theoretical and modelling studies on isocyanates at the atomistic scale are utmost necessary, both to understand the isocyanate properties and to serve as solid foundations of larger scale approaches.

1.4   Objectives and thesis outline

In previous sections the exciting and multidisciplinary research on isocyanate has been explored. Whereas there is an abundance of experimental works highlighting the importance of isocyanate and their promising applications, it is clear that more work from the modelling and simulation side is required. The liquid state properties and interactions of aliphatic isocyanates and polyisocyanates liquids are poorly known. Adhesion properties were studied for few and very specific species, that is isocyanate ions and isocyanic acids. Effective all-atom forcefields for isocyanate-based molecules are lacking. The complex chemistry of isocyanates is far to be fully characterized.

The development of reliable models and effective simulation tools represent an unavoidable step to provide an answer to most of these questions. Firstly, they might be used as a predictive tool to guide and assist the design of novel compounds. Most importantly, simulations are often the only way to investigate the underlying physics influencing, driving and ruling the macroscopic behaviour of isocyanate systems, at time and length scales unattainable otherwise.

Therefore, the main objective of this thesis is to show how a wide range of electronic structure, atomis-tic and coarse-grained methods can be used to investigate the liquid state properties of isocyanate-based

materials, understand their interactions and characterize the network formation process. Generally spea-king, isocyanate-based liquids are complex molecular fluids, making their computational investigation a daunting task. Throughout the thesis it will be made clear how, to gain a deep understanding of the sy-stem, several time and space scales must be addressed using different methods in a multi-scale fashion, and how experimental data must be used as the cornerstone to assess the predictive power and validity to the proposed simulation models.

In chapter 2, an overview of the simulation techniques employed throughout this thesis is given, along with the theoretical concepts on which they are based upon. *Ab initio* calculations, molecular dynamics and dissipative particle dynamics simulations are explained, discussing the application field and limitations of each method.

The development of an optimized molecular dynamics force field for isocyanate-based molecules is presented in chapter 3. The new forcefield is tested and validated by comparing its predictions with experimental results, and used to investigate the liquid state of isocyanates and the relationship between their viscosity and molecular-scale features.

In chapter 4, isocyanates are investigated in detail with a range of *ab initio* methods, including density functional theory and symmetry-adapted perturbation theory, with the objective to clearly establish the nature of their intermolecular interactions and their influence over viscosity. Furthermore, the non-covalent functionalization capabilities of isocyanurate rings are evaluated by studying their adsorption on various 2D materials.

Networks and nanogels obtained from isocyanate end-functionalized polymers are studied in chapter 5. A dissipative particle dynamics simulation framework is employed, in conjunction with a modelling for the crosslinking reaction, to simulate the network formation process, to characterize their swelling and topological properties and to assess how those are affected by variations of processing conditions.

Chapter 2

Theoretical background and methods

This chapter provides an overview of the computational methods employed throughout this thesis. The focus is directed on describing the foundation of these methods and the justification for their choice, rather than implementation details, with references provided for the interested reader wishing to find complete and in-depth discussions of the touched topics. The chapter is divided in sections that follow a bottom-up approach starting with quantum mechanical calculation methods, followed by molecular dynamics simulations and ended by dissipative particle dynamics method.

2.1 Ab initio methods

2.1.1 The Schroedinger equation

Ab initio, meaning 'from the beginning', are all those methods that obtain the wavefunction of a many-electron system starting solely from the laws of quantum mechanics. Any polyatomic system is a collection of atoms held together by the interactions between their nuclei and electrons. It can be either a periodic arrangement of atoms or an isolated molecule. In the framework of quantum mechanics[1] , the physical state of the system is completely described by a wavefunction $|\Psi\rangle$. Wavefunctions are normalized in such a way that, in the position representation,

$$\langle\Psi|\Psi\rangle \equiv \int \mathrm{d}^3 r \Psi^*(\vec{r})\Psi(\vec{r}) = 1, \tag{2.1}$$

where the asterisk denotes the complex conjugation sign and the integral is extended over all volume.

Any observable O can be associated with an operator, whose expectation value on $|\Psi\rangle$ corresponds

---

[1]For a clear exposition of the foundations of quantum mechanics, we suggest the book of Sakurai [102].

to its measure:

$$\langle O \rangle = \langle \Psi | O | \Psi \rangle = \int \mathrm{d}^3 r \, \mathrm{d}^3 r' \Psi^*(\vec{r}) O(\vec{r}, \vec{r}') \Psi(\vec{r}'). \tag{2.2}$$

Obtaining the exact wavefunction means to have the complete physical knowledge of the polyatomic system, as it allows to calculate the expectation values of all observables. In stationary systems, whose status does not change over time, $|\Psi\rangle$ is the solution of the time independent Schroedinger equation

$$H | \Psi \rangle = E | \Psi \rangle, \tag{2.3}$$

in which H is the Hamiltonian operator of the system, which is unitary ($H^\dagger H = \mathbf{1}$), $|\Psi\rangle$ is an eigenstate of H, the eigenvalue being the total energy of the system. Of particular interest is the lowest-energy state, called ground-state. It can be shown that the Schroedinger equation obeys a variational principle, in the sense that the ground-state solution is the one that minimizes the total electronic energy, which is the expectation value of H over $|\Psi\rangle$. Any other possible solution of the Schroedinger equation represents an excited state, possessing a higher energy.

Let us consider n electrons and K atoms with masses M_I and atomic numbers Z_I. The Hamiltonian[2], neglecting any relativistic effect, is:

$$= \sum_{I=1}^{K} \frac{P_I^2}{2M_I} + \sum_{i=1}^{n} \frac{p_i^2}{2} + \sum_{i=1}^{n} V_N(r_i) + V_{NN} + V_{ee} \tag{2.4}$$

$$V_{NN} = \frac{1}{2} \sum_{I=1}^{K} \sum_{J \neq I}^{K} \frac{Z_I Z_J e^2}{|\vec{R}_I - \vec{R}_J|} \tag{2.5}$$

$$V_N(r) = \sum_{I=1}^{K} \frac{-Z_I e^2}{|\vec{R}_I - \vec{r}|} \tag{2.6}$$

$$V_{ee} = \frac{1}{2} \sum_{i=1}^{n} \sum_{j \neq i}^{n} \frac{e^2}{|\vec{r}_i - \vec{r}_j|}, \tag{2.7}$$

where V_{NN}, $V_N(r)$ and V_{ee} are the operators describing nucleus-nucleus, nucleus-electron and electron-electron interactions, respectively.

Analytic solutions of the Schroedinger equation with the Hamiltonian 2.4 are available only in the simplest situations (Hydrogen atom) meaning that, to solve more complex systems, approximations are required. Starting from almost one century ago, a series of methods have been developed with increasing accuracy, leading to the advanced techniques used nowadays.

---

[2]Throughout this chapter, atomic units are employed, so that $m_e = 1$, $e = 1$ and $\frac{1}{4\pi\varepsilon_0} = 1$. However, the symbol e is retained for clarity.

2.1.2   The Hartree-Fock approximation

The method of Hartree-Fock [103] (HF) is one of the earliest attempts to solve 2.4. Although it is nowadays almost never used by itself, it constitutes the starting point of more accurate methods, sometimes referred to as 'post-HF'. First of all, it is assumed that the electronic degrees of freedom are decoupled from those of ions (Born-Oppenheimer approximation [104]), so that the electronic part can be solved separately from the nuclear one, resulting in a factorized wavefunction: $|\Psi\rangle = |\Psi_N\rangle |\Psi_e\rangle$. Ions could be considered constrained to their equilibrium position with zero velocity, so that their kinetic energy term can be neglected and V_{NN} treated as a constant and added a posteriori. The electronic Hamiltonian then becomes:

$$H = \sum_{i=1}^{n} h(r_i) + \sum_{i=1}^{n} \sum_{j=i+1}^{n} \frac{e^2}{r_{ij}} \tag{2.8}$$

$$h(r) = \frac{p^2}{2} + V_N(r). \tag{2.9}$$

In 2.8, the 1-body part $h(r)$ has been separated from the 2-body electrostatic potential. Any eigenstate $|\Psi\rangle$ of 2.8 is a complex function of the positions and spins σ_i of all n electrons.

$$|\Psi\rangle = |\Psi\left(\vec{r}_1\sigma_1, \cdots, \vec{r}_n\sigma_n\right)\rangle_{GS} \tag{2.10}$$

A direct calculation of $|\Psi\rangle$ in this form is not feasible, as it depends in some complicated way on all the coordinates of all electrons. The main idea of HF theory is to approximate the many-electron wavefunction $|\Psi\rangle$ as a Slater [105] determinant of one-electron wavefunctions, called *spin-orbitals*, that is a product of a spatial $|\phi_i(\vec{r}_i)\rangle$ and a spin $|\chi_i\rangle$ part, $|\psi_i(\vec{x})\rangle \equiv |\phi_i(\vec{r}_i)\rangle |\chi_i\rangle$:

$$|\Psi\rangle \approx \mathrm{Det} \begin{bmatrix} \psi_1(\vec{x}_1) & \cdots & \psi_1(\vec{x}_n) \\ \vdots & \ddots & \vdots \\ \psi_n(\vec{x}_1) & \cdots & \psi_n(\vec{x}_n) \end{bmatrix} \tag{2.11}$$

The $|\phi_i(\vec{r}_i)\rangle$ are usually chosen to be orthonormal:

$$\langle \phi_i(\vec{r}_i)|\phi_j(\vec{r}_j)\rangle = \delta_{\sigma_i\sigma_j}\delta_{ij}. \tag{2.12}$$

The use of a Slater determinant takes into account the fact that electrons are fermions, because it is antisymmetric upon the coordinate exchange of two electrons. This means that the *exchange* correlation is correctly reproduced. However, any other correlation is completely ignored.

2.1.2.1   The Fock equations

Let us consider an eigenstate $|\Psi\rangle_0$ of 2.8 with energy E_0. Given a fixed spin configuration, we want to obtain the spin-orbitals that minimize E_0:

$$E_0 = \sum_i \langle \psi_i|h|\psi_i\rangle + \frac{1}{2}\sum_{i,j}\left[< \psi_i(i)\psi_j(j)|\frac{e^2}{r_{ij}}|\psi_i(i)\psi_j(j) > - < \psi_i(i)\psi_j(j)|\frac{e^2}{r_{ij}}|\psi_j(i)\psi_i(j) > \right],$$

(2.13)

where it is understood that $\psi(i) \equiv \psi(\vec{x}_i)$. It can be shown that E_0 is minimal when, for each of the spin-orbitals $|\psi_i\rangle$, the Fock equations are satisfied:

$$\left[\frac{p^2}{2} + V_N(r) + v_{Coul}(r) + v_{exch}(r)\right]|\psi_i\rangle = \epsilon_i |\psi_i\rangle,$$

(2.14)

where

$$v_{Coul} = \sum_j^{(occ.)} \langle \psi_i(\vec{r}\sigma)| \int \mathrm{d}(\vec{r'}\sigma')\psi_j(\vec{r'}\sigma')\frac{e^2}{|\vec{r}-\vec{r'}|}\psi_j(\vec{r'}\sigma')$$

(2.15)

$$v_{Exch} = \sum_j^{(occ.)} \langle \psi_j(\vec{r}\sigma)| \int \mathrm{d}(\vec{r'}\sigma')\psi_j(\vec{r'}\sigma')\frac{e^2}{|\vec{r}-\vec{r'}|}\psi_i(\vec{r'}\sigma')$$

(2.16)

are the Coulomb and exchange potential, respectively, and the sums run over all the occupied spin-orbitals. Equations 2.15 and 2.16 represent the 'classical' Coulomb interaction and an exchange operator. Equations 2.14 can be solved for each $|\psi_i\rangle$, and the full system's wavefunction $|\Psi\rangle$ can thus be reconstructed. Since the $|\psi_i\rangle$ appear in the definition of v_{Coul} and v_{Exch}, the solution has to be found in a self-consistent way. The commonly implemented technique in computational codes consists in an iterative procedure, where a first guess for the $|\psi_i\rangle$ is used to calculate the potentials to be employed for getting new $|\psi_i\rangle$ with which restart the iteration, until the total energy does not change anymore, up to some convergence threshold.

The HF method allows to change a many-body problem into a set of n intertwined 1-body equations, much simpler to treat. The Coulomb and exchange operators are mean-field terms: instead of the exact interaction V_{ee} (eqn. 2.7), the electron i interacts with the others through their spatially averaged charge density. The fermionic correlation, that is the repulsion between parallel spin electrons, is fully taken into account by the exchange term, which is often referred to as *exact* exchange. However, the HF method completely lacks all the dynamic correlation effects due to the electrons trying to minimize their Coulomb repulsion energy. Since correlations are at the basis of Van der Waals forces, those are absent in HF theory, thus representing an important limitation of this method. It is customary to define the *correlation energy* E_c as the difference between the solution from the non-relativistic Schroedinger equation and the Hartree-Fock energy:

$$E_c = E_{HF} - E_{exact}.$$

(2.17)

As the original Hamiltonian 2.8 is left unchanged, the variational principle still holds, meaning that the E_{HF} is always greater than E_{exact} and that E_c is always negative.

2.1.2.2   The Hartree-Fock-Roothan method and basis sets

The Fock equations are rather complex integro-differential equations, and even with the approximations made, a direct solution for them is difficult without any guess over the form of the $|\psi_i\rangle$. To circumvent this problem, the Hartree-Fock-Roothan [106] approach is used, in which every spin-orbital is expanded in a finite set of localized functions, referred to as a basis set. In doing so, HF equations could be solved with numerical methods. However, the solution accuracy will now depend on the finite basis set size. Series of basis sets with increasing number of functions may still be used to extrapolate to the complete basis set limit.

A wide variety of basis set exists. A natural choice is represented by Slater-type orbitals (STO), that is hydrogen atom like solutions. The notation STO-xG indicates that STO basis functions are used, each one further approximated by x gaussian functions, which allow for an efficient implementation in computational codes because they have analytical derivatives. A very popular basis set is the one by Pople [107], which employs gaussian type orbitals (GTO) to expand spin-orbitals. In the commonly used split-valence approach, core atomic orbitals are approximated with only one basis function. The notation 6-311G means that there is one basis function for core orbitals, composed by 6 gaussian functions, and 3 basis functions for valence orbitals, composed by 3, 1 and 1 Gaussian functions respectively. In many cases polarizable [108] and/or diffuse [109] functions may be added to the basis set, in order to correctly treat the polarization of orbital and regions with low electron density. The notation 6-311++G(d,p) indicates that polarization functions (d-type orbitals for p and p-type orbitals for s) and doubly diffuse functions (++) were added to the original basis set.

Other basis sets of interest are the correlation consistent ones, by Dunning and collaborators [110]. Those sets are indicated by the notation cc-PVxZ, which means correlation consistent basis set with polarizable functions, with valence-only orbitals represented by x basis functions. The augmented version with diffuse functions is commonly used: aug-cc-pVxZ. The peculiarity of Dunning's basis sets is that they are designed to converge smoothly to the complete basis set (CBS) limit as x is increasing, hence are very useful for CBS extrapolation techniques, which represent the 'gold standard' in QM calculations. The 'calendar' jun- and jul- cc basis sets are simplified versions of the aug-cc-pVxZ, with a smaller number of augmented functions.

The Hartree-Fock-Roothan method is used by all orbital-based QM codes. Within this work, all non

periodic density funcional theory calculations were performed with Pople's basis sets, while Dunning's ones were used for Moller-Plesset, coupled cluster and symmetry-adapted perturbation theory calculations.

2.1.3   Perturbative approaches

2.1.3.1   Moller-Plesset perturbation theory

The HF method lacks a treatment of electron correlations. A way to include them is by using Rayleigh's perturbation theory as firstly stated by Moller and Plesset [111] in 1934. The main idea of the MP approach is to consider the Fock Hamiltonian as that of the unperturbed system, and the difference between the HF electrostatic potential and the exact one as a perturbative term:

$$H = H^0 + H' \tag{2.18}$$

$$H^0 = H_{Fock} \tag{2.19}$$

$$H' = \sum_i \left[V_{ee} - \sum_{i=1}^{occ} (J_i - K_i) \right], \tag{2.20}$$

where, in the last row, J_i and K_i are the direct and exchange Coulomb operators, already defined by equations 2.15 and 2.16. The zero order energy E_0 is equal to the sum of all spin-orbital eigenvalues by construction. The first order energy E_1 correction is:

$$E_1 = \langle \psi | H' | \psi \rangle = \frac{1}{2} \sum_{i,j} \left[< \psi_i(i)\psi_j(j) | \frac{e^2}{r_{ij}} | \psi_i(i)\psi_j(j) > - < \psi_i(i)\psi_j(j) | \frac{e^2}{r_{ij}} | \psi_j(i)\psi_i(j) > \right],$$
$$\tag{2.21}$$

therefore $E_{MP1} = E_0 + E_1 = E_{HF}$ is equal to the Hartree-Fock energy. This means that the Hartree-Fock theory is correct up to the first order of MP perturbation theory(MPPT), a result also known as the Moller-Plesset theorem. The next term is the second-order energy term:

$$E_2 = \frac{1}{4} \sum_{i,j}^{occ.} \sum_{a,b}^{virt.} \frac{< \psi_i\psi_j | H' | \psi_a\psi_b > [< \psi_a\psi_b | H' | \psi_i\psi_j > - < \psi_a\psi_b | H' | \psi_j\psi_i >]}{\epsilon_i + \epsilon_j - \epsilon_a - \epsilon_b}, \tag{2.22}$$

where the ϵ_i are the eigenstates of the relative spin-orbitals, and the indexes a, b runs over unoccupied, also termed virtual, spin-orbitals. Due to the Brillouin theorem, singly excited states have null matrix elements, hence the only contributing matrix elements are the doubly excited ones. The MPPT truncated at the second order is called MP2. Further terms of the perturbative series could be included, however the MPPT series is not guaranteed to converge. Moreover, as the original Hamiltonian is changed, the variational principle is not valid anymore, meaning that the MP2 energy can be lower than E_{exact}.

Overall, the MP2 method is capable to capture most of the electron correlation effects, and may be seen as a reasonable choice for quantum mechanical calculations. In fact, truncating the perturbative series at 2-order is actually overestimating the correlation effects. In practice ,the calculation of E_2 involves

the explicit computation of 2-electron overlap functions, which makes this technique computationally expensive as the number of integral to be calculated scales as N^4, N being the number of electrons [112]. Within this work, molecules with 66 electrons represented the largest problem treatable with MP2, using a medium-sized basis set.

2.1.3.2   Symmetry-adapted perturbation theory

The system under investigation may be constituted by a complex of two non-covalently bound molecules A and B. To assess whether the bound state is energetically favoured, its interaction energy E_{int} is of interest:

$$E_{int} = E_{AB} - E_A - E_B, \qquad (2.23)$$

where E_{AB} is the electronic energy of the complex, while E_A and E_B are the energies of the isolated molecules. Let H_{AB} be the Hamiltonian of the full system and H_A, H_B the Hamiltonians of the separated molecules. The unperturbed Hamiltonian and the perturbation H' are then defined as:

$$H_0 = H_A + H_B \qquad (2.24)$$

$$H' = H_{AB} - H_0. \qquad (2.25)$$

H' contains all the intermolecular interaction terms. Concerning the wavefunction, the Slater determinant Ψ_{AB} obtained from the HF Hamiltonian H_{AB}^{HF} is not an eigenstate for H_0. If the unperturbed H_0 is to be kept, Ψ needs to be symmetry adapted, and the perturbative expansion modified accordingly. Symmetry-adapted perturbation theory (SAPT) [113] does exactly this, and may be seen as a double perturbation theory: the intermolecular interaction is expanded according to the London multipole expansion, while the intramolecular terms expanded as shown in MPPT. The higher order energies are:

$$E_{SAPT} = \sum^{ijk} E_{pol}^{ijk} + E_{exch}^{ijk}, \qquad (2.26)$$

where the index i denotes the intermolecular perturbation order and indexes j, k the intramolecular one. It can be shown that the 0th order SAPT energy is equal to the electrostatic interaction between the charge distributions of the two molecules. The first order energy, which unlike MPPT is nonzero, entails the effect of the variation of charge density of molecule A due to the charge distribution of charge B, that is induction charges. The second order energy represent the dispersion energy term, as it couples the density fluctuations of both molecules. Considering also the exchange terms, SAPT naturally provides an energy decomposition in which each term has a clear physical interpretation, making it a very useful method in providing quantitative information on the intermolecular interaction types.

15

According to the perturbative terms considered, different levels of SAPT are available. SAPT0 considers the polarization expansion up to the second order but does not consider intramolecular correlation effects. SAPT2 and SAPT2+ take into account those as well. It was shown [114] that, due to error cancellations, the relatively inexpensive SAPT0 used with the jun-cc-PVDZ basis set could provide qualitative results for large systems. For smaller systems, SAPT2+/aug-cc-PVDZ provides more accurate results, and was chosen as the standard SAPT method within this work, when possible.

2.1.4   Coupled cluster method

A wavefunction $|\Psi\rangle$, solution of a N-electron problem is approximated by a single Slater determinant (see equation 2.11) $|\Phi\rangle$, but can be expressed exactly as a linear combination of an infinite series of Slater determinants, including every possible excited state. In the coupled cluster (CC) method [115], this combination is expressed by means of an exponential formula:

$$|\Psi\rangle = e^{\mathbf{T}} |\Phi\rangle , \qquad (2.27)$$

where $\mathbf{T}$, the cluster operator, is defined as

$$\mathbf{T} = \sum_i \mathbf{T}_i \qquad (2.28)$$

and generates i-particle excitations from the ground state Slater determinant. In second quantization formalism, the T_i are characterized by coefficients t_i, which, if obtained, permit to calculate $|\Psi\rangle$. In coupled cluster singlet-doublet-perturbative triplet (CCSD(T)) method, only T_1 (singlet excitations) and T_2 (doublet excitations) are explicitly treated, while T_3 (triplet excitations) are included perturbatively. The CC methods are particularly expensive and can be applied only to small molecular systems.

The CCSD(T) method can be used in conjunction with MP2 and Dunning's basis sets, in a way that a complete basis set (CBS) extrapolation scheme can be defined, providing the CCSD(T)-CBS method [116]. This represents one of the highest accuracy methods available, representing one of the 'gold standards' in quantum chemistry computations. Due to its huge computational cost, it was here used to generate interaction energies of small molecular isocyanate dimers, up to 14 heavy atoms in total, to serve as a reference in testing the performances of lower accuracy methods.

2.1.5   Density functional theory

One of the greatest advances, if not a revolution, in the field quantum mechanical calculations is represented by density functional theory (DFT), originally devised by Hohenberg, Kohn and Sham. Not only DFT

provides a computational convenient and accurate way to solve electronic structure problems, but also indicates how it can be improved. The cornerstone of DFT was the demonstration that any observable, in particular the total energy, can be expressed as a functional of the density, which is the content of the Hohenberg-Kohn theorem.

2.1.5.1 The Hohenberg-Kohn theorem

Let us consider the N-electron Hamiltonian 2.8, whose non-degenerate ground state wavefunction is $|\Psi_{GS}\rangle$ and rewrite it separating the electron interaction and the nuclear external potential term:

$$H = H_{int} + V_{ext} \tag{2.29}$$

$$H_{int} = \sum_i \frac{p_i^2}{2} + \frac{1}{2} \sum_{i \neq j} \frac{e^2}{r_{ij}} \tag{2.30}$$

$$V_{ext} = V_{ext}(r) = -\sum_I \frac{Z_I e^2}{|\vec{R}_I - \vec{r}|}. \tag{2.31}$$

It is also useful to recall the definition of the ground-state density:

$$n(\vec{r}) = < \Psi_{GS}(\vec{r}_1, \cdots, \vec{r}_N)| \sum_i \delta^3(\vec{r} - \vec{r}_i)|\Psi_{GS}(\vec{r}_1, \cdots, \vec{r}_N) > \tag{2.32}$$

It can be noted that, for any fixed number N of electrons, all N-electron Hamiltonians are equivalent up an to the external potential $V_{ext}(r)$, which is the only variable of the system. The Hohenberg-Kohn [117] theorem states that there is an one-to-one correspondence between the ground state density of an N-electron Hamiltonian and the external potential acting on it.

Let's first prove that given any $V_{ext}(r)$ the corresponding density is unique. This is trivial, because $|\Psi_{GS}\rangle$ can be obtained by solving the Schroedinger equation, and it is non-degenerate by assumption. Therefore $n(\vec{r})$ can be obtained from 2.32.

To prove the other sense of the correspondence, let us suppose per absurd that there are two external potentials, $V_{ext}(r)$ and $\tilde{V}_{ext}(r)$ that correspond to the same density $n(\vec{r})$. Let H, $|\Psi_{GS}\rangle$, E_{GS} and $\tilde{H}$, $\left|\tilde{\Psi}_{GS}\right\rangle$, $\tilde{E}_{GS}$ be the Hamiltonians, ground state wavefunctions and energies associated with the different potentials. Because $|\tilde{\Psi}>$ is not an eigenstate for H, then

$$E_{GS} \leq < \tilde{\Psi}_{GS}|H|\tilde{\Psi}_{GS} >= \tag{2.33}$$

$$< \tilde{\Psi}_{GS}|H_{int} + \tilde{V}_{ext} + V_{ext} - \tilde{V}_{ext}|\tilde{\Psi}_{GS} >= \tag{2.34}$$

$$\tilde{E}_{GS} + \int \mathrm{d}^3 r n(\vec{r}) \left(V_{ext}(r) - \tilde{V}_{ext}(r) \right). \tag{2.35}$$

The same reasoning can be applied for $\tilde{E}_{GS}$, and eventually two inequalities are obtained:

$$E_{GS} - \tilde{E}_{GS} < \int \mathrm{d}^3 r n(\vec{r}) \left(V_{ext}(r) - \tilde{V}_{ext}(r) \right) \tag{2.36}$$

$$E_{GS} - \tilde{E}_{GS} > \int \mathrm{d}^3 r n(\vec{r}) \left(V_{ext}(r) - \tilde{V}_{ext}(r) \right) \tag{2.37}$$

For those to be simultaneously true, the right term must be zero, which is absurd because $V_{ext}(r) \neq \tilde{V}_{ext}(r)$ by hypothesis. So it must be $V_{ext}(r) = \tilde{V}_{ext}(r)$, proving the theorem.

To understand this result, it should be noted that the GS wavefunction is a functional of the external potential, $|\Psi_{GS}\rangle = |\Psi_{GS}\rangle [V_{ext}]$ and so are the GS expectation values of the kinetic energy $T = T[V_{ext}]$, the electron-electron interaction $V_{ee} = V_{ee}[V_{ext}]$ and the GS energy $E[V_{ext}]$. All these quantities, due to the HK theorem, may be recast unambiguously as functional of the GS density, and used to construct the Hohemberg-Kohn energy functional:

$$E^{(HK)}[n; V_{ext}] = < \Psi_{GS}[n]|T + V_{ee} + V_{ext}|\Psi_{GS}[n] >, \qquad (2.38)$$

or, equivalently,

$$E^{(HK)}[n; V_{ext}] = T[n] + V_{ee}[n] + \int d^3 r V_{ext}(r) n(\vec{r}), \qquad (2.39)$$

where V_{ext} is fixed and $|\Psi_{GS}\rangle [n]$ is the GS wavefunction with density n. It is evident that the HK energy functional will be minimal and equal to the exact energy of the N-electron system when n is equal to the exact ground state electron density. Most interestingly, the functional

$$F[n] = T[n] + V_{ee}[n] \qquad (2.40)$$

does not contain any dependence upon V_{ext}, hence it is universal, meaning that, if $F[n]$ is known, it would be possible to solve every electronic problem. Of course, $F[n]$ is not known, and most of the DFT research is devoted in finding the best approximations for it.

2.1.5.2 Kohn-Sham equations

The Kohn-Sham [118] assumption states that given a system of n-interacting electrons, it is always possible to find a system of n non-interacting electrons with the same ground state density. The assumption is correct for standard problems, thereby the GS wavefunction can be expressed, neglecting the spin degrees of freedom, as a linear combination of atomic orbitals (LCAO):

$$|\Psi\rangle_{GS} = \mathcal{A}\{\phi_1(\vec{r}_1) \cdots \phi_n(\vec{r}_n)\}, \qquad (2.41)$$

and the density becomes

$$n(r) = \sum_i^{(occ.)} \phi_i^*(\vec{r}) \phi_i(\vec{r}), \qquad (2.42)$$

where the orthogonality of atomic orbitals is assumed.

Although we do not know the exact functional form of $F[n]$, still we can elaborate the HK energy functional, taking advantage of the Kohn-Sham assumption. The non-interacting kinetic energy term and

Hartree potential may be defined as

$$T_0[n] = \sum_i < \phi_i(\vec{r}_i)|\frac{p^2}{2}|\phi_i(\vec{r}_i) > . \qquad (2.43)$$

$$V_H[n] = \frac{1}{2}\sum_{i\neq j} < \phi_i(\vec{r}_i)\phi_j(\vec{r}_j)|\frac{e^2}{r_{ij}}|\phi_i(\vec{r}_i)\phi_j(\vec{r}_j) >= \frac{1}{2}\int \mathrm{d}^3r\,\mathrm{d}^3r'n(\vec{r})n(\vec{r}')\frac{e^2}{|\vec{r}-\vec{r}'|}. \qquad (2.44)$$

Using these definitions in the HK functional we obtain

$$E^{(HK)} = T_0[n] + V_H[n] + \int \mathrm{d}^3rV_{ext}(r)n(\vec{r}) + E_{xc}[n] \qquad (2.45)$$

where the exchange-correlation functional $E_{xc}[n]$, defined as

$$E_{xc}[n] = T[n] + V_{ee}[n] - T_0[n] - V_H[n] \qquad (2.46)$$

contains now all the unknown quantities of our systems, expressed as the difference between the exact and non-interacting kinetic and potential energy terms. By carrying out a variational calculation, we obtain the final form of the KS equations:

$$\left[\frac{p^2}{2} + V_{ext}(r) + V_H(r) + V_{xc}(r)\right]|\phi_i\rangle = \epsilon_i\,|\phi_i\rangle . \qquad (2.47)$$

In principle, once that one has the exact form of V_{xc} at hand, these could be solved self-consistently and the GS wavefunction thus be obtained, just like as for the HF equations. However, while the HF equations are approximate, and so is the HF GS wavefunction, KS equations are exact, and so is their solution. Actually, the knowledge of V_{xc} would let to solve exactly all N-electron problems, due to the universality of the HK functional.

2.1.5.3   Local density and generalized gradient approximations, hybrid functionals

The ignorance of $F[n]$ directly translates into the impossibility to find an exact form of the exchange-correlation potential V_{xc} appearing in KS equations. However, several approximation can be made in order to provide a V_{xc} and obtain a solution of the KS equations. One of the first and successful attempts in this regard is represented by the local density approximation (LDA), in which the kinetic and exchange-correlation energy are assumed to match those for an homogeneous electron gas (HEG), a system of free electrons subject to an uniform positive potential to ensure neutrality. In LDA, the kinetic energy functional is expressed as:

$$T^{LDA}[n] = \frac{3}{10}(3\pi^2)^{2/3}\int \mathrm{d}^3rn^{5/3}(\vec{r}), \qquad (2.48)$$

while the exchange energy functional is provided by:

$$E_X^{LDA}[n] = -\left(\frac{3}{4}\right)\left(\frac{3}{\pi}\right)^{1/3}\int \mathrm{d}^3rn^{4/3}(\vec{r}). \qquad (2.49)$$

The correlation part can't be obtained analytically, but can be calculated with high accuracy, by using quantum Montecarlo methods, as done for instance by Ceperley and Alder [119]. All quantities appearing in LDA are local functions of the electron density and such assumption generally holds for system in which the electron density has a weak spatial dependency, such as in metals.

The model can be further improved by means of the generalized gradient approximation(GGA). In GGA, E_{XC} is a function of the density alone and of the density gradient ∇n, making the GGA a semi-local theory. In detail,

$$E_{XC}^{GGA}[n] = \int \mathrm{d}^3 r \epsilon_X^{HEG}(\vec{r}) F_{XC}(r_s, \zeta, s),$$
(2.50)

where the uniform exchange energy density ϵ^{HEG} from LDA is multiplied by an *enhancement factor* F_{XC} that depends on the atom size expressed by the Wigner-Seitz radius r_s), on the spin polarization ζ and on the reduced density gradient s,

$$s = \frac{\nabla n(\vec{r})}{2k_f n(\vec{r})},$$
(2.51)

where k_f is the Fermi momentum. The form of F_{XC} pertains to specific GGA formulations, such as those by Perdew and Wang [120], or the widely used by Perdew, Burke and Ernzerhof [121].

2.1.5.4   Hybrid functionals

Finally, DFT has found to be particularly effective when used in conjunction with hybrid functionals, in which the XC part is obtained by blending LDA, GGA and exact HF exchange functionals. Mixing these contributions helps to reciprocally compensate the error sources, hence providing better accuracy. Amidst the most used ones, there is B3LYP, obtained by using the B88 [122] exchange and the LYP [123] correlation functionals for the GGA part, and employing three parameters to mix them with exact and the VWN [124] formulation of LDA XC functionals:

$$E_{XC}^{B3LYP} = E_x^{LDA} + a_0(E_X^{HF} - E_X^{LDA}) + a_X(E_X^{GGA} - E_X^{LDA}) + E_C^{LDA} - a_C(E_C^{GGA} - E_C^{LDA}),$$
(2.52)

with $a_0 = 0.20$, $a_X = 0.72$ and $a_C = 0.81$. The mixing strategy allows for a compensation of error sources intrinsic to each method, hence providing a higher accuracy. While fast implementation exists in orbital-based codes, hybrid calculation are extremely expensive in plane-wave based codes, as explained in later sections.

2.1.5.5   Dispersion corrections

In DFT 2-electron correlations are not properly taken into account, such as in Moller-Plesset perturbation theory. This results in a significant underestimation of total energies for non-covalently bound dimers,

and in general for all those systems in which dispersion forces are expected to play a significant role. To correct this, it is possible to add to the Hamiltonian a set of interatomic potentials, in the form of Lennard-Jones parameters, that provide the missing dispersion empirically. This is the approach followed by the group of S. Grimme [125], that developed empirical dispersion terms for a wide set of functionals, including PBE and B3LYP. The inclusion of dispersion corrections provides a great increase of the accuracy of DFT calculations, and represents a fundamental ingredient that cannot be neglected. In this work, all DFT calculations were performed adopting the Grimme's D3 dispersion scheme, with Becke-Johnson damping [126]. In particular, for a system of N atoms, it is assumed that the DFT-D3 energy is the sum of a DFT electronic energy and a dispersion energy E_{Disp} made of 2-body and 3-body terms:

$$E_{DFT-D3} = E_{DFT} + E_{disp} \tag{2.53}$$

$$E_{disp} = E^{(2-body)} + E^{(3-body)} \tag{2.54}$$

$$E^{(2-body)} = \sum_{AB} \sum_{n=6,8,10...} s_n \frac{C_n^{AB}}{r_{AB}^n} f_{d,n}(r_{AB}) \tag{2.55}$$

$$E^{(3-body)} = \sum_{ABC} \frac{C_9^{ABC}(3\cos\theta_a \cos\theta_b \cos\theta_c + 1)}{(r_{AB}r_{BC}r_{CA})^3}, \tag{2.56}$$

where in the many-body terms the sums run over all possible pairs AB and all possible triplets ABC. In $E^{(2-body)}$, the s_n are scaling factors which values are defined in the $[0,1]$ interval, and the $f_{d,n}$ are additional damping functions. The C_n are the actual dispersion parameters, which are obtained from ab initio calculations. In the 3-body term, the C_9^{ABC} are approximated by a geometric mean:

$$C_9^{ABC} \approx -\sqrt{C_6^{AB} C_6^{BC} C_6^{CA}}. \tag{2.57}$$

2.1.5.6 Basis set superposition error

When calculating the interaction energy of a dimer using non-orthogonal localized basis sets, there is a computational artefact called basis set superposition error (BSSE), which is caused by the fact that, when the two molecules are close, the electron of molecule A can 'see' the basis set functions of molecule B, and may spread into some of those in the energy minimization process. This will cause interaction energies to be slightly overestimated. To correct this, a counterpoise (Cp) calculation needs to be performed, in which each of the monomer energy calculation is performed in the so-called extended basis set, that contains also all the orbitals from the other monomer's atoms (called in this case ghost atoms), but with no electrons. Comparing with the monomer-only basis set energy, the correction is obtained. All dimer calculations presented in this work made use of the BSSE correction, which needs to be taken into account also for MPPT and CCSD.

2.1.5.7   Non Covalent Interaction analysis

Non covalent interaction index (NCI) [127, 128] analysis is a technique which allows to identify the regions of a molecule subject to weak noncovalent interactions from the electron density, and to classify them. In particular, it relies on the reduced density gradient s, defined in equation 2.51, and identifies the non-covalent interaction by the presence in $s(n)$ of regions in which both the density n and its second eigenvalue λ_2 are small. $s(n)$ isosurfaces can be plotted and coloured according to $\mathrm{sgn}(\lambda_2)\rho$, allowing the visualization of non-covalent interaction sites. Although NCI is a less quantitative method compared to an SAPT analysis, it provides valuable insight on the contact regions between molecules. The NCI analyses were performed using the multiWFN package [129].

2.2   Periodic systems

A crystal is a collection of atoms arranged in a regular structure, called a lattice. The presence of translational invariance in crystals has very important consequences in terms of their electronic structure, with the appearance of delocalized electrons, which cannot be assigned to any particular nucleus. Because of this, periodic systems are in general difficult to treat with an orbital-based approach, and a plane wave decomposition represents a more natural choice, as it entails naturally the concept of periodicity.

2.2.1   Periodic systems and primitive cell

Let us consider distribution of points in space. If there exists a set of them from which all the others can be obtained by means of translations, those have spatial periodicity and form a *Bravais lattice*. If the points represent atoms, the Bravais lattice describes a crystal. Any translation vector $\vec{t}$ is defined as

$$\vec{t} = n_1\vec{t_1} + n_2\vec{t_2} + n_3\vec{t_3};\ n_1, n_2, n_3 \in Z, \tag{2.58}$$

where the linearly independent $\vec{t_i}$ are termed basis vectors, and identify the *primitive cell*, whose volume is

$$\Omega = \vec{t_1} \cdot \left(\vec{t_2} \wedge \vec{t_3}\right) \tag{2.59}$$

The equilibrium position of the atoms within the primitive cell are defined by the vectors $\vec{d_i}$, expressed in the basis of the $\{\vec{t_i}\}$. In the most basic structure, a monoatomic simple cubic lattice, there is only one atom at the origin of the primitive cell, whose basis vectors are orthogonal and have the same length a.

The *reciprocal space* is the space spanned by the reciprocal vectors $\vec{g_i}$, defined such that

$$\vec{g_i} \cdot \vec{t_j} = 2\pi\delta_{ij} \tag{2.60}$$

An useful construct is the Wigner-Seitz cell (see figure 1), defined as the set of points that are closer to a lattice point than all the others. The equivalent construct in the reciprocal space is called Brillouin zone (BZ). Within the BZ there are some important high-symmetry points, in which interesting phenomena occur. The origin of reciprocal space is the Γ-point, which corresponds to constant terms in the Fourier plane wave expansion of fields (like the potential or wave functions), i.e. non-periodic contributions. Other high-symmetry points may be found at the vertexes and mid-points of the BZ edges; their number and position depend on the shape of the BZ and, more in general, on the crystal symmetry group.
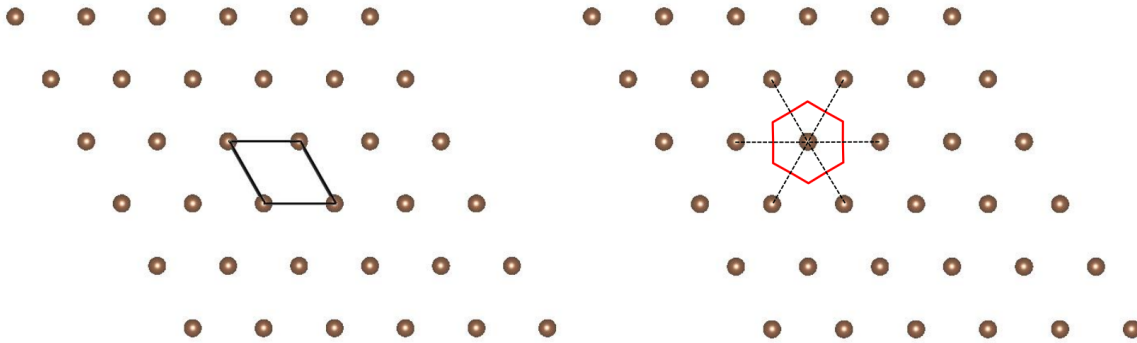
Figure 1: On the left, representation of a bidimensional crystal with an hexagonal unit cell (in black). On the right, the corresponding Wigner-Seitz cell (in red).

2.2.2   Wavefunction in crystals and the Bloch theorem

Consider an electron within a crystal with lattice constants $\vec{a}$. It is described by the Hamiltonian

$$H = \frac{p^2}{2} + V(r), \tag{2.61}$$

where $V(r)$ is the electrostatic potential generated by the nuclei and clearly has the same periodicity of the crystal: $V(r + t_n) = V(r)$, where $t_n = \vec{n} \cdot \vec{a}$, $\vec{n}$ being a vector of integers. Because of this, $V(r)$ accepts a Fourier plane wave expansion:

$$V(r) = \sum_{m=-\infty}^{+\infty} V_m e^{i\frac{2\pi\vec{m}}{a}\vec{r}}. \tag{2.62}$$

The Bloch [130] theorem states that the wavefunction of an electron $|\psi\rangle$ subject to a periodic potential may be written as the product of a plane wave and a delocalized function with the same periodicity of the crystal:

$$|\psi\rangle_{\vec{k}}(\vec{r}) = e^{i\vec{k}\vec{r}}u(\vec{k},\vec{r}) \tag{2.63}$$

$$u(\vec{k},\vec{r}) = \sum_{n=-\infty}^{+\infty} a_n(\vec{k})e^{i\frac{2\pi\vec{m}}{a}\vec{r}} \tag{2.64}$$

In view of an non-interacting approximation, the Bloch theorem suggests that a plane wave decomposition, rather than one based upon localized spin-orbitals, is a much more natural choice for periodic systems.

It is easily proved that $V(r)$ only mixes plane waves which wavevectors $\vec{k}$ differ by any reciprocal vector:

$$e^{i\vec{k}'\vec{r}}V(r)e^{i\vec{k}\vec{r}} = V_m\delta^3\left(\vec{k}' - \vec{k} - \frac{2\pi\vec{m}}{a}\right).$$ (2.65)

Hence, all independent values of k lie in the first BZ. Fixing a value for k and solving the Schroedinger equation will provide an infinite set of solutions $\{\phi_n\}$, in the form of 2.64, with energies $E(k)_n$ sorted according to some quantum number n. Repeating this procedure for all the possible values of k in the first BZ would result in the emergence of allowed and prohibited regions of energy, called bands, which may be seen as a generalization of the isolated systems energy levels. Finally, in the limit of an infinite system, the minimum spacing in the reciprocal space tends to 0, k becomes a continuous variable, and $E \rightarrow E(k)$. When calculations are performed on periodic systems, observables are expected to be functions of k. Since the number of allowed wavevectors in the BZ is large (and asymptotically infinite), a restricted set of k-points is chosen and the Schroedinger equation (independently) solved for each one of them. Observables are then calculated as averages over the selected N_k k-points:

$$\langle O\rangle = \frac{1}{N_k}\sum_{i=1}^{N_k} O(k_i)$$ (2.66)

Any periodic DFT calculation needs to be checked for convergence with respect to the number of k-points. In this thesis, a total energy convergence threshold of 1 meV was considered as the acceptance criterion for a k-point grid. When dealing with a supercell, that is a system that is the product of primitive cells, the Brillouin zone is greatly reduced and a smaller number of k-points might be used, because the accuracy actually depends on the k-point density.

2.2.3   DFT methods for periodic systems

In a crystal, as done for isolated systems, an independent-electron approximation may be introduced and a set of Kohn-Sham equations derived and solved to obtain the ground-state density. In general, the electronic orbitals may be separated into strongly bound and well-localized ones, representing the core electrons and a weakly bound and diffuse ones, corresponding to valence electrons. In view of this, the space can be separated into core regions, modelled as spheres or Wigner-Seitz cells around the atoms, and a valence region that encompasses the remainder.

The Bloch theorem ensures that all wavefunctions have the same periodicity of the lattice, hence a plane wave expansion is a very natural choice, and indeed very appealing, because plane waves are simple

to treat from a computational point of view. However, as shown by Herring [131], the strong localization of core orbitals would require a very large number of plane waves for an accurate representation, hindering any expansion in this sense.

To solve this issue, a range of methods has been developed to take advantage of the core-valence separation, replacing the core region strong potentials with effective *pseudopotentials*, in which the strong and localized contributions are smoothed.

2.2.3.1   Orthogonalized plane wave method

Although it is not a commonly used method in modern DFT codes, the orthogonalized plane wave method represents a simple way to understand the origin of pseudopotentials. Consider an Hamiltonian H of the form

$$H = \frac{p^2}{2} + V(r),$$ (2.67)

with a set of orthonormal solutions $\{\phi_i\}$, the first q of which are known. It is generally possible to separate the loosely bound and extended valence eigenstate $|\phi^v>$ from the tightly bound and well-localized core eigenstates $|\phi_i^c\rangle$. Suppose then that the first q known eigenstates correspond to the core states, and solutions for the valence eigenstates are to be determined.

At the basis of the OPW method [131] there is the possibility to restate the valence eigenfunctions as a sum of a smooth wavefunction and a strongly localized part, orthogonal to the former by construction:

$$|\phi^v> = |\tilde{\phi}^v> - \sum_i <\tilde{\phi}^v|\phi_i^c> |\phi_i^c>,$$ (2.68)

where the part under the sum sign is a projection over the core eigenstates. By replacing 2.68 into the Schroedinger equation for a valence eigenstate with the Hamiltonian given in 2.67, it is possible to obtain an eigenvalue equation for the smooth wavefunctions [132, 133]:

$$\tilde{H}\left|\tilde{\phi}_i^v\right\rangle = \left(\frac{p^2}{2} + V^{PKA}(r)\right)\left|\tilde{\phi}_i^v\right\rangle = \varepsilon_i^v\left|\tilde{\phi}_i^v\right\rangle$$ (2.69)

where

$$V^{PKA} = V + V^{Rep}$$ (2.70)

$$V^{Rep}\left|\tilde{\phi}_i^v\right\rangle = \sum_j \left(\varepsilon_i^v - \varepsilon_j^c\right)\left\langle\phi_j^c|\tilde{\phi}_i^v\right\rangle |\phi_j^c\rangle .$$ (2.71)

V^{Rep} is a repulsive potential, as $\left(\varepsilon_i^v - \varepsilon_j^c\right)$ is always positive and it is non-local. It may be regarded as effect of the core electrons, effectively screening the nuclear charge. By consequence, the total potential $V(r) + V^{Rep}(r)$ felt by a valence electron is weaker than $V(r)$ alone.

2.2.3.2 Pseudopotentials

The whole potential 2.70 may be replaced by a smooth function that reproduces its same scattering properties with respect to the valence states. The space can be separated into a 'core' region, within some radius r_C and an 'outer' region. Within r_C, the pseudopotential may be assumed to be spherically symmetric and diagonal with respect to the angular momentum. In this case, partial waves provide an orthonormal set, and different l contributions are treated independently. In the outer region, the potential is simply Q_{ion}/r, Q_{ion} being the ion charge. Being this contribution weak, the wavefunction of valence states is naturally smooth here, and can be easily expanded in plane waves.
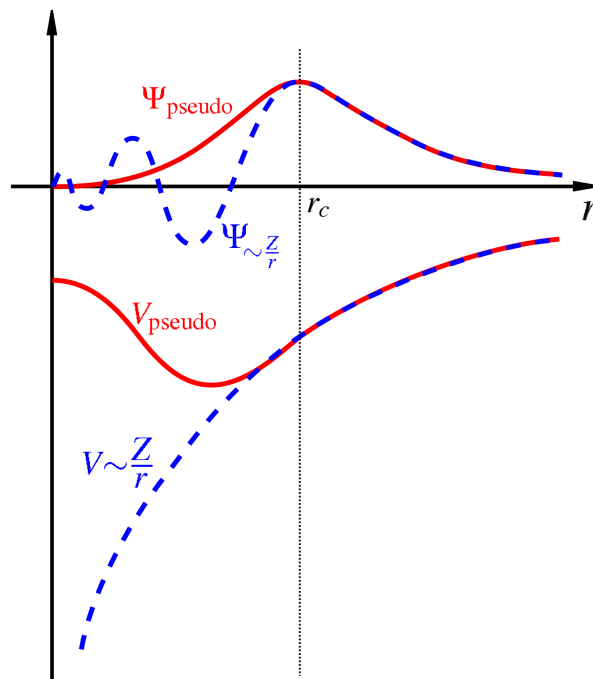
Figure 2:   Schematic representation of pseudopotentials and pseudowavefunctions(in red), compared with the normal ones (in blue). Image from [134].

To be well-behaved, some conditions are requested to the pseudofunctions. Outside r_c, the normal and pseudowavefunctions must match. At r_c, continuity and first derivate continuity of pseudowavefuncti-ons must hold, as well as for their first energy derivatives. Finally, the charge enclosed within the cut-off radius of standard and pseudowavefunctions should be the same. Imposition of the last condition provides the so-called norm conserving pseudopotentials [135, 136]. Alternatively, it can be relaxed in order to obtain PPs as smooth as possible, that is *ultrasoft* pseudopotentials [137] . The starting point of these methods is a solution of the KS equations for an isolated atom, under the *frozen core* approximation, which states that the core states are not affected by the presence of other surrounding atoms (as in a crystal).

2.2.3.3   Projector augmented wave method

The projector augmented wave (PAW) method, developed by Blochl in 1994 [138], may be regarded as a generalization of the previous methods, with the great advantage to provide a clear connection between the expectation values calculated on the original and pseudo wavefunctions. The real space is separated between non-overlapping spherical regions Ω_R around atoms, called augmentation spheres, and the remainder. outside Ω_R, the real and pseudo wavefunctions are coincident. Within the Ω_R, the real wavefunctions are solutions of the Schroedinger equations for the all-electron (AE) isolated atom, while the PS are a smooth continuation of the outer ones. Both sets form a complete set for the valence states within Ω_R. This implies that a linear transformation exists, defined as

$$\phi_i = \mathcal{T}\tilde{\phi}_i \tag{2.72}$$

where the $\{\phi_i\}$, $\{\tilde{\phi}_i\}$ are a basis of the real and PS valence functions respectively, e.g. a set of partial waves:

$$\tilde{\Psi} = \sum_i c_i \tilde{\phi}_i. \tag{2.73}$$

Applying the linear transformation on 2.73 it is possible to show that the same coefficient c_i are present in the expansion for Ψ:

$$\Psi = T\tilde{\Psi} = T\sum_i c_i \tilde{\phi}_i = \sum_i c_i \phi_i \tag{2.74}$$

The AE wavefunction can be then expressed as:

$$\Psi = \tilde{\Psi} + \sum_i c_i \left(\tilde{\phi}_i - \phi_i \right), \tag{2.75}$$

which has the form $\mathcal{T} = 1 + \mathcal{T}_R$, where $\mathcal{T}_R$ is nonzero only within Ω_R. The coefficients c_i are still unknown, but can be expressed as the result of a projection of $\tilde{\Psi}$ over a set of *projector functions* $\tilde{p}_i$,

$$c_i = <\tilde{p}_i|\tilde{\Psi}>, \tag{2.76}$$

which must obey the following completeness and orthogonality rules:

$$\sum_i |\tilde{p}_i><\tilde{\phi}_i| = 1, \tag{2.77}$$

$$<\tilde{p}_i|\tilde{\phi}_j> = \delta_{ij}. \tag{2.78}$$

With the use of projector function, the transformation operator may be expressed as:

$$\mathcal{T} = 1 + \sum_i \left(\tilde{\phi}_i - \phi_i \right) <\tilde{p}_i|. \tag{2.79}$$

The transformation T connects the AE wavefunction to the PS ones, and it is defined in the whole space. As a consequence, any operator A defined on the space of the AE wavefunctions can be linearly transformed into one that operates into the PS space, and its expectation value calculated using the PS wavefunctions:

$$\tilde{A} = \mathcal{T}^{\dagger} A \mathcal{T} \tag{2.80}$$

$$= A + \sum_{i,j} |\tilde{p}_i> \left(<\phi_i|A|\phi_j> - <\tilde{\phi}_i|A|\tilde{\phi}_j> \right). \tag{2.81}$$

Expressions for the total energy and other quantities, as well as details on the protocol and implementation of the PAW method can be found in [138]. In this theory, pseudopotentials still play a prominent role, as they are required to build the PS wavefunctions in the augmentation sphere.

The PAW method was employed for all periodic calculations performed in this thesis. Like any other plane-wave expansion based method, there is an intrinsic error due to the finiteness of the plane waves, truncated to an energy cutoff of several hundreds of eV. This means the calculation results must be checked for convergence with respect to the plane-wave cutoff. The same 1 meV tolerance for the total energy as for the k-point sampling convergence was used. While values around 600 eV are adequate for bulk systems, when vacuum is present as in calculations regarding two-dimensional materials the cutoff needs to be increased, and a value of 1000 eV is required to achieve good convergence.

2.3 Ab initio calculations in practice

Here we illustrate the typical steps involved in *ab initio* calculations. For non periodic systems, the package Gaussian 09 [139] was used to perform all calculations, except for SAPT ones, in which case the Psi4 code [140] was employed. For periodic systems calculations, the VASP code [141, 142], which implements the PAW method, was used.

2.3.1 Geometrical optimizations

A polyatomic system is provided as a list of atoms and positions, either built from scratch or downloaded from some reference database, such as COD [143]. The initial step consists into the choice of the method and its testing. In the case of orbital-based code, the basis set is expanded as much as possible, provided the most complex molecule/dimer to describe can be treated within the chosen method. Likewise, for plane-wave codes, convergence of the total energy over the number of k-points and plane wave energy cutoff are conducted.

The starting structure is generally unrelaxed, therefore the atoms' positions need to be adjusted to minimize internal forces. Different methods and/or basis sets (or energy cutoffs) will change interatomic forces, resulting in different relaxed structures. Each ionic step requires a full electronic calculation, causing the relaxation to be the most demanding part of a quantum mechanical calculation. When advanced methods are desired, this step may be omitted and the electronic calculation carried on with a structure relaxed with a lower accuracy method. The relaxation is generally stopped when all atomic forces fall below a certain threshold, typically $1 - 2 \times 10^{-2}$ eV/Ang. After this , the relaxed structure is available for further calculations, and important quantities such as the charge density are always obtained from minimized structures.

From a general point of view, the optimization moves the system through its potential energy (hyper) surface, until a stationary point is found. It should be noted that, without further analysis, there is no guarantee that the final conformation is truly an energy minimum, and a normal mode analysis should be performed to clarify this, as discussed in next section.

In view of classical force field parametrization, potential energy scans of selected degrees of freedom, such as dihedral angles, are of particular interest. The coordinate of interest is varied by small steps and frozen, while the rest of the molecule is allowed to relax, and a geometrical optimization for every variable value is performed. As a result, an energy profile is obtained that can be fitted with the desired functions, as will be discussed in section 2.4.2.

2.3.2   Normal modes and vibrational frequencies

In any molecular system, the knowledge of the Hessian matrix, defined as

$$H_{ij} = \frac{\partial U}{\partial x_i \partial x_j},$$
(2.82)

U being the total potential energy of the system, allows to classify the minimum energy points obtained through a geometrical optimization and to calculate its normal modes and vibrational frequencies, which are of interest because can be directly measured by several techniques.

To obtain H_{ij}, the most robust approach is to numerically calculate it by a central difference method, where each atom of the system is displaced in all possible directions, with positive and negative displacements, and the resulting forces are used to build the Hessian. When diagonalized, the eigenvectors represents the normal modes of the systems, and eigenvalues their frequencies. In correspondence of every stationary point all forces are null, and the nature of the critical point is established by the normal mode frequencies. If it is a true minimum, any atom displacement produces a recalling forces, and all

frequencies are real. Conversely, if the critical point is a saddle point, there will be modes with imaginary frequencies, corresponding to relaxation modes.

2.3.3   Density of states and band structure calculations

In periodic systems, a very important quantity is the total density of states (DOS), defined as the number of electronic states that can be found in a certain interval of electronic energy:

$$DOS \equiv \frac{\mathrm{d}n(E)}{\mathrm{d}E} \tag{2.83}$$

the DOS is calculated on relaxed structures by using the highest possible numbers of k-points, in order to have the best accuracy.

To calculate energy bands, closed paths joining the high-symmetry points in the k-space are generally employed. However, this k-point selection is not a good choice to represent of the whole k-space. For this reason, the charge density from a previous calculation with a good k-space sampling scheme, e.g. the one resulting from a DOS calculation, is used instead.

2.4   Molecular Dynamics simulations

Ab-initio quantum methods certainly are an extremely powerful tool to study the fundamental properties of condensed matter systems. However, there are some intrinsic limitations restricting their application fields, mostly due to their computational demands. With the resources typically available to the author, systems with no more than 100 heavy atoms could be treated using DFT or perturbative approaches.

To treat larger systems, one can turn to Molecular Dynamics (MD), which is a model where the constituents and their interactions are entirely described by classical physics. Despite the approximation made within MD could look raw, nevertheless MD allows for simulations of millions of atoms, leading to the prediction of thermodynamic quantities. One of the advantages of MD simulations is that the interaction potentials and parameters can be chosen in a way to closely reproduce the quantum-mechanical forces of the system under interest allowing, with the appropriate parametrization, to simulate a very large class of systems, from molten metals to proteins. In the following, the basic ideas behind MD methods will be presented, followed by the introduction of force fields for molecular modelling.

2.4.1   Basic ideas of Molecular Dynamics

2.4.1.1   MD equations of motion and LJ potential

Let us consider a system of N point-like massive and neutral particles, called atoms or -more generally-beads, interacting through a certain conservative pair potential U, which depends solely on the interatomic distance. The total Hamiltonian of the system is

$$H = \sum_i \frac{p_i^2}{2m_i} + \frac{1}{2} \sum_{i \neq j} U(r_{ij}),$$ (2.84)

Each bead i is subject to the interaction with all the others, resulting in the total potential

$$V_i = \sum_{j \neq i} U(r_j - r_i)$$ (2.85)

and the force $\vec{f}_i = -\nabla V_i$. The equation of motion for bead i is simply

$$m_i \ddot{\vec{r}}_i = \vec{f}_i.$$ (2.86)

MD consists in solving the Newton's equations of motion 2.86 for all beads, in order to provide the dynamic evolution of the system.

The interaction potential $U(r_{ij})$ is a crucial element of the model. A common choice for interatomic interactions is the Lennard-Jones (LJ) potential(see figure 3):

$$U_{LJ}(r) = 4\varepsilon \left[\left(\frac{\sigma}{r} \right)^{12} - \left(\frac{\sigma}{r} \right)^6 \right],$$ (2.87)

The LJ potential has a long-range attractive tail and a short-range repulsion. The attractive part has the r^{-6} power law, typical of London dispersion forces, while the repulsive core prevents the atoms to overlap. In 2.87, σ is the zero-crossing point of the LJ potential and ε, which is located at $r_0 = 2^{1/6}\sigma$. For $r \rightarrow \infty$, $U_{LJ}(r) \rightarrow 0$.

Depending on the system of interest, other suitable choices for $U(r)$ can be made. However the LJ potential, due to its relative simplicity and its physical connection with dispersion forces, represent the standard choice for all-atom simulations of molecular liquids.

In many cases, such as in all-atom simulations, a certain electrostatic charge q_i is assigned to each atom. In this case, an electrostatic interaction term is added to the Hamiltonian 2.84:

$$V_{Coul} = \frac{1}{2} \sum_{i \neq j} \frac{q_i q_j}{r_{ij}},$$ (2.88)

Since in MD periodic boundary conditions are used to mimic the behaviour of infinite systems, charge neutrality must always be checked to avoid unwanted effects.
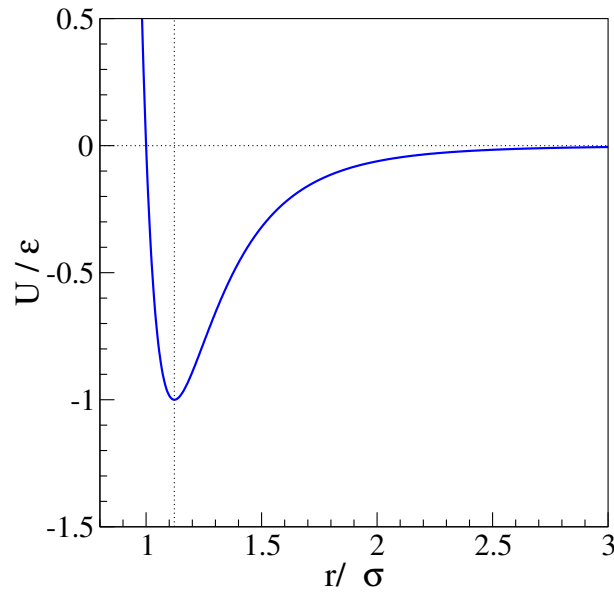
Figure 3: Lennard-Jones potential with $\epsilon = 1$ and $\sigma = 1$. The vertical dashed line denotes the position of the minimum.

In a system of N beads, the number of pairs scales as N^2. However, the long-range behaviour of the LJ potential makes it possible to consider a cut-off distance for pair inclusion which greatly reduces the number of pairs. This is justified by the fact that, at the typical cut-off distance of 3σ, we have $U_{lj}(3\sigma) \approx 5.2e^{-3}\varepsilon$, and also that, at least for disordered dense systems, the resultant of all beads outside the cut-off radius will provide a null contribution due to long-range isotropy. As a matter of fact, the truncation does introduce some errors that require either small corrections or a long-range treatment. To avoid this, it is possible to multiply the LJ potential with a smoothing function that makes it null at the cutoff distance, as done e.g. in the CHARMM force field [91]. However, when electrostatic interactions are also accounted for, this scheme is not sufficient, because of their slower r^{-1} dependence. In the Particle Mesh Ewald (PME) method [144], a cutoff range is defined and interactions within are calculated directly, while those outside are calculated in the reciprocal space, through a Fourier Transform. In molecular simulation codes, it is often used a slight variant called PPPM [145], which may be applied as well to the long-range part of LJ potential [146].

If the simulated system represent a molecule, then atoms are linked together by bonds, which are represented by extra potential terms acting only on bonded atom pairs. 3-body angle and 4-body dihedral and improper potential terms can be present as well, to better describe the intramolecular forces and

obtain good molecular geometries, when compared to quantum mechanical calculations. More details are discussed further in text, in section 2.4.2.

2.4.1.2   Integration of the equations of motion

To obtain the dynamic evolution of the simulated systems one needs to integrate numerically the equations of motion. As the consequence of the finite precision of any computing machine, what is actually computed is a discretized approximation of the continuous trajectories, with a finite integration step Δt. Consider a point-like body of mass m, subject to the force $f(t)$, of which we know the position $r(t)$ at time t. Being Δt the timestep A second-order Taylor expansion can always be written for $r(t + \Delta t)$:

$$r(t + \Delta t) = r(t) + v(t)\Delta t + \frac{f}{2m}(\Delta t)^2 + o(\Delta t^3). \tag{2.89}$$

Analogously,

$$r(t - \Delta t) = r(t) - v(t)\Delta t + \frac{f}{2m}(\Delta t)^2 + o(\Delta t^3). \tag{2.90}$$

By summing up these equation, an estimate for $r(t + \Delta t)$ is obtained:

$$r(t + \Delta t) = 2r(t) - r(t - \Delta t) + \frac{f}{m}\Delta t^2 + o(\Delta t^4) \tag{2.91}$$

and the velocities can be recalculated by

$$v(t) \approx \frac{r(t + \Delta t) - r(t - \Delta t)}{2\Delta t}. \tag{2.92}$$

This is the standard Verlet algorithm, that requires the knowledge of position both at time t and $t - \Delta t$. The velocity Verlet algorithm is slightly more efficient, as it predicts $r(t + \Delta t)$ knowing the position and velocity at time t. To show this, consider the Taylor expansion of the velocity:

$$v(t + \frac{\Delta t}{2}) = v(t) + \frac{f(t)}{2m}\Delta t + o(\Delta t^2). \tag{2.93}$$

Substituting in 2.89 gives

$$r(t + \Delta t) = r(t) + v(t + \frac{\Delta t}{2})\Delta t + o(\Delta t^2). \tag{2.94}$$

Once the new position is known, the new velocities can be calculated with

$$v(t + \Delta t) = v(t + \frac{\Delta t}{2}) + \frac{f(t + \Delta t)}{2m}\Delta t + o(\Delta t^2). \tag{2.95}$$

From the above formulae, it emerges that each step will inevitably produce small errors proportional to Δt that will accumulate as the simulation runs, eventually invalidating it. Moreover, this will cause two trajectories starting from the same initial conditions not to match exactly, because the errors act as a

random source of noise. Whereas smaller Δt reduces the integration error, very small values would result in impractically long simulations. As a rule of thumb, Δt needs to be chosen in a way that the fastest degrees of freedom of the system are sufficiently sampled and the overall accuracy is reasonable.

A way to quantify this, is to run a constant-energy simulation and monitor the energy drift, which should not change in ideal conditions. If the drift is larger than a certain threshold, then the timestep must be reduced. In MD simulations contained in this thesis, the value $\Delta E_{threshold}/E(t=0) = 1e^{-4}$ per million steps was used.

2.4.1.3   The rRESPA algorithm

In many cases, the interaction potentials in MD can be range-separated into a short-range and a long-range term. When this occurs, short-range terms have steeper gradients generating a fast dynamics, while long-range terms have small gradients and slow dynamics. This means that the appropriate timestep for the short-range part of the potential may be unnecessarily fine for the long-range part. The idea of the rRESPA [147] algorithm is to use a timestep Δt for the long-range part, while considering an inner timestep $\Delta t/n_r$, with n_r being a positive integer, for the short-range part. This provides a significant speed-up when compared to the same simulation with an unique timestep $\Delta t = \Delta t/n_r$. rRESPA levels may be nested and 3-4 levels can be used for complex molecule simulations.

2.4.1.4   Ensemble averages in MD

Consider, in three dimensions, a system of N particles, described by a classical Hamiltonian of the type 2.84, which is a function of the 3N coordinates and 3N conjugated momenta. Each state of the system can be described by a point in the 6N-dimensional phase space. During its dynamical evolution, the system particles will change their coordinates and momenta, moving along a trajectory in the accessible area of the phase space. Indeed, the *ergodic theorem* states that, in the infinite time limit, the system will explore all of its accessible phase space. It is then natural to introduce a phase space probability distribution function $f(\{p\}, \{q\}; t)$, so that the integral

$$\int_{\Delta q} \int_{\Delta p} \mathrm{d}^{3N}q \, \mathrm{d}^{3N} f(\{\vec{p}\}, \{\vec{q}\}; t) \tag{2.96}$$

is the probability of finding the system in the $\Delta p \Delta q$ hypervolume. The time evolution of the probability distribution function is described by the Liouville equation [148]. In statistical mechanics, once the equilibrium phase space distribution function $f(\{\vec{p}\}, \{\vec{q}\}; t)$ of a system is known, the value of any observable $a(x)$, with x indicating some combination of coordinates and momenta, can be obtained as an ensemble

average $\langle a \rangle$, defined by

$$\langle a \rangle = \int \mathrm{d}^{3N}p\, \mathrm{d}^{3N}q\, a(x) f(\{\vec{p}\}, \{\vec{q}\}; t), \tag{2.97}$$

or, equivalently,

$$\langle a \rangle = \lim_{T \to \infty} \frac{1}{T} \int_0^T \mathrm{d}t\, a(t) \approx \frac{1}{N} \sum_{i=1}^{N} a(i). \tag{2.98}$$

In MD simulations the simulation time is finite and discretized by the timestep: $T = N * \Delta t$. Thus MD ensemble averages are always calculated according to the right hand side of 2.98.

An important quantity related to $\langle a \rangle$ is its fluctuation, defined as

$$\langle \Delta a \rangle = \langle a - \langle a \rangle \rangle, \tag{2.99}$$

and depends upon the number of atoms in the system N according to $\langle \Delta a \rangle / \langle a \rangle \approx 1/\sqrt{(N)}$ [148]. In the so-called thermodynamic limit, N becomes infinite and all fluctuations reduce to zero, with all quantities having averages equal to their equilibrium values.

When a time-dependent external perturbation $F_e(t)$ acts upon the system, it will affect the equation of motion:

$$\dot{q}_i = \frac{\partial H}{\partial p_i} + C_i(x) F_e(t); \dot{p}_i = -\frac{\partial H}{\partial q_i} + D_i(x) F_e(t), \tag{2.100}$$

where $C_i(x)$ and $D_i(x)$ characterize the response of coordinates and momenta to the external force. If we wish to calculate how a is changed by the onset of $F_e(t)$, we should calculate first the variation of the equilibrium phase space distribution function $f(\{\vec{p}\}, \{\vec{q}\}, t)$, and then the ensemble average on the new distribution. To get it, we should solve the Liouville equation, which determines the time evolution of the probability distribution function. However, a direct calculation of the change of $f(\{\vec{p}\}, \{\vec{q}\}, t)$ is generally unfeasible.

Luckily, it can be demonstrated that, by solving the Liouville equation in the approximation of small external perturbations and performing some algebra, that

$$\langle a \rangle_{neq} = \langle a \rangle \mid_{eq} - \frac{1}{k_b T} \int_0^t \mathrm{d}s F_e(s) \langle a(t-s)j(0) \rangle, \tag{2.101}$$

where the equilibrium time correlation function $\langle a(t-s)j(0) \rangle$ appears and j, the dissipative flux, is defined as:

$$j(x) = -\sum_{i=1}^{3N} \left[D_i(x) \frac{\partial H}{\partial p_i} + C_i(x) \frac{\partial H}{\partial q_i} \right], \tag{2.102}$$

Equation 2.101 is a very important result of linear response theory, because it connects non-equilibrium ensemble averages (left hand side) to average of correlation functions performed using the equilibrium ensemble.

2.4.1.5   Periodic boundary conditions

Even a tiny droplet of liquid still contains an enormous amount of molecules: one nanoliter of water contains roughly 10^{17} atoms. Simulating this sheer amount of atoms is out of reach of any existent computer at the moment. However, the use of Periodic Boundary Conditions (PBC) allows to correctly represent thermodynamic ensembles, from which calculate the macroscopic quantities as ensemble averages.

In practice, the simulation box is replicated across all dimensions in space. Each atom in the primitive box will have its own image in every replicated box, in a way that whenever a bead exits from one side of the box, its image enters from the opposite wall (see figure 4). This ensures the conservation of the number of atoms. To calculate interactions, the minimum image convention is adopted, in which the distance r_{ij} between two atoms is always chosen as the smallest one between atom i and all images of atom j.
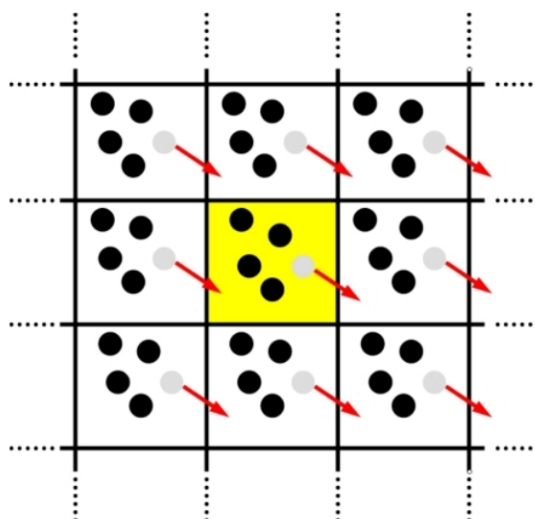
Figure 4: Illustration of periodic boundary conditions. The original simulation box is highlighted in yellow. The grey bead will leave the simulation box from the right wall, but will be replaced by its image coming from the right side.

It is clear that enforcing PBC constrains the minimum size of the simulation box, in the sense that no atom could directly interact with its own periodic image, and the same holds for entire molecules or polymers. Moreover, introducing a periodicity can influence all those phenomena characterized by length scales equal or larger than the simulation box. A size effects study is required for these cases, in which the same quantity is calculated for different sizes of the simulation box.

2.4.1.6 Thermodynamic ensembles

In MD, it is important to establish a connection between the simulated systems and the thermodynamic properties. The aim is to get the properties of a system at equilibrium conditions. A measurable O will always be expressed by its ensemble average value $\langle O \rangle$, in which the average may be performed over time and/or independent runs, and will be further characterized by its fluctuation $\langle \delta O \rangle$.

The most simple situation corresponds to a system described by the MD Hamiltonian 2.84 within a periodic box with dimensions and number N of particle fixed. This corresponds to the microcanonical or NVE ensemble, in which the number of beads, volume and energy are conserved. This ensemble is the preferred choice for data production, as it provides the bare dynamics of the system, without any external perturbation. Clearly, in equilibrium MD, NVE simulations make sense when the energy E corresponds to the equilibrium energy.

To reach equilibrium, however, the energy must be allowed to change. A canonical ensemble is obtained when a microcanonical ensemble is brought in contact with a thermal bath, allowing energy flow to and from the simulation box. In MD, this is done by coupling the system with a thermostat. In this context, temperature is a measure of the average kinetic energy of the atoms. Nosé and Hoover [149] showed that an additional degree of freedom could be added to the MD Hamiltonian,

$$H = U(\{q_i\}) + \sum_i \frac{p_i^2}{2m_i} + 3Nk_bT \ln s + p_s^2/2Q \tag{2.103}$$

in which the coordinate s and its momentum p_s were introduced. The Hamilton equations are:

$$\dot{q}_i = \frac{p_i}{m_i} \tag{2.104}$$

$$\dot{p}_i = -\nabla_{q_i} U(\{q_i\}) - \zeta p_i \tag{2.105}$$

$$\dot{\zeta} = \frac{1}{Q}\left(\sum_i \frac{p_i^2}{m_i} - 3Nk_bT\right), \tag{2.106}$$

in which $\zeta = p_s/Q$.

As it is clear from equation 2.106, when the system's temperature is larger(smaller) than the target value T, the bead momenta are decrease(increased), thanks to the damping factor appearing in the equations for $\dot{p}_i$. The parameter Q is the inertial mass of the thermostat, and needs to be chosen carefully, as a light mass would not be effective, while a heavy one would be too slow in dampening the fluctuations. In MD, the canonical ensemble obtained in this way is called NVT, as it conserves temperature instead of energy.

In a similar fashion, an additional degree of freedom, that is a barostat, may be added in such a way that it couples a target pressure P_e with the system's one, defined as the trace of the atomistic pressure

tensor $P_{\alpha\beta}$:

$$P_{\alpha\beta} = \frac{1}{V}\left(\sum_i^N m_i v_{i,\alpha} v_{i,\beta} + \sum_i^N r_{i,\alpha} f_{i,\beta}\right). \tag{2.107}$$

In this case, we have a isothermal-isobaric ensemble where pressure and temperature are conserved, thus it is called NPT.

The Nosé-Hoover thermostat and barostat has been proven to be non-ergodic. In simulation codes the chain variant of the Nosé-Hoover thermostat is actually used, in which additional thermostats are concatenated with the main one. This way, ergodicity can be restored and the reproduced ensemble truly identified with the canonical one.

In a different approach, the thermostatting can be achieved by the use of a Langevin thermostat. In this case, the total force on a bead i is the sum of the conservative force, a friction term and a random force term, $F_{i,tot} = F_c + F_d + F_r$, where

$$F_c = -\nabla_i U(q) \tag{2.108}$$

$$F_d = -\gamma v_i \tag{2.109}$$

$$F_r \propto \sqrt{\frac{k_B T m_i}{\gamma \Delta t}} \tag{2.110}$$

In this model, there is a dynamic friction term, with coefficient γ, and a random force. Both terms describe the interaction between the particle with a solvent at temperature T. This thermostat is particularly useful to simulate molecules in gas-phase, as the contribution from the random force allows for a broader and faster exploration of the possible configurations.

2.4.2   Modelling of molecules and forcefields

To treat accurately molecule in MD, the quantum mechanical interactions must be mapped into a set of empirical classical potentials. The set of potential function chosen for this scope and associated parameters is called a forcefield.

The main features that are expected from a forcefield are prediction accuracy and transferability, that is the possibility to use it to simulate molecules not originally included in the parametrization set, but still obtaining reliable results. One always desires the highest possible accuracy, but it must be traded off to ensure some degree transferability, otherwise a new parametrization, a lengthy procedure involving *ab initio* calculations and/or experimental measurements, should be carried on for every new molecule to investigate.

Up to date, a very large choice of different force fields exists, spanning application field and level of complexity. In this work, we will restrict ourselves to unpolarizable force fields, in which partial atomic

charged are fixed parameters.

In the following, the General Amber Force Field (GAFF) [89] is presented. It has been chosen as default MD force field in this work because a basic parametrization for isocyanates was already available, it is simple to modify and it is open-source.

2.4.2.1 GAFF bonded potential terms

GAFF is a non-polarizable, all-atom force field, initially designed starting form the AMBER force field to allow for simulation of small organic molecules in watery environment. Along the years, its application expanded over the initial intended use, including lipids, organic liquids, liquid crystals, and more [150, 151, 152, 153, 154].

A molecule is treated as a connected set of point-like massive and charged atoms. Bonded potential terms describe interactions between atoms which are in the same bond, angle or dihedral. The list of all those terms defines the molecule topology, and it is invariant during the simulation.

Chemical bonds are described by harmonic terms:

$$V_b(r_{ij}) = \frac{1}{2} K_b (r_{ij} - l_0)^2, \tag{2.111}$$

where K_b and l_0 are the bond force constant and the equilibrium bond lengths. Three bonded atoms in a row form an angle, which is described by:

$$V_a(\theta_{ijk}) = \frac{1}{2} K_\theta (\theta_{ijk} - \theta_0)^2, \tag{2.112}$$

θ_{ijk} being the angle between atoms i,j and k, and θ_0 the equilibrium value.

Dihedral energy terms describe the interaction between two terminal atoms of a dihedral. In GAFF, it is described by a set of cosine potentials:

$$V_d(\phi_{ijkl}) = \sum_{p=1}^{4} \left[\frac{V_p}{n} \left(1 + \sigma_k \cos(p \cdot \phi_{ijkl})\right) \right], \tag{2.113}$$

in which periodicities p are summed, up to $p = 4$. ϕ_{ijkl} is the dihedral angle, V_p the force constant and n the dihedral multiplicity (i.e. how many times it appears for the same 4-tet of atoms). σ is either +1 or -1, denoting the phase offset.

In some situations, 4 atoms could be bonded in such a way that a central atoms connects with all the others. This type of bonding often occurs in flat arrangements, and flatness should be enforced by means of an improper potential energy term:

$$V_i(\phi_{ijkl}) = \frac{K_i}{2} (\phi_{ijkl})^2 \tag{2.114}$$

where the improper dihedral ϕ_{ijkl} actually measures the out-of-plane deviation of the central atom.

2.4.2.2 GAFF atom specifications and non-bonded potential terms

Atoms in GAFF are defined not only by their atomic number, but also on their environment. For instance, type CT denotes a carbon atom in an alkyl chain, while C represent an sp2 hybridized carbon atom, such as in benzene. Their masses correspond to those of the most abundant nuclear isotopes.

Partial atomic charges are assigned starting from a HF calculation, performed using the 6-31G(d)[3] basis set, from which the electrostatic potential (ESP) is extracted. Next, point charges are located at the centre on each atom and kept fixed, and the values that best fit the ESP are taken. This method, known as restrained ESP (RESP) fit if a constraint on the magnitude of charges is used during the fit [155], results in slightly exaggerated charges, which are however retained as they model the polarization effect caused by water, a highly polar molecule.

Gaff forcefield includes non-bonded interaction by standard LJ (eq. 2.87) and electrostatic (eq. 2.88) terms. For each atom type, the pair of ϵ and σ is provided. When different atom types interact, the following sum rules apply:

$$\epsilon_{ab} = \sqrt{\epsilon_a \epsilon_b} \qquad (2.115)$$

$$\sigma_{ab} = \frac{\sigma_a + \sigma_b}{2} \qquad (2.116)$$

A set of scaling rules on how to apply non-bonded interactions to bonded atoms pairs completes the definition of GAFF. LJ and Coulomb interactions are neglected for atoms within the same bond and same angle. For 1-4 atomic pairs in the same dihedral, that is atoms separated by 3 bonds, they are scaled by a factor 0.5 and 10/12, respectively.

2.4.2.3 Fitting of dihedrals against DFT data

To obtain the dihedral parameters from ab-initio calculations, two different scans have to be performed for every dihedral: one using the quantum mechanical method of choice and the other using the force field energy function, excluding any dihedral contribution. This is necessary because, unlike in the case of bond and angle energy terms, non-bonded interactions between the 1-4 atomic pairs in the same dihedral are not excluded, thus contributing non trivially to the dihedral energy profile.

The difference between quantum and classical scans is finally fitted with the GAFF dihedral potential expression, equation 2.113, using V_i and δ_i as fitting parameters.

---

[3]The equivalent notation 6-31G* is often used in literature.

2.4.2.4   Final remarks

To use GAFF, a complete set of parameters must always be provided for the target molecule and, if absent, needs to be introduced and tested. This is due to the important issue of transferability retaining a reasonable accuracy. In general, any result coming from the use of a force field should be tested against experimental reference values of the highest possible quality, in order to assess the capabilities and limitations of the employed force field.

Due to the molecular fixed topology, simulation of chemical reactions are not allowed using GAFF and similar force fields. Likewise, since charges are predetermined and invariable, charge-transfer processes cannot be simulated. Both limitations might be surpassed by the aid of more complex methods, such as reactive and/or polarizable force fields, but at the cost of a significant reduction of treatable temporal and spatial scales because those methods require the dynamic calculation of partial charges, a very lengthy step. Therefore, if reactivity is not under interest, classical all-atom MD still represent one of the best ways to investigate the liquid state and its properties.

2.4.3   MD simulations in practice

2.4.3.1   Time and space scales of MD

Due to its nature, MD is intrinsically heavily parallelizable and scales very well with the number of CPUs. However, to obtain good energy conservation under NVE conditions, the timestep in for all-atom simulation should be lower than 1 fs for temperatures not greater than 400 K. In MD simulations presented here, 1 fs timestep was used with a 3-level RESPA algorithm, corresponding to an innermost timestep of 0.125 fs. With the resources typically available to our group, simulation speeds of 0.5-1 nanoseconds/day were obtainable for systems containing ca 20000 atoms. All MD simulations in this work were performed using LAMMPS [156].

2.4.3.2   From system creation to data production

To perform a simulation of N molecules in a disordered liquid phase, we need to ensure that the initial system is randomized both in molecular orientation and in their conformation. To achieve this, the initial box is created at very low densities (below 0.1 g/cm^3). Subsequently, all dimensions and coordinates are scaled by a factor of 0.9, thus reducing the simulation box volume , and a small 10 ps step run is run under NVE conditions imposing an upper bound on the atomic displacement per step of 0.1 Å. This type of run is very efficient in removing accidental overlaps and randomizing initial conformations, and the

constrain prevents the system to became unstable due to the high forces generated in this phase.

This step is repeated until a density larger than 0.7 g/cm^3 is obtained. The final state is then used as a 500 ps simulation at 500 K and 1 atm, using NPT conditions and Nosé-Hoover thermo- and and barostatting, with damping constants of 0.1 and 1 ps^{-1} respectively. The system is then equilibrated at the target temperature T_{eq}, under NPT conditions until twice the time required for total energy to reach stationarity. The last 100 ps of equilibration time are used for sampling the system's equilibrium density $\langle \rho \rangle$.

Some care must be taken to pass from NPT to NVE conditions, in order to start the NVE trajectory from a point as close as possible to its equilibrium values of density and energy. After equilibration, a small 1500 fs run is performed under NPT condition in order to pick up a system state with ρ as close as $\langle \rho \rangle$, which is used for a 100 ps run under NVT conditions. A further 150 fs run under NVT conditions is performed to pick up a state with the temperature as close as the target temperature.

At this point, the system is ready for data production under NVE conditions, which is carried on for several nanoseconds. At this stage, systems snapshots, that is files containing all atoms coordinates and velocities at a given time are saved at regular 20 ps intervals for later analysis, and system thermodynamic variables are printed out every 3 fs.

When simulating a system in which a 2D material sheet is present, generally in the xy plane, the periodicity is removed from the z direction, and a large amount of vacuum along z is added. The sheet is created of the desired size according to their crystal structure, and is centre of mass is kept fixed to avoid any drift motion. Once the sheet is equilibrated, other molecules can be added in the desired quantity to wet the surface. To avoid them to escape from the upper side of the box, a reflective wall is enforced, which change the verse of the normal component of momentum of each incoming atom. A layer of vacuum is always kept between the liquid and the upper side of the box, in order to let the liquid to create a liquid-air interface. While thermostatting is implemented in the same way as for fully periodic systems, the barostat is coupled only to the x and y directions.

For gas phase simulations, a cubic simulation box of 200 Å length, containing a single molecule, is used without periodic boundary conditions. A very large cutoff for non-bonded interactions should set to avoid any approximation in potential energy calculation and random initial velocities with zero total angular and linear momentum were assigned to all atoms. To calculate the total potential energy $\langle U_{gas} \rangle$, a 25 ns long simulation with a time step of 0.25 fs applying a Langevin thermostat with a damping constant of 10 ps^{-1} was performed. Simulation data was sampled every 1.25 ps, with the first 300 ps of the simulation regarded as equilibration and discarded.

2.4.3.3   Radial pair distribution function

The radial pair distribution function [157] $g(r)$ is the probability that, given a bead i at $\vec{r}_i$, another bead j can be found at a distance $r = |\vec{r}_i - \vec{r}_j|$, and it is very useful in describing the local structure of any dense system. For a system of N beads, it is defined as:

$$g(r) = \frac{V}{4\pi r^2 N(N-1)} \left\langle \sum_{i=1}^{N} \sum_{j\neq i}^{N} \delta^3 (r - r_{ij}) \right\rangle, \qquad (2.117)$$

where the brackets denotes an ensemble average. It is normalized in such a way that

$$\int_0^R 4\pi r^2 \rho g(r) \, \mathrm{d}r = N_R, \qquad (2.118)$$

where ρ is the system's density and N_R is the number of beads within a sphere of radius R.

2.4.3.4   Enthalpy of vaporization

The enthalphy of vaporization ΔH_{vap} is the enthalpy necessary to remove a molecule from a liquid and bring it in a gas phase. Therefore, it is a good descriptor of the liquid's cohesive forces. It is calculated using the following equation [158]:

$$\Delta H_{vap} = U_{gas} - U_{liq} + RT + \frac{1}{2}R\left(<T_{liq}> - <T_{gas}>\right)(3N_{atoms} - 6) \qquad (2.119)$$

where T is the system target temperature, U_{gas} and U_{liq} the potential energy per molecule for the gas and the liquid phase, respectively. The last term appearing in (2.119) is a correction term that takes into account the difference between the gas phase temperature $\langle T_{gas} \rangle$ and the liquid phase temperature $\langle T_{liq} \rangle$ extracted from the simulation.

2.4.3.5   On the calculation of viscosity

The shear viscosity is a key macroscopic property of a liquid, as it describes its resistance to undergo a shear flow. Liquids show a very large variation of viscosity values, ranging from 1 mPa·s of water to several Pa·s of honey. Viscosity is strongly dependent upon temperature, and for glass-forming systems it may change by 10 or more orders of magnitude within a narrow temperature window, undergoing into what is called a glass transition [159].

Let us consider a system consisting in a liquid trapped into two parallel walls located at $-y_0$ and $+y_0$ and oriented normally with respect to the y axis, moving in opposite directions along the x axis. As result of friction forces, the walls' motion will induce a velocity field $\vec{u}$ in the fluid. If the system is infinite in the x and z directions, the velocity profile can only depend on y, i.e. $\vec{u} \equiv u_x(y)\hat{x}$. The viscosity η is thus

defined as the proportionality constant between the shear stress of two adjacent layers of fluid and the transverse velocity gradient:

$$\sigma_{xy} = \gamma\eta, \tag{2.120}$$

where γ is the shear rate (as the velocity profile is linear, its gradient is a constant) and σ_{xy} is the xy component of the stress tensor, that is the flow of momentum oriented along direction x across a surface with normal versor parallel to y.

There is a family of relationships, known as Green-Kubo (GK) formulae [160], that allows to calculate the transport coefficients from the equilibrium time autocorrelation functions of the system. An in-depth derivation of GK formulae and linear response theory upon which they are based can be found in [161], while here we will follow the exposition of Tuckerman [162].

In the presence of a velocity gradient as described in 2.120, the equation of motion of the system are:

$$\dot{q}_i = \frac{p_i}{m_i} + \gamma y_i \hat{x}; \tag{2.121}$$

$$\dot{p}_i = F_i - \gamma p_{y_i} \hat{x}. \tag{2.122}$$

To apply 2.101 to viscosity, a microscopic definition of the stress tensor should be given:

$$\sigma_{\alpha\beta} = -\frac{1}{V}\left(\sum_i^N m_i v_{i,\alpha} v_{i,\beta} + \sum_i^N r_{i,\alpha} f_{i,\beta}\right). \tag{2.123}$$

Using 2.123, the viscosity definition can be recast as:

$$\eta = \lim_{t\to\infty} \frac{\langle\sigma_{xy}\rangle_{neq}}{\gamma}, \tag{2.124}$$

where now the stress tensor refers to the perturbed system, and the time limit is taken to remove any transient effect, and $< \sigma_{xy} >_{neq}$ can be obtained using 2.101. To do so, it is easy to show that for a liquid between two moving walls, we have, by comparing with equations 2.100, $C_i(r,p) = \gamma y_i \hat{x}$ and $D_i(r,p) = -\gamma p_y \hat{x}$. The dissipative flux is then:

$$j(r,p) = -\gamma V \sigma_{xy}. \tag{2.125}$$

Considering $F_e(t) \equiv 1$, equation 2.101 may be written for $\langle\sigma_{xy}\rangle_{neq}$:

$$\langle\sigma_{xy}\rangle_{neq} = \langle\sigma_{xy}\rangle_{eq} + \frac{\gamma V}{k_B T}\int_0^t d\tau \langle\sigma_{xy}(\tau)\sigma_{xy}(0)\rangle \tag{2.126}$$

and, substituting with 2.124 and taking the time limit, we finally obtain:

$$\eta = \frac{V}{k_B T}\int_0^\infty dt \langle\sigma_{xy}(t)\sigma_{xy}(0)\rangle, \tag{2.127}$$

The GK formula 2.127 presents several advantages: it can be obtained from equilibrium simulations (possibly in NVE ensemble) and it directly gives the zero-shear viscosity, whereas nonequilibrium methods generally require an extrapolation. On the other hand, there are some caveats to be addressed. First of all, stress tensor components need to be sampled finely in time to ensure a good description of the fast stress oscillations, resulting in large amount of generated data. Most importantly, the stress autocorrelation function may take a very long time to converge because, as the viscosity increases, so do relaxation times, and convergence would require impractically long simulation times. However, the simulation cannot be too long, because the accumulation of numerical integration errors will start to be important.

The computational implementation of GK viscosity formula is slighty different from 2.127, which allows to divide the simulation in many short time windows t_W to improve statistics [163]:

$$\eta = \frac{V}{10k_bT} \left\langle \int_{t'}^{t'+t_W} \sigma_{ij}\left(t+t'\right) \sigma_{ij}\left(t'\right) \, \mathrm{d}t \right\rangle \tag{2.128}$$

where a sum over all components of the traceless stress tensor σ_{ij} is understood and angular brackets indicate average over different possible time origins t', separated by t_s =15 fs. The time window span t_W should be picked as the minimum time that guarantees include stress autocorrelation integral convergence, and clearly is specific to every system (and temperature). The uncertainty on viscosity was estimated calculating, for each run, the standard deviation of the converged values of the stress autocorrelation integral of each of the traceless pressure tensor components.

2.4.3.6   Free energy estimates with adaptive biasing force method

In many cases, the bare interaction energy between two subsets of a system, such as two molecules or a molecule and a surface, is not sufficient to describe the stability of these assembles, because the effects of temperature and size of conformational space, that is entropy contributions, are not taken into account.

A better descriptor in this sense is the free energy G, defined as $G = U - TS$, and in particular the free energy difference ΔG between two reference states, generally a bound state and one in which the constituents are taken apart and do not interact any more. It is thus clear that to calculate ΔG we need a very long trajectory to have a good sampling of the accessible conformation space at some temperature T. However, in a plain calculation, the interacting moieties could be trapped into an energy minimum and/or locked in some stable conformation, with the effect of greatly reducing the conformational sampling. To overcome this problem, several methods have been developed to speed up the sampling and obtain reliable free energy estimates. In this thesis, the adaptive biasing force (ABF) [164, 165] has been adopted. It applies when the phenomenon under interest is described by one *collective variable* (CV) ξ. The free

energy, as a function of ξ, with a probability distribution $P(\xi)$ is:

$$G(\xi) = -lnP(\xi) + G_0,\tag{2.129}$$

and its gradient can be estimated by the average of the forces, at fixed ξ [166]:

$$\nabla_\xi G(\xi) = \langle -F(\xi) \rangle \, |_\xi.\tag{2.130}$$

Once ξ and its boundaries are defined, a simulation at the desired temperature and pressure conditions is run, and CV values are sampled in order to accumulate $F(\xi)$. After a certain number of samples the ABF algorithm adds a fictitious force F^{ABF}, the biasing force, proportional to the sampling, in order to overcome eventual energy barriers, according to

$$F^{ABF} = \alpha(N_\xi)\nabla \tilde{A}(\xi),\tag{2.131}$$

where $\alpha(N_\xi)$ is a scaling factor growing for 0 to 1 as the number of samples increases, and $\tilde{A}(\xi)$ is the current estimate of the free energy gradient. The algorithm continues additively and is converged when ξ has an uniform probability to have any value comprised in its boundaries: the biasing force has 'filled' completely the free energy surface (at least its projection on ξ). The final result is the integrated free energy gradient, or potential of mean force (PMF), from which ΔG can be extracted.

2.5   Polymers and Dissipative Particle Dynamics

This section contain some elementary notions of polymer physics, necessary to understand the dissipative particle dynamics simulation method. The exposition is based upon the book of Pierre-giles De Gennes [167].

2.5.1   Polymers

A polymer is a large molecule constituted by repeating units linked between them, called monomers. Depending upon their connectivity, they could be linear, when the monomers are organized in a chain-like structure, or branched, when there are junctions connecting more chains within the same polymer. In this case, the junction points are termed crosslinking (CL) points.

A polymer made of N monomers can be described by a random walk in 3 dimension of N steps of equal size α , having one polymer end as origin of the walk. Each step connects two adjacent monomers and α represents their bond length. The end-end vector $\vec{R}_{ee}$, the vector joining the polymer ends, is defined as:

$$\vec{R}_{ee} = \sum_{i=1}^{N} \vec{a}_i,\tag{2.132}$$

If the steps are completely uncorrelated, that is $a_n \cdot \vec{a}_m = \alpha^2 \delta_{nm}$, then

$$R_{ee}^2 = \sum_{a,b=1}^{N} \vec{a}_a \cdot \vec{a}_b = \sum_{a=1}^{N} |\vec{a}_a|^2 = N\alpha^2, \tag{2.133}$$

which implies that $R_{ee} \propto N^{1/2}$. A chain that obeys this relationship is termed ideal.

The probability for a chain of N beads of having an end-end radius of r is given by:

$$p(r) \approx \frac{1}{N^{3/2}} e^{\frac{-3r^2}{2N\alpha^2}}. \tag{2.134}$$

with an associated entropy of

$$S = \ln(p(r)) \approx -\frac{3r^2}{2N\alpha^2} \tag{2.135}$$

up to an additive constant. If the free energy $U - TS$ is written, we obtain:

$$F = F(0) + \frac{3Tr^2}{2R_{ee}^2}, \tag{2.136}$$

which shows how, by pushing or pulling both ends of the polymer, an elastic, spring-like, force of entropic origin is generated.

The contour length L is defined as

$$L^2 = \sum_{i=1}^{N} |\vec{a}_i|^2. \tag{2.137}$$

L is a fixed quantity and it is clear that $R_{ee} \leq L$.

The ideal picture does not always hold, but it is correct in dense polymer melts [167]. In other situations, as for a free chain in solvent, excluded volume effects must be taken into account, and the radius of a polymer does not obey anymore a Gaussian distribution, as in equation 2.134, but it can be shown that $R_e e \propto N^\nu$, with ν very close to 0.6. Apart from excluded volume effects, the polymer flexibility is also a factor to consider. Polymer chains are not fully flexible, but would display a force against bending. Since monomers cannot overlap, a certain degree of stiffness is always present in every chain. However, it is possible to define a length a_k in a way that

$$R_{ee}^2 = N_K a_k^2. \tag{2.138}$$

The *Kuhn length* of a polymer is that quantity that, for any given chain, allows to describe it as an ideal random walk of $N_k < N$ steps a_k wide. The stiffer the polymer, the larger a_k.

One of the main issues in simulating polymers is that it might be very difficult to obtain an equilibrated system because the relaxation processes might have very long time scales, especially for longer chains. It might be useful to calculate the mean squared internal distance (MSID) $R^2(|i - j|)$, which simply is the

square distance between monomers i and j of the same chain. When stiff chains are under investigation, then it is expected that the MSID follows [168]:

$$R_{ee}^2(n) = n\alpha^2 \left(\frac{1+\cos\theta}{1-\cos\theta} - \frac{1}{n} \frac{2\cos\theta(1-\cos^n\theta)}{(1-\cos\theta)^2} \right), \qquad (2.139)$$

where $\cos\theta$ is the angle between adjacent bonds. By explicitly calculating the MSID from a simulation and comparing it with the prediction of 2.139, it is possible to check whether the simulated polymer melt is in equilibrium or not, because non equilibrated systems would show significant deviations from 2.139.

It is known that polymer melts display many *entanglements* between chains. Their presence strongly influence the mechanical and dynamic properties of the system, and it is very important to well-represent it in the simulated melt. To gain information upon the entanglement state of the system, a primitive path analysis (PPA) [169] should be performed. Given a chain in a melt, a primitive path (PP) is the shortest path between its ends that preserves the entanglements of the chains. If the chain is unentangled, the primitive path will be reduced to a straight segment, and its contour length will be equal to R_{ee}. The presence of entanglements will result as the appearance of 'kinks' (that can be counted) and cause the PP contour length to increase. The PPA provides a way to characterize the entanglement state of any polymer, an can be applied to polymer networks as well. In this work (chapter 5) chains up to N=40 have been simulated, and the PPA analysis has been done using the Z1 code [170, 171, 172, 173], kindly provided by prof. Martin Kröger.

2.5.2 Flory-Huggins theory

Flory and Huggins developed a mean field theory to investigate the phase behaviour of polymer-solvent mixtures. The mean field refers to the polymer concentration ϕ, assumed to be uniform in space, hence disregarding any local density fluctuation. To make the derivation clearer, a lattice model is assumed for a system containing a solvent and polymers made of N beads. Each of the solvent or polymer monomers can occupy one lattice site at the time, and overlap is forbidden. In this section, the convention $k_B T = 1$ is adopted, and all thermodynamic quantities are expressed per site. Under these conditions, the entropy S per site is:

$$S(\phi) = \frac{\phi}{N} \ln(\frac{\phi}{N}) + (1-\phi)\ln(1-\phi), \qquad (2.140)$$

where the first term on the right side is the entropy associated to the polymer and the second one of the solvent. The entropy of mixing S_{mix} is given by:

$$S_{mix} = S(\phi) - \phi S(1) - (1-\phi)S(0) = \frac{\phi}{N}\ln\phi + (1-\phi)\ln(1-\phi), \qquad (2.141)$$

that is the mixing entropy is the difference between the system's entropy and that of the (weighted by concentration) pure phases.

The internal energy per site can be assumed to be made of three pair contributions describing monomer-monomer, monomer-solvent and solvent-solvent interactions:

$$U = \frac{1}{2}\chi_{mm}\phi^2 + \chi_{ms}\phi(1-\phi) + \frac{1}{2}\chi_{ss}(1-\phi)^2 \tag{2.142}$$

where the χ_{ij} contain information upon the strength of the pair interaction between different species. The energy of mixing is obtained as S_{mix} and can be written as:

$$U_{mix} = \chi\phi(1-\phi) + \text{costant and linear terms} \tag{2.143}$$

where $\chi = \chi_{ms} - \frac{1}{2}(\chi_{mm} + \chi_{ss})$ is the Flory-Huggins parameter. To understand its role, the free energy of mixing can be written:

$$F_{mix} = U_{mix} - TS_{mix} = \chi\phi(1-\phi) + \frac{\phi}{N}\ln\phi + (1-\phi)\ln(1-\phi). \tag{2.144}$$

Equation 2.144 allows to determine the expected concentration of the polymer as a function of the Flory-Huggins parameter. For good solvents, χ is small and low polymer concentrations are found, meaning that it is effectively solvated. For a bad solvent, χ is large and very high polymer concentrations are predicted, hence a net separation between solvent-rich and polymer-rich phases is expected.

2.5.3   Polymer networks

A *gel*, or polymer network, is obtained when the polymer chains are merged together in one single macro-molecule. The points which join different chains are called crosslinking (CL) points, and the chain between them is an elastic strand. The functionality ν represents in this context the number of bonds hosted by the CL bead, and it must be $\nu \geq 2$ to have a network. In this thesis, crosslinking is always understood as an irreversible process which creates new chemical bonds between CL points and attached chains. Other forms of crosslinking were not considered.

When immersed in a solvent, some of the solvent molecules will migrate into the polymer-rich phase, causing the gel to swell. The process will stop when the chemical potential of solvent molecules within the gel and outside is equal, and this is obtained when the solvent pressure outside it matches the one inside, in which region the excess pressure is provided by the network stress. The swelling capability will thus depend both on the network elastic properties and on the solvent strength, and its knowledge is helpful to characterize the elastic response of it.

In an ideal network, every chain has the same length, i.e. are *monodisperse*, and connects two different CL points. Under a deformation, these will move and the strand will give rise to an elastic force, as a consequence of 2.136. Based upon this, several model exists, such as the affine and phantom

network [174] that, starting on the concentration of CL beads and elastic strands, can predict the elastic moduli, however they apply only for ideal networks and neglect the entanglements. Unfortunately, real networks are by no means ideal. The network structure will contain many defects, mostly dandling ends and loops which bring no contribution to the network elasticity and a certain degree of dispersity, affecting the behaviour of single chains.

2.5.4   Dissipative Particle Dynamics

Dissipative Particle Dynamics (DPD) [175, 176, 177] is a theory that has been developed to reproduce the phase separation and solvation of polymers. DPD beads are coarse-grained representations of one -or more- monomer. Any DPD particle i is subject to the DPD force f_i, similar to the Langevin dynamics force term, composed by a pair term F_C, a dissipative term F_D and a random force term F_R:

$$\vec{f_i} = \sum_j \left(\vec{F}_{C,ij} + \vec{F}_{D,ij} + \vec{F}_{R,ij} \right) \tag{2.145}$$

$$\vec{F}_{C,ij} = a_{ij} w(r) \hat{r}_{ij} \tag{2.146}$$

$$\vec{F}_{D,ij} = -\gamma w^2(r) \left(\hat{r}_{ij} \cdot \vec{v}_{ij} \right) \hat{r}_{ij} \tag{2.147}$$

$$\vec{F}_{R,ij} = \sigma w(r) \theta_{ij}(t) \hat{r}_{ij} \tag{2.148}$$

$$w(r) = 1 - \frac{r}{r_c}, \tag{2.149}$$

where the sum runs over all different particles j at distance r_{ij} and r_c is the cut-off radius of DPD interactions, set to $r_c = 1$. The function $\theta_{ij}(t)$ is a randomly fluctuating variable [176, 177], the damping factor γ is set equal to 4.5 and $\sigma^2 = 2kT\gamma$. The pair repulsion parameters a_{ij} describe the interaction between beads, and provide a purely repulsive term. With a density fixed at $\rho = 3$ DPD units, the value of a_{ii} is set to $a_{ii} = 25$. This choice correctly reproduces the liquid water compressibility [177].

The major difference with MD methods is that the interaction potential is *soft*, in the sense that the DPD pair potential, unlike the Lennard-Jones one, is finite and well defined at the origin, meaning that beads can largely overlap. This allows for intrinsically larger time-steps during the simulation, as it does not provoke the appearance of steep gradients and, by consequence, large forces.

When DPD is applied to simulate polymers, special care must be taken in order to avoid the unphysical chain crossings made possible by the soft-core potential. These topology violations artificially enhance the polymer diffusion in melts and disrupt permanent entanglements in networks. The segmental repulsive potential [178] (SRP) prevents this by adding repulsive potentials between middle points of bonded atoms.

Remarkably, the a_{ij} are connected to the Flory-Huggins parameters χ_{ij} [177], which in turn may be

related to Hildebrand solubility parameters [179]:

$$a_{ij} = a_{ii} + 3.27\chi_{ij} \tag{2.150}$$

$$\chi_{ij} = \frac{v_{ij}}{RT}(\delta_i - \delta_j)^2 \tag{2.151}$$

$$\delta_i = \left(\frac{\Delta H_{vap} - RT}{v_i}\right)^{0.5}, \tag{2.152}$$

where ΔH_{vap} is the enthalpy of vaporization, and v_i, v_{ij} are the molar and partial molar volume, respectively. These equations thus indicate a bottom-up approach to obtain the a_{ij} from atomistic simulations [180]. The top relationships also shows that large a_{ij} values describes species with poor mixing behaviour.

The definition of the pair repulsion parameters on the basis of the Flory-Huggins theory makes DPD particularly suited for simulations of polymers in solution and mixtures of species with different hydrophilicities, as well as for investigating the swelling properties of polymer networks, in which the swelling transition is easily induced by tuning the solvent-gel interaction strength.

Before going further, it should be noted that the DPD pair potential is purely repulsive, hence it cannot reproduce polymer surfaces or interfaces without introducing impenetrable walls in the system, or fictitious 'air' beads with a very large $a_{liq-air}$. For these situations, not encountered in this thesis, there exists generalizations, which are well discussed in [181]. Apart from that, equilibration and data production stages are analogous to those of all-atom MD simulations.

2.5.5   Modelling of chemical reactivity

In experimental situations, the preparation time of crosslinked polymer networks can take from minutes to days to be fully reacted, depending upon the reactants employed and the temperature/pressure conditions. The chemical reaction itself, in general, is a rather complex process that can be fully understood only from a quantum mechanical perspective. Although these considerations seems discouraging at first glance, it is possible to provide a simple model in many cases.

A crosslinking reaction falls in this category because it mainly involves bond formations between monomers, it is the dominant -and faster- process in the system and its final state is not reversible. Under these conditions, the chemical process can be seen as a series of bond creations between beads, allowed to react whenever they are closer than some threshold value and with a pre-determined probability, lower than unity, to occur. Bond breaking, if present, can be treated exactly in the same way, allowing to take into account reversible crosslinking or other polymer degradation mechanisms. This method has been widely used [182, 98, 183] whenever the network formation process from a disordered melt is required, and

has the advantage of providing realistic structures, obtained from equilibrated melts and letting naturally appear all those features, such as network defects, present in real systems.

During the simulation, reaction steps are repeated as many times as required and alternated with diffusive phases, where no reaction occurs. This is necessary because, any bond creation/deletion change the status of two neighbouring beads, causing the instantaneous appearance (or disappearance) of pair and bond forces. To avoid simulation instabilities, the system must be given the proper time to relax these stresses, and also to allow all the species to diffuse. The number of reaction steps required to obtain a fully reacted network depends upon the reactant concentration and reaction speed, codified by its threshold and probability. Actually, fully reacted final states are unlikely to be obtained in simulations, as with time the concentration of reactants decreases until reaction become very rare, unless some attractive potential between reactants is introduced to speed up the process [184].

Alternatively, the system can be prepared already in a crosslinked structure, in which CL points are joined with chains of desired length and up to the desired functionality. The CL points might be randomly or evenly distributed in space, depending on whether a random or regular network is desired. This method is almost instantaneous when compared with the reaction-driven and avoids many network defects, at the cost of neglecting entirely diffusion and relaxation of chains during the formation process. How this affects the elastic and swelling properties of networks, will be discussed in chapter V.

2.5.6 Characterization of nanogels

In chapter V, nanogels are employed rather than periodic network to characterize their swelling properties, because their non-periodicity allows the nanogel to reach the equilibrium in the swollen state by adjusting the quantity of solvent within them. To achieve this, nanogels are put in a simulation box containing solvent beads in excess, and with a box size large enough to exclude self-interactions of the nanogel in swollen state. In a bad solvent they are collapsed and assume a spherical shape. The gyration radius R_g is defined as

$$R_g^2 = \frac{1}{N} \sum_{i=1}^{N} (\vec{r}_i - \vec{r}_{CM})^2,$$
(2.153)

where N denotes the number of beads in the nanogel and $\vec{r}_{CM}$ its centre of mass position. R_g^2 can be regarded as an estimator of the nanogel size, especially useful in the swollen state, in which nanogels assume a less spherical shape and have less defined boundaries. Clearly, when the solvent-gel interaction parameter changes, $R_g \equiv R_g(a_{sg})$. In terms of R_g, The swelling ratio might be defined as the ratio between $R_g(a_{sg})$ and the radius of gyration of the collapsed nanogel $R_{g,c}$,

Further insight on the nanogel structure can be obtained considering the radial density profile $\rho(r)$,

defined in such a way that:

$$\int_0^\infty 4\pi r^2 \, \mathrm{d}r \rho(r) = N, \tag{2.154}$$

N being the number of beads of the nanogel. Another useful quantity is the form factor $P(q)$, defined as

$$P(q) = \frac{1}{N} \sum_{i,j=1}^n e^{-i\langle \vec{q}(\vec{r}_i - \vec{r}_j)\rangle}, \tag{2.155}$$

where the sum runs over all the nanogel beads and angle brackets indicate an average over time and over

the possible directions of $\vec{q}$.

Chapter 3

Development of a molecular dynamics force field for isocyanate liquids

This chapter illustrates the development, testing and application of a classical molecular dynamics force field for aliphatic isocyanates and polyisocyanate liquids. After briefly discussing the motivation, the force field reparametrization technique is presented, and used to calculate the viscosity of several isocyanurate systems. Finally, the possibility to estimate low-temperature viscosities from higher-temperature calculations is discussed Sections 3.1 and 3.2 are based on the publications "GAFF-IC: Realistic Viscosities for Isocyanate Molecules with a GAFF-based Force Field" [185] and "Aliphatic isocyanaturate and polyisocyanate networks" [10].

3.1   Motivation

Aliphatic isocyanurates are mainly used for the production of polyurethane coatings and adhesives. Although providing superior resistance properties, their use is hindered by their high viscosity, which limits their possible processing routes and renders their mixing with other components a difficult task. For commercial-grade isocyanurate trimer products based upon hexamethylene diisocyanate, viscosities of 1000-3000 mPa·s are reported at room temperature, to be compared to the low viscosity of their precursor, 2.3 mPa·s [186]. Whereas the addition of solvents could improve their processability, current research efforts are aimed at avoiding this, both to develop a more sustainable process and to limit the emission of volatile organic compounds (VOCs), a matter of rising concern especially for coatings and adhesives.

Experimental measurements of viscosity at room temperature on high-purity samples of functional

and non functional isocyanate trimers [10] liquids are reported in figure 5. To change their size, aliphatic mono- and diisocyanates with different number of CH_2 groups in the alkyl chain were used as precursors, and very high purity samples (above 99 %) were obtained by distillation techniques.
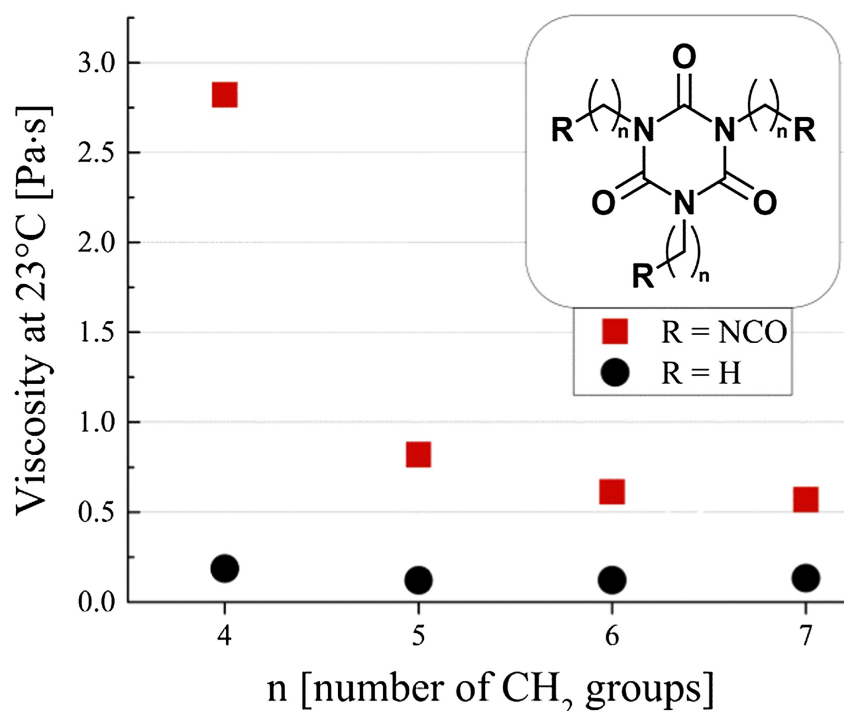
Figure 5: Experimental viscosity measurements on a series of isocyanate trimers, which structure is reported in inset. Red squares indicate functional molecules, while black dots represent non-functional ones.

It was found that the viscosity of aliphatic isocyanurates follows complex structure-property relationships, with higher viscosities observed for lighter molecules as well as large differences between non functional and functional trimers. However, it is not clear which mechanism governs the viscosity of polyisocyanates. From an experimental point of view, there is no trace of any typical binding mechanism distinctive of isocyanurates with respect to isocyanates. The search for low viscosity formulations is indeed of high industrial interest [187, 188], and it will be certainly accelerated if rheological properties of these liquids could be understood.

To achieve this, molecular dynamics simulations, in conjunction with a force field capable of accurate, *quantitative*, predictions, seem to represent an ideal choice, due their ability to connect molecular-scale features to macroscopic observables. Among the possible choices, the GAFF [89] force field already contained non-bonded parameters for the NCO group atoms, and reproduced reasonably well the density at 298 K and 1 atm of many isocyanate liquids. However, when the viscosity of an HDI liquid was calculated, an overestimation of at least one order of magnitude was found, providing, at 293 K and 1 atm, a value of 22.3 mPas against the reference value of 2.3 mPas [186].

Therefore, a reparametrization of the original force-field for the isocyanate molecule family was necessary. This approach has been successfully applied using GAFF as the starting point to investigate a wide class of different systems, such as hydrocarbons, lipids, liquid crystals, and ionic liquids [153, 189, 151, 190, 152, 154]. In the following sections, we will illustrate the steps undertaken to optimize the GAFF force field, and how this dramatically improved the simulation predictions.

3.2   Optimization of force field parameters

3.2.1   Definition of the molecular test set

To carry out the optimization of the force field parameters, a test set of isocyanate based molecules (figure 6), namely, methyl isocyanate (MIC), Ethyl isocyanate (EIC), Butyl isocyanate (BIC), hexamethylene diisocyanate (HDI), octadecyl isocyanate (ODIC) was defined. All these species contain at least one isocyanate group and span a wide range of molecular weights and the choice was restricted to those molecules for which quality reference data is available.

3.2.2   Optimization of bonded and non-bonded parameters

The starting point of the reparametrization is to verify if the force field's equilibrium values for bond and angles are correct. Isocyanate and isocyanurate group optimized geometries were obtained at the B3LYP-D3/6-311++G(d,p) level of theory, and the bonded potential lengths adjusted to the DFT-derived data. This step ensures a better match of the molecular conformations obtained from classical and quantum calculations, but will not improve significantly those observables that depend on the intermolecular forces, described by Lennard-Jones and Coulomb potentials. In fact, while the ring structure was already well-described by the default GAFF parameters, some adjustments were required for the NCO groups bond and angle values. A full list of the optimized parameters is presented in Appendix A.

It was decided to take the system's equilibrium density ρ and its enthalpy of vaporization ΔH_{vap} as target functions for the optimization of non-bonded energy parameters, because they are closely related with the liquid's cohesive forces. For the purpose of this study, the MIC molecule was considered, which is the simplest one in the test set, consisting of an isocyanate group attached to a methyl group. Its geometry is such that no dihedral terms are needed to properly parametrize it, making it an ideal candidate to study the non-bonded interactions of the NCO group.

MIC ρ and ΔH_{vap} were calculated using liquid phase simulation under NPT conditions and gas phase
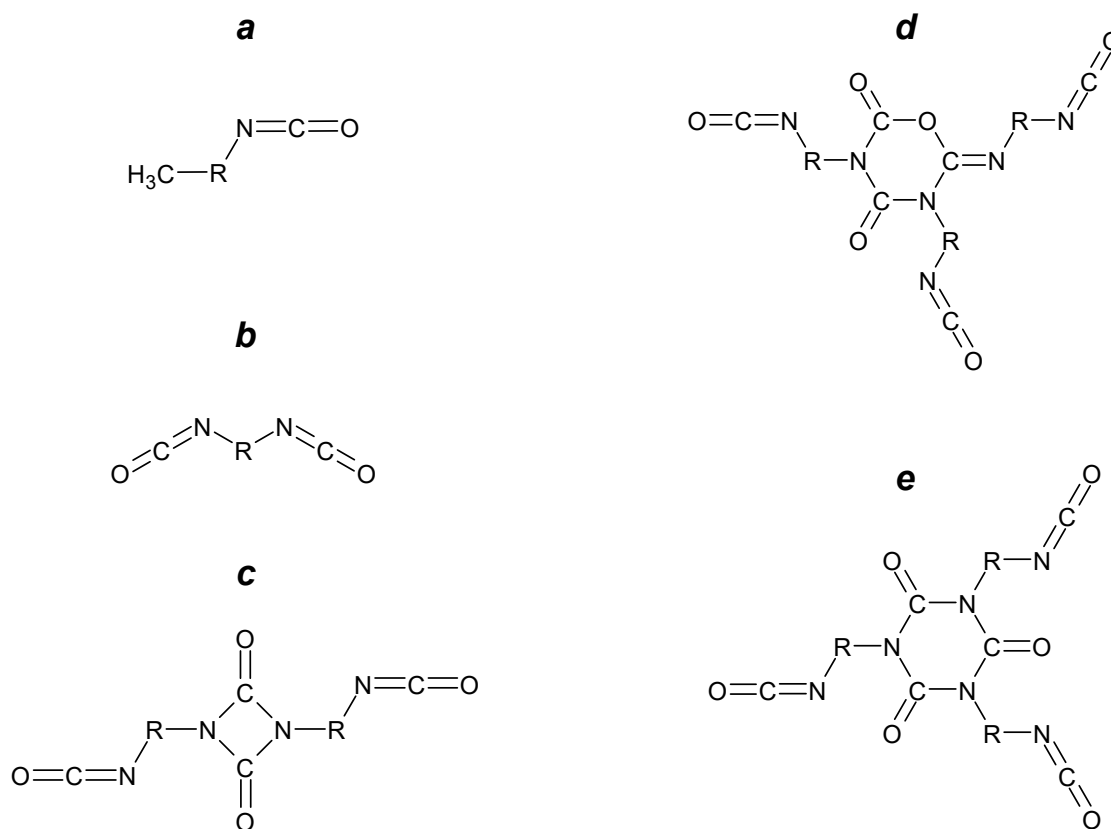
Figure 6: Overview of aliphatic isocyanates considered in this work. In all formulas, R represents an alkylene group: $R = -(CH_2)_n-$, where n is the number of carbons. Monoisocyanates (MIC, BIC, EIC and ODIC) (a), diisocyanates (HDI) (b), isocyanate dimers (UDI) (c), the asymmetrical (A3HDI) (d) and symmetrical (3HDI) (e) isocyanate trimers.

simulations under NVE conditions, both at temperature and pressure of 293.15 K and 1 atm. When compared against the reference values listed in table 1, the unoptimized GAFF overestimates density and vaporization enthalpy by $8\,\%$ and $42\,\%$ respectively, in line with what was reported elsewhere [151, 150, 152], indicating that liquid cohesive forces are exaggerated by GAFF.

One way to correct this overestimation, is by scaling the atomic charges as done in the case of simulations of ionic liquids in the MDEC model [195, 189] where a scaling factor of $\frac{1}{\sqrt{2}}$ was adopted. To understand this step, it should be taken into account that the original GAFF force-field was developed to describe small drugs in a water-solvated environment. The strong dipole moment of water will produce a polarization effect on the charge distribution of the solute molecules. The RESP method is based upon Hartree-Fock calculations and tends to overestimate the atomic partial charges, when compared with more accurate DFT methods. However, within the original GAFF formulation this effect is not corrected in order to reproduce the water overpolarization effect. When considering other molecular liquids or other solvents,

Table 1: Comparison between calculated and experimental densities, vaporization enthalpies and viscosities for the molecules considered for development and testing of GAFF-IC. N/A means that the experimental value is not available. Regarding viscosity, NC indicates a non-converged calculation. All calculations were conducted at the temperatures reported in brackets along with corresponding experimental data, and at a pressure of 1 atm.

Molecule	Experiments			GAFF			GAFF-IC		
	ρ (g/cm^3)	ΔH_{vap} (kJ/mol)	η (mPa·s)	ρ	ΔH_{vap}	η	ρ	ΔH_{vap}	η
MIC	0.9588[191] (293.15 K)	29.9[192] (293.15 K)	N/A	1.035	44.5 ± 6.6	1.02 ± 0.11	0.956	32.4 ± 6.5	0.34 ± 0.06
EIC	0.901[191] (298.15 K)	31.8[193] (298.15 K)	N/A	0.952	48.6 ± 7.2	0.94 ± 0.16	0.915	36.4 ± 7.2	0.38 ± 0.04
BIC	0.88[191] (293.15 K)	46.8[192] (293.15 K)	N/A	0.910	66.8 ± 10.5	1.46 ± 0.27	0.889	43.1 ± 9.8	0.71 ± 0.11
ODIC	0.847[194] (293.15 K)	77.8[192] (400.0 K)	6.5 (298.15 K)	0.880	117.7 ± 32.9	NC	0.858	91.6 ± 32.1	4.3 ± 1.29
HDI	1.053[186] (293.15 K)	67.2 (293.15 K)	2.3[186] (293.15 K)	1.084	117.1 ± 14.4	21.7 ± 10.2	1.058	79.5 ± 14.5	2.83 ± 0.56
UDI	N/A	N/A	23 (296.15 K)	1.129	298.7 ± 8.9	NC	1.117	137.9 ± 21.7	26.5 ± 8.7
A3HDI	1.146 (298.15 K)	N/A	21.3 (358.15 K)	1.141	214.7 ± 27.0	NC	1.145	203.3 ± 27.6	24.0 ± 9.6
3HDI	1.146 (298.15 K)	N/A	32.1 (358.15 K)	1.145	239.4 ± 28.33	199.1 ± 23.4[10]	1.155	184.36 ± 26.9	36.9 ± 6.6
			17.8 (378.15 K)						22.9 ± 6.6
			12.3 (398.15 K)						12.6 ± 1.2

the HF-RESP charges might be inadequate.

The charge-scaling improves the agreement between calculations and experiments, however still ove-restimating the reference values, with simulations giving $\rho = 1.001 \pm 0.005$ g/cm^3 and $\Delta H_{vap} = 37.6 \pm 6.5$ kJ/mol. To test whether a stronger scaling could cure this behaviour, a factor of $\frac{1}{\sqrt{10}}$ was also considered, but very little improvement was observed with respect to the former scaling, with $\rho = 0.989 \pm 0.005$ g/cm^3 and a ΔH_{vap} of 39.9 ± 6.8 kJ/mol being obtained. This indicates that the charge scaling alone is not sufficient to achieve better accuracy, indicating that NCO-NCO interacti-ons, apart from a significant electrostatic term, also include a relevant dispersion contribution, hence the isocyanate group LJ parameters should be optimized as well.

Hence, new Lennard-Jones parameters for N, C and O atoms of the isocyanate group were obtained using the following procedure. The ε value for the three atoms was initially reduced by 0.055 kcal/mol and new parameter sets were defined incrementally considering steps of 0.005 kcal/mol. Regarding the LJ radii σ_{ij}, the default values were downsized by subtracting 0.0287 Å.

Each parameter set was used to run a calculation of ρ and ΔH_{vap} and the best results were obtained with the GAFF-IC set (see Appendix I), which provided an excellent agreement with both density and vaporization enthalpy with deviations better than 1% and 10 %, respectively. Concerning the non-bonded parameters for the alkyl group atoms, the parametrization of Dickson *et al.* was adopted [150].

Standard GAFF is known for poorly reproducing the dihedral energies of alkanes, which affects its pre-dictions of liquid phase properties. Therefore, a refitting of the relevant isocyanate dihedral energy terms is required. In any case, having changed the non-bonded parameters and the partial charge derivation scheme rendered the GAFF default dihedral parameters inconsistent.

Figure 7 shows the dihedral energy curves obtained from the optimized parameters. DFT relaxed scans were performed at the B3LYP-D3/6-311+g(d,p) level of theory. The overall accuracy increased significantly with respect to the standard GAFF, with an almost perfect match obtained for C-C-C-C dihedrals, while the C-C-C-N was greatly improved, especially the minima at ± 60 degrees.

3.2.3   Transferability and performance of GAFF-IC

The newly developed force field was further tested by calculating ρ and ΔH_{vap} of the isocyanate test set (see figure 6), as well as their viscosity at different temperatures.

Viscosity was calculated from NVE simulations through the Green-Kubo formula, as explained in section 2.4.3.5. Simulations times up to 5 ns were employed, and thermodynamic data was saved every 3 fs, for further processing. To avoid error accumulation, an integration time window t_W of 50
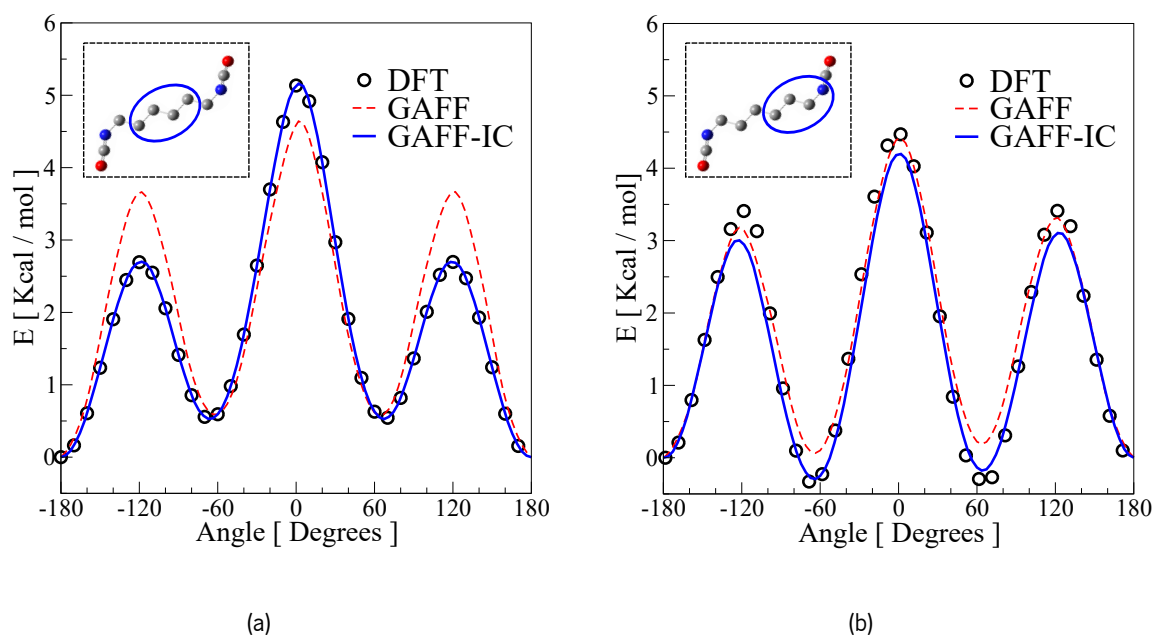
Figure 7: Comparison of dihedral energies between DFT at the B3LYP/6-311++G(d,p) level of theory (circles) and fitted molecular mechanics parameters dihedral energies (lines) for a central C-C-C-C dihedral (a) and a terminal C-C-C-N dihedral (b), as shown in insets. Mean absolute deviation is 0.2 kcal/mol.

ps was sufficient to ensure the convergence of the autocorrelation integral for the low-viscosity systems, namely all monoisocyanates and HDI. Larger t_W were considered for isocyanate dimers and trimers, up to $t_W = 600$ ps. All results were averaged considering different time origins, spaced by 15 fs. Other values were considered as well: while larger ones degrade the integral quality, smaller ones provide no improvement. For small species, up to HDI, boxes with 1000 molecules were simulated; for the larger ones and all trimers, the number was reduced to 343, in order to keep the computational cost to reasonable levels.

Table 1 lists the molecule set considered for GAFF-IC parametrization and testing, along with the experimental and calculated values for density, enthalpy of vaporization and viscosity. The calculated and experimental values of ρ and ΔH_{vap} for the molecules in table 1 are plotted in figure 8, panel (a) and (b), respectively. The densities calculated with standard GAFF are slightly overestimated, with a relative mean absolute deviation (MAD) of $2.79\,\%$ while GAFF-IC predicts densities very close to the reference ones, with a relative MAD of $0.748\,\%$. Concerning vaporization enthalpies, the use of GAFF resulted in a marked overestimation of ΔH_{vap} for all the molecules considered, producing a MAD of 55.92 %. Conversely, the GAFF-IC predicted ΔH_{vap} values are much closer to the experimental ones, with a MAD of 12.01 %. An exception seems to be represented by the HDI and ODIC, for which the GAFF-IC force field overestimates ΔH_{vap} by 17.5 % and 17.7 %, respectively. However, the reference values lie within the uncertainty of the

GAFF-IC prediction, and it clearly represents an improvement with respect to the unoptimized parameters, that overestimated the experimental ΔH_{vap} by a factor 2.
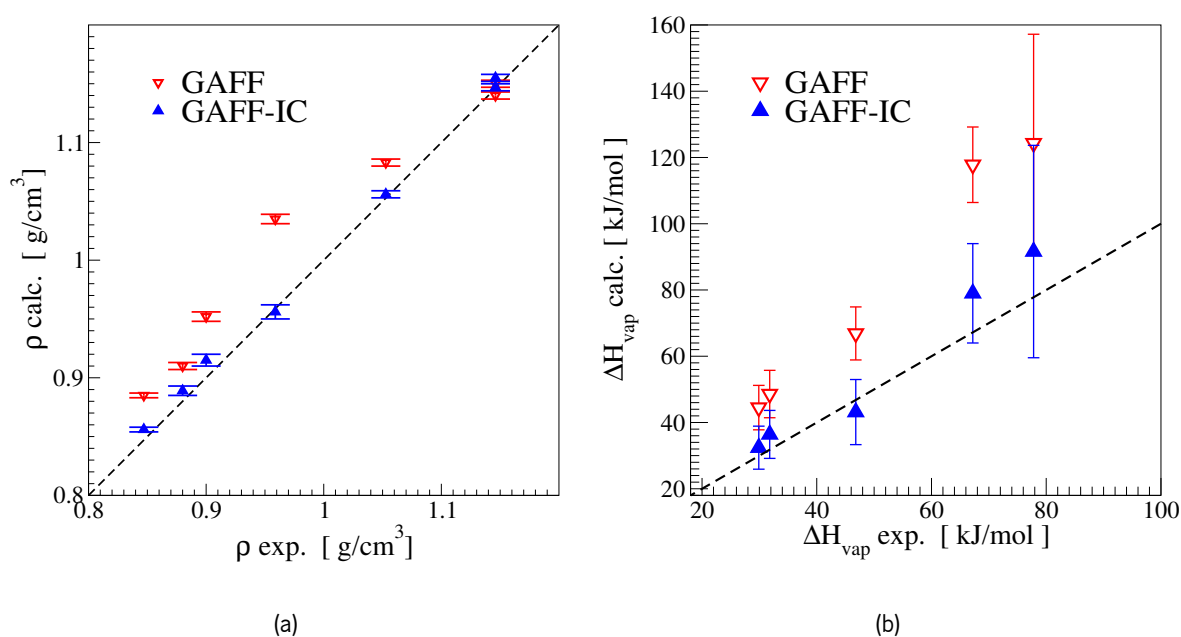
Figure 8: Deviation against experimental values of the calculated ρ (a) and ΔH_{vap} (b) for all the molecules of table 1. The plots are restricted to those molecules for which measurements were available. Dashed line is $y = x$.

Experimental and calculated viscosity values are reported in figure 9. Due to the high viscosity at room temperature of isocyanate trimers, Green-Kubo calculations can be difficult, requiring very long simulation times. Therefore, viscosity measurements for 3HDI were performed at higher temperatures, allowing for a direct comparison between experiments and simulations.

The standard GAFF force field overestimates experimental viscosities by about one order of magnitude for HDI and gives larger values for the smaller isocyanates (MIC, EIC, BIC), when compared with GAFF-IC results. In turn, GAFF-IC viscosity predictions almost match experimental values. Concerning polyisocyanates, our results show once again a large difference between the GAFF and GAFF-IC, with the unoptimized force field providing a 6-fold overestimation of the 3HDI viscosity. On the other hand, GAFF-IC provides very accurate estimates of viscosities for 3HDI and UDI, in excellent agreement with experimental values, reproducing very well the expected A3HDI/3HDI viscosity ratio. In figure 9 (b) is reported a comparison between experimental and calculated viscosities for 3HDI at three different temperatures. Again, an excellent agreement with experimental data was found, with predicted viscosities matching the experimental values.
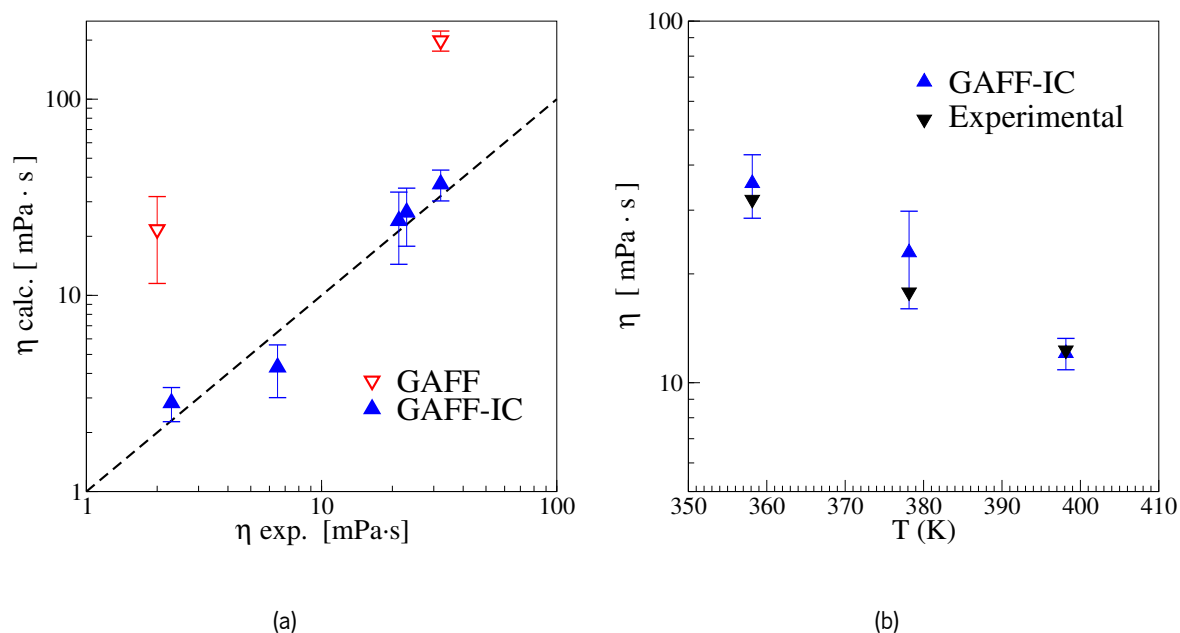
Figure 9: (a): Deviation against experimental values of the calculated η of all the molecules of table 1, and calculated at the temperatures reported therein. The plot is restricted to those molecules for which measurements were available. Dashed line is $y = x$. For 3HDI, only the first entry of table 1 is shown.

(b): Comparison between experimental and calculated viscosities for 3HDI, at different temperatures.

3.3 Viscosity calculations of selected aliphatic polyisocyanate systems

In the previous section, the validity of the GAFF-IC force field in predicting liquid properties of isocyanate and polyisocyanate liquids has been established. In the following, further results on several polyisocyanates are reported. Not only they serve as a further validation of GAFF-IC transferability and performance, but are also useful to provide insights into the physical mechanisms underneath the liquid behaviour. While the first two sections show calculations on systems for which experimental data was available, the last one shows results on not yet synthesized molecules.

3.3.1 Functional and non-functional trimers

To compare our calculations with the experimental results reported in figure 5, the series of functional and non-functional pure trimers has been reproduced. For each system, boxes containing 343 molecules were simulated. It was already pointed out that room-temperature viscosities are too high to be calculated from MD simulations. To overcome this limitation, the measurements were repeated at a higher temperature of 358.15 K, thereby allowing for a direct comparison of measured and predicted values. Unfortunately,

n=4 trimers were not available any more at the time of these measurements.
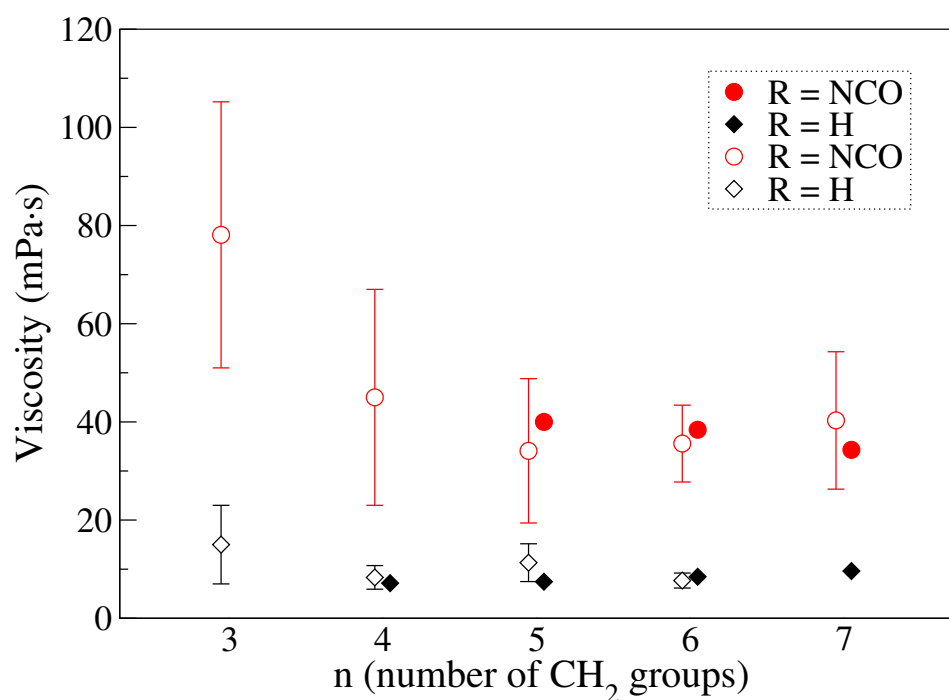
Figure 10: Comparison of simulation (open symbols) and measurements (full symbols) for a series of functional (red) and non-functional (black) aliphatic isocyanurates. All data refer to a temperature of 358.15 K and a pressure of 1 atm.

Simulation results are reported in figure 10, where compared with experimental data and an excellent agreement is found. More specifically, our model is able to capture the viscosity difference between functional and non-functional trimers. The peculiar trend of increasing viscosity for smaller molecular weights is also reproduced for functional trimers, and expanded up to the experimentally unavailable until now n=3 molecules. These results are particularly important because not only they prove that GAFF-IC can be easily and effectively transferred to isocyanate trimers, but also indicate that the current model reproduces correctly all the viscosity differences and features. meaning that it represents well the underlying physical processes.

3.3.2   Isocyanate-isocyanurate mixtures

To explain the viscosity difference between functional and non functional isocyanurates, it is possible to hypothesize the existence of some type of interaction between isocyanate groups and isocyanurate rings.

If this is true, it is expected that the mixing of HDI, bearing only NCO groups, and non-functional HDI trimers, containing only isocyanurates, would produce some observable effect in the mixture's viscosity. The viscosity of an ideal binary mixture, that is one in which the mixing process does not produce any change in volume, is described by the Arrhenius law:

$$\ln \eta_{12} = x_1 \ln \eta_1 + x_2 \ln \eta_2, \tag{3.1}$$

where the mixture viscosity η_{12} is expressed in terms of that of pure liquids η_i and the mole fractions x_i. The ideality holds when the interaction between similar or different molecules is the same, which is almost never the case [196]. To take into account non-ideality, Grunberg and Nissan [197] proposed to extend equation 3.1 by adding an empirical interaction parameter G_{12}:

$$\ln(\eta_{12}) = x_1 \ln \eta_1 + x_2 \ln \eta_2 + x_1 x_2 G_{12}. \tag{3.2}$$

A positive G_{12} is related with the onset of attractive intermolecular interactions, and would cause a positive deviation in viscosity from the Arrhenius law.

To check what happens in isocyanurate mixtures, the viscosity of $3HDI_{\nu=0}$/HDI mixtures was measured at 298 K for different mixing ratios and compared with simulations at the same conditions, as shown in figure 11.
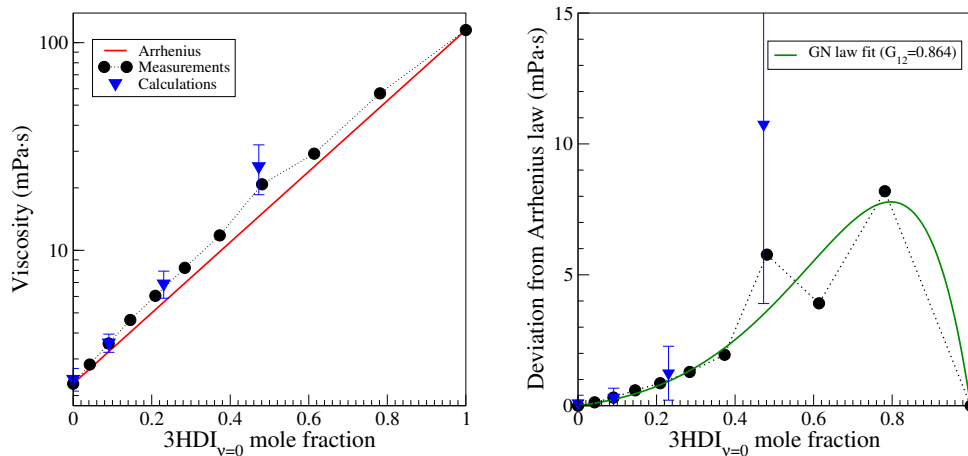
Figure 11: On the left, experimental and simulated viscosity for a HDI/$3HDI_{\nu=0}$ mixtures, measured at 298 K, reported as a function of the molar fraction of $3HDI_{\nu=0}$. The red dashed line indicates ideal behaviour, as predicted by equation 3.1.

On the right, the deviation of experimental viscosity from the Arrhenius law is reported, along with the experimental data fit using equation 3.2.

The mixture viscosity exhibits a slight positive deviation from the ideal behaviour, and can be represented well by a Grunberg-Nissan curve with $G_{12} = 0.864$. This indicates the presence of attractive intermolecular interactions between isocyanurates and isocyanates. When compared with other systems with positive deviations from ideality [198], G_{12} is rather small, suggesting that the interaction is not strong. Beside this, the simulation results follow almost exactly the experimental measurements, at least for the molar ratios simulated, proving once again the robustness of the proposed parametrization, even when applied to mixtures.

3.3.3   Effect of arm modification

Finally, we simulated a series of HDI trimer liquid with decreasing functionality, obtained by subsequently removing one of the NCO ends of the trimers. These molecules with lower functionality could be synthesized starting from mixtures of aliphatic mono- and diisocyanates, but are very difficult to isolate, therefore no experimental data is currently available. However, it is instructive to observe the change in viscosity in terms of functionality.

The temperature was set to 398.15 K to have a faster convergence of the GK calculation. Results are reported in figure 12, along with the calculated densities. While the liquid density appears to be a linear function of the functionality, $\eta(\nu)$ behaves non-linearly. It is interesting to observe that an appreciable rising in viscosity is found only from $\nu \geq 2$.

In conclusion, the last two subsections demonstrated that the viscosity of aliphatic isocyanurates does not depend in a simple way upon the presence of isocyanurate rings and isocyanate groups, but appears to be influenced by cooperative effects, as suggested by the fact that high viscosities are found only for functional trimers, where both groups are present within the same molecule, and only for $\nu \geq 2$. Mixture of diisocyanates and $\nu = 0$ isocyanurates show small positive deviations of their viscosity with respect to the ideal behaviour, indicating the presence of some kind of interaction between these molecules, expected to be weakly attractive.

To further investigate and validate these hypotheses, a deeper insight on polyisocyanates' intermolecular interactions is certainly required. How this can be obtained, by means of quantum mechanical calculations, is the subject of next chapter.
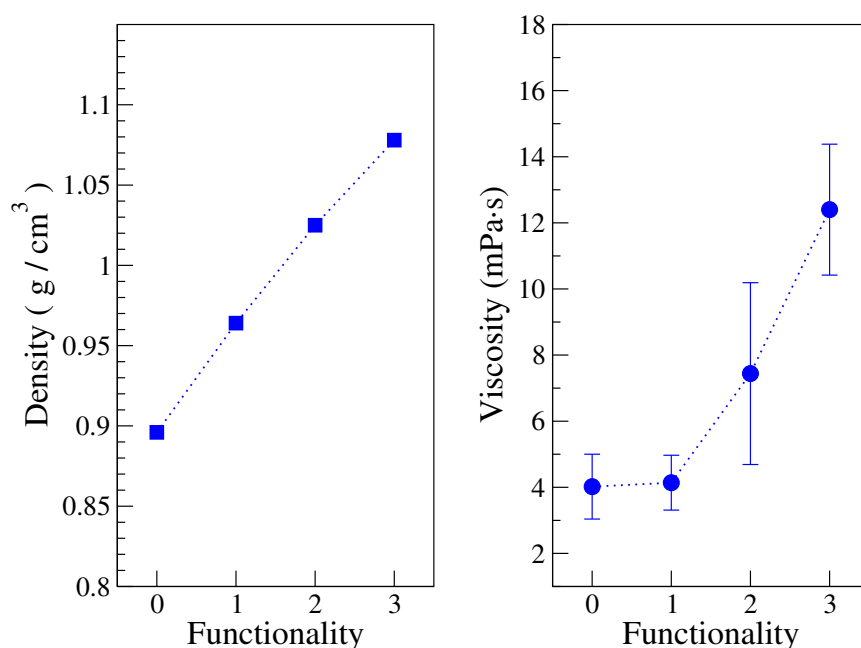
Figure 12: Calculated densities (left) and viscosities(right), at 398.15 K and 1 atm, for a series of trimers obtained from hexamethylene mono- and diisocyanates. The functionality ν represents the number of NCO terminations per molecule.

3.4   Low-temperature estimations of viscosity

One of the main limitations of the Green-Kubo method is that the liquid's typical relaxation times are getting longer as the temperature decreases, following - at first approximation- an Arrhenius-like exponential law:

$$\tau(T) \approx \tau_0 \exp^{-\frac{\alpha}{k_B T}},$$

α being an activation energy for the process under consideration. Since shear stress makes no exception, lower temperatures imply longer simulation times for the GK integral, equation 2.128, to converge. Unfortunately, requested times could exceed the limits imposed by the availability of computational resources. Moreover, even if a large number of nodes could be available, the integrals would still be prone to the inescapable accumulation of errors, undermining the reliability of results.

While higher-temperature simulations can easily overcome this limitation, corresponding experimental measurements are not always available because, in real systems, other phenomena could appear at these regimes, such as isocyanate reactions. Thus, it may be necessary to provide alternative ways to extract from simulations quantities that can be related to room temperature viscosity. In this section, we will consider the possibility to employ Stokes-Einstein and Debye-Stokes-Einstein relationships for viscosity

estimation.

3.4.1 The Stokes-Einstein and Debye-Stokes-Einstein relationships

The Stokes-Einstein (SE) relationship, derived for the motion of Brownian particles, allows to calculate the diffusivity D of a spherical particle of radius r_0 immersed in a viscous fluid with viscosity η:

$$D = \frac{k_B T}{6\pi\eta r_0}. \tag{3.3}$$

If r_0 is independent from temperature, this can be recast as:

$$\frac{\eta D}{T} \approx const. \implies \eta_2 \approx \frac{D_2 T_1}{D_1 T_2}. \tag{3.4}$$

Thus, if 3.3 is valid, then the viscosity at lower temperature T_1 can be calculated by knowing the viscosity at some higher temperature T_2 and the diffusivity coefficients at both temperatures. By stating this, it is implicitly assumed that 3.3 applies to molecular liquids. Indeed, the assumption has been found to be valid in a wide range of systems [199], although it is violated when the system approaches the glass transition temperature [200]. In atomistic simulations, it is possible to calculate the molecular mean square displacement (MSD) $\langle \Delta R^2(t) \rangle$, defined as:

$$\langle \Delta R^2(t) \rangle = \frac{1}{N} \sum_{i=1}^{N} \left| \vec{R}_i(t) - \vec{R}_i(0) \right|^2, \tag{3.5}$$

where the sum runs over all the N molecules, R_i being the position of their centre of mass. In a molecular liquid, the position of a molecule will follow a diffusive behaviour in the long time limit, $r^2 \propto Dt$. Therefore, it is possible to estimate D from 3.5, using:

$$D = \lim_{t\to\infty} \frac{\langle \Delta R^2(t) \rangle}{6t} \tag{3.6}$$

Figure13 reports the self-diffusion constants calculated for pure functional and non functional trimer liquids, at different temperatures. It is interesting to observe how, for functional trimers, the diffusivity increases with the molecular weight, while the converse seems to hold for non functional ones.

The Debye-Stokes-Einstein(DSE) relationship is the rotational analogous of 3.3:

$$\frac{\eta_1}{T_1 \tau_1} \approx const., \tag{3.7}$$

where, in lieu of the rotational diffusion constant D_r, the orientational relaxation time is used instead, by virtue of the equality $D_r = \frac{1}{2\tau_r}$. The τ_r might be extracted from the orientational autocorrelation function $C_{rot}(t)$:

$$C_{rot}(t) = \frac{1}{N} \sum_{i=1}^{N} \hat{n}_i(t) \cdot \hat{n}_i(0), \tag{3.8}$$
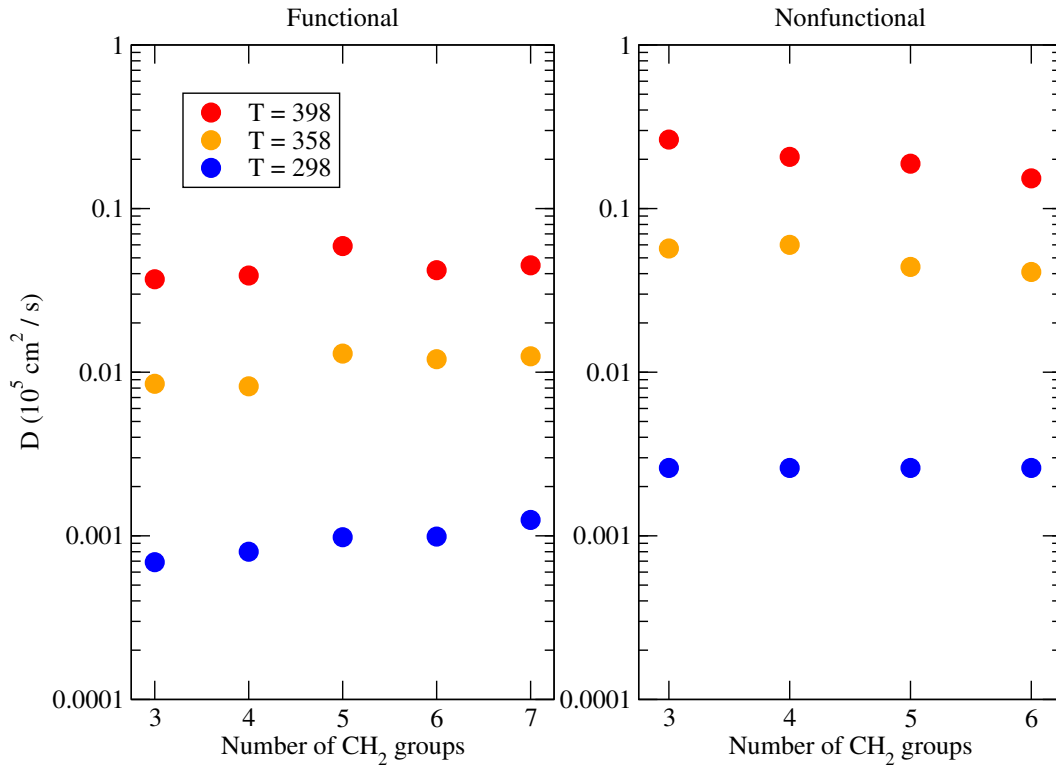
Figure 13: Self-diffusion constants for functional (left) and non functional (right) isocyanurates, for different alkyl arm lengths, at the temperature of 298, 358 and 398 K.

where N denotes the total number of molecules and the $\hat{n}_i$ are unit vectors related to the molecular orientation. For isocyanurates, a natural choice is to identify $\hat{n}_i$ with the unit vectors normal to the ring plane. The rotational relaxation could be a very slow process, exceeding by several order of magnitude the time accessible by simulations. Yet, $C_{rot}(t)$ can be fitted with a two-process stretched exponential, that is a modified Kolrausch-Watts-Williams law [201]:

$$C_{rot.}(t) = a_0 e^{-\left(\frac{t}{\tau_\beta}\right)} + (1 - a_0)e^{-\left(\frac{t}{\tau_\alpha}\right)^\gamma}, \tag{3.9}$$

and the relaxation time τ_{KWW} obtained by integrating the fitted function, where it is understood that $\tau_r = \tau_{KWW}$. Figure 14 reports the calculated τ_{KWW} for the same series of molecules as in figure 13. Rotational relaxation times grow as the temperature decreases, following an inverse trend with respect to the diffusion constants.
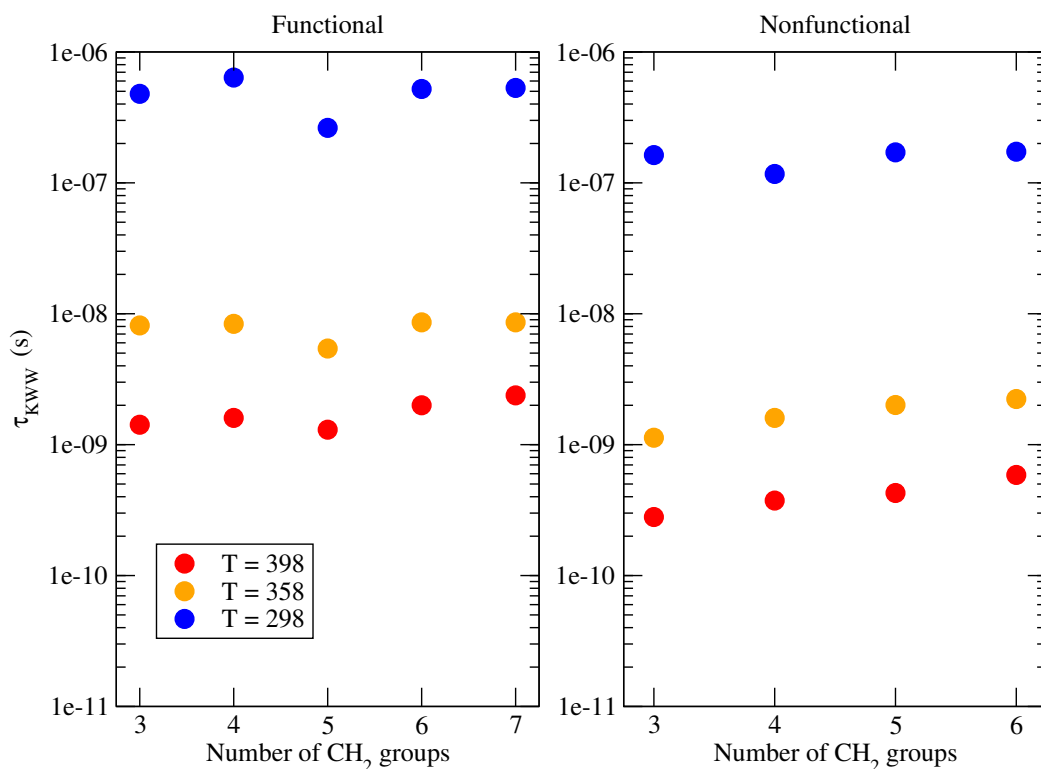
Figure 14: Rotational relaxation times for functional (left) and non functional (right) isocyanurates, for different alkyl arm lengths, at the temperature of 298, 358 and 398 K.

3.4.2 Effectiveness of diffusion-viscosity relationships

The room temperature viscosity of functional and non functional isocyanurate families estimated using 3.4 and 3.7, together with high temperature calculations reported in figure 10. The error on these estimates may be assumed to be very large, because it is composed by that coming from the high-temperature viscosity measurement and that from the D or τ_{KWW}. For these reasons, error bars are not reported, and the obtained estimates should be considered only as indicative.

DSE-based estimation exaggerates the experimental values for both families of molecules. The error is much more pronounced for non functional isocyanurates while, in the other case, the overestimation seem to improve as the alkyl arms are shorter, and their flexibility decreases. In fact, the orientational correlation function has been defined in a way that is unable to capture the effects of arm flexibility, which becomes more important as the alkyl arm length increases.The observed match with the n=4 trimer is not very relevant, because it is the only occurrence found.

69
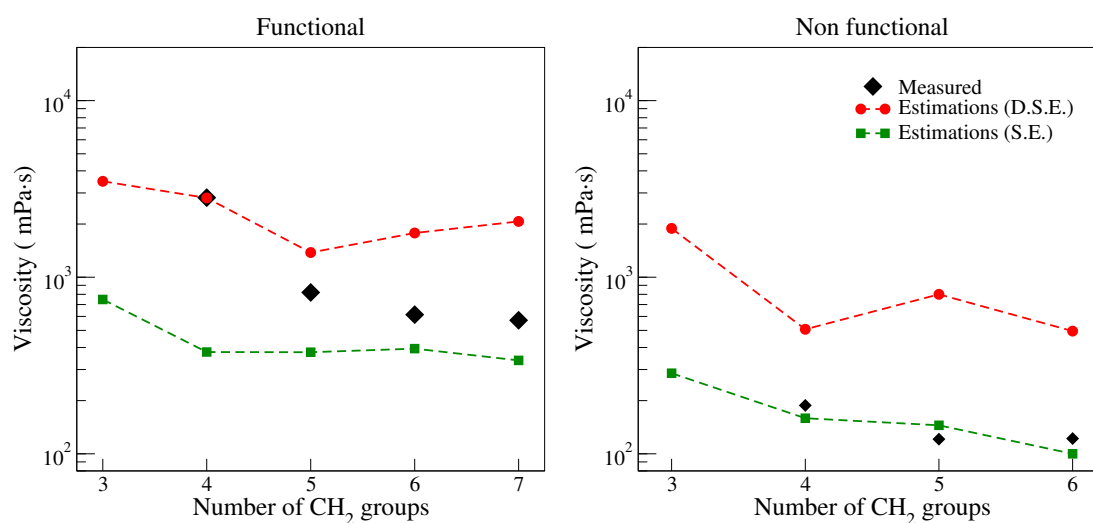
Figure 15: Estimated viscosities at 298 K for functional (left) and non functional $\nu = 0$ (right) isocyanurates, for different alkyl arm lengths, as obtained from 3.7 using either rotational or the α relaxation times. Results are compared with the experimental data at the same temperature, taken from 5.

SE-based estimates, on the other hand, appear to provide RT viscosities lower than the measured ones for functional trimers, with an error that increases the chain length decreases. Nevertheless, they provide much better values for the $\nu = 0$ trimers, with a very close agreement with experimental data. The underestimation observed in functional trimers could depend upon two factors. Firstly, it is not guaranteed that the simulation time considered is enough for those liquids to attain the diffusive regime, thus the diffusivities at 298 K might be overestimated. Since in 3.4 they appear in the denominator, larger Ds would result in lower RT viscosities. This effect is not present in non-functional isocyanurate because, due to their faster dynamics, which attain a purely diffusive regime in relatively short times.

Secondly, and this argument applies to the rotational estimates as well, there is no evidence to claim the validity of SE and DSE relationships for isocyanate liquids, and what is observed might be the result of their violation. To verify that, further experiments are required, aimed at measuring the rotational and translational diffusion of both functional and non functional isocyanurates, as well as determining their structural relaxation times.

Overall, the presented calculations seem to indicate that for aliphatic isocyanurate there is not a clear relationship between viscosity and diffusion times. Whereas some of the estimations might be certainly improved by employing more computational power, information on the validity -or violation- of SE and DSE relationships would be extremely welcome, not only to improve the understanding of the dynamics of complex molecular fluids, but also to serve as a benchmark to assess the reliability of the atomistic

models employed in simulations.

3.5 Conclusions

The GAFF-IC forcefield was developed starting from standard GAFF, and correctly predicted the densities and vaporization enthalpies of isocyanate-based molecular liquids, providing a 5-fold increase in accuracy for both quantities, when compared with GAFF. The use of GAFF-IC for viscosity calculations resulted in a striking improvement of viscosity predictions. Excellent agreement was found for HDI molecule, curing the observed order-of-magnitude overestimations of GAFF calculations. Although it was parametrized starting from monoisocyanates, GAFF-IC also proved to be transferable to polyisocyanate molecules, as testified by the broad range of molecular liquids simulated, always providing viscosities in excellent agreement with experiments as well. Our study demonstrates that GAFF-IC is a powerful tool to reliably predict densities, vaporization enthalpies and viscosities of isocyanurate materials and hence help in the design of new processing routes and materials based on isocyanates.

Different methods to estimate viscosities at ambient conditions from higher temperature calculations were also illustrated and discussed, in order to verify the possibility to expand the application field of MD simulations to common laboratory conditions. In spite of not being conclusive, some promising, yet qualitative, results were obtained, underlining the need of further investigations, not only with simulations but also from the experimental side, to clarify the validity -or violation- of Stokes-Einstein and Debye-Stokes-Einstein relationships in isocyanurate liquids, and to characterize their structural relaxation times.

We would like to stress that this parametrization, which filled an important gap, is only a first step, and could certainly be refined with future work. Directions of improvement of GAFF-IC include its extension to other family of isocyanates, such as aromatic ones, as well as a generalization to urethanes and urea, all very likely to coexist with isocyanates and isocyanurates in final materials. The compatibility with already existing parametrizations needs to be addressed, in order to pave the way for isocyanate-substrate interaction studies, interesting in their applications as coatings or adhesives, and simulation in biological environment, due to their extensive presence in biomaterials. The possibility to fully evaluate GAFF-IC performance was limited by the scarceness of quality experimental data on them. We strongly believe that further work should be performed in this sense, non only to provide a larger basis of comparison for improving the accuracy of simulations, but also to gain further insight into the microscopic dynamic properties of isocyanates and isocyanurates.

Chapter 4

Intermolecular interactions of isocyanates and isocyanurates

This chapter contains a study on intermolecular interactions of isocyanates and isocyanurates, performed through ab-initio methods and MD simulations, and is organized in two parts. The first part is an adaptation of the publication "Investigation on the intermolecular interactions in aliphatic isocyanurate liquids: revealing the importance of dispersion" [202]. The second part, containing original unpublished work, studies the noncovalent adhesion properties of isocyanurates with selected bi-dimensional materials, such as graphene, boron nitride and heptazine-based carbon nitride.

4.1   Motivation

In chapter III, a classical molecular dynamics force field has been developed, tested and applied in atomistic simulations to study the liquid state properties of aliphatic polyisocyanate liquids. The predictions followed closely experimental results for a wide range of isocyanate liquids, confirming that such approach is capable of taking into account with good accuracy their molecular-scale properties. In particular, the evidence of a weak isocyanate group/isocyanurate ring interaction has been shown, and proposed to be the basis of the high viscosities observed for functional isocyanurates. As no experimental evidence confirming or denying this is currently available, the only way to investigate this hypothesis is through *ab initio* methods.

In the following sections, the presence of such interaction is revealed with density functional theory and characterized with symmetry-adapted perturbation theory and non-covalent interaction analysis. Furthermore, gas and liquid phase binding free energies, as well as local structure properties, were obtai-

ned from classical MD simulations employing the GAFF-IC force field, demonstrating how the isocyanate-isocyanurate interaction could be connected to the higher viscosities observed in functional trimer liquids.

One interesting result is that the isocyanurate ring is capable to establish strong dispersion-dominated interactions. Considering its relatively flat structure, we investigated the adhesion properties of the ring with 2D materials, to explore the possibility of isocyanurate based non-covalent functionalization. This would have advantages over covalent approaches, because no chemical bonds are formed between the material and the isocyanurate. This results in a better preservation of the unique properties of 2D materials, and opens the possibility to embed them in an isocyanate-based networks. To explore this possibility, the adhesion energies of methyl isocyanurates were calculated for a series of 2D materials using DFT methods, and promising results are found.

4.2   Study of isocyanate and isocyanurate intermolecular interactions

4.2.1   Assessment of the accuracy of ab-initio methods for isocyanates and isocyanurates

DFT and SAPT methods were used to calculate the interaction energies (E_{int}) of isocyanate and isocyanurate dimers, as defined in section 2.1.3.2. The performance of these methods for such molecules was evaluated using high accuracy calculations as a basis of comparison. For this purpose, a test set of 16 small molecule dimers was built starting from methane, isocyanic acid (IC), methyl isocyanate (MIC) and formaldehyde molecules. An isocyanuric acid-methane dimer was also included to consider ring-based interactions. Optimized structures at the mp2/aug-cc-pVTZ level of theory were used to calculate the reference interaction energies, obtained with the CCSD(T)-complete basis set extrapolation scheme as described in [116]. An exception was the isocyanuric acid-methane dimer, for which the CCSD(T)-cbs(aDZ) [116] method was preferred due to limits in available computational power. The results obtained are shown in figure 16 and reported in table 2.

Concerning DFT methods, two hybrid DFT functional were considered, which already included a scheme for empirical dispersion correction. The B3LYP-D3BJ and the APFD hybrid functionals were compared using the 6-311++G(d,p) basis set, and showed similar performance. APFD, with a mean absolute error (MAE) of 0.16 kcal/mol, behaved slightly better than B3LYP-D3BJ, that scored a MAE of 0.20 kcal/mol. However, it showed a slight tendency to overestimate the reference E_{int} throughout the set,

Table 2:　Comparison between CCSD(T)-CBS and DFT/SAPT single point energies for the small isocyanate reference set, along with the resulting mean absolute deviations (MAD). Energies are reported in kcal/mol. DFT calculations were conducted using the 6-311++G(d,p) basis set, while SAPT calculations employed augmented (and truncated for SAPT0) correlation consistent basis sets. Last row reports the MAE of the S22 test of DFT and SAPT methods. The corresponding geometry can be found in supplementary material of [202].

Dimer	ID	Interaction energy (kcal/mol)					
		CBS	B3LYP-D3BJ	APFD	SAPT0	SAPT2 -dz	SAPT2+ -dz
IC dimer (linear)	B1	-3.64	-3.74	-3.54	-4.03	-3.31	-3.26
IC dimer (L-shape)	B2	-4.06	-4.42	-4.32	-4.42	-4.08	-3.84
IC dimer (symmetric)	B3	-3.83	-3.88	-4.14	-4.60	-3.69	-3.52
IC and CH_2O	B4	-4.86	-5.02	-5.33	-5.77	-4.71	-4.60
ICU and CH_4 (top)	B5	-2.35[1]	-2.26	-2.53	-1.41	n/a	-2.28
MIC dimer (cc)	B6	-6.17	-5.81	-6.23	-6.37	-5.99	-5.89
MIC dimer (ct)	B7	-5.94	-5.50	-5.97	-6.09	-5.85	-5.73
MIC dimer (tt)	B8	-5.70	-5.17	-5.69	-5.79	-5.69	-5.55
MIC and CH_4 (linear)	B9	-0.64	-0.44	-0.49	-0.43	-0.58	-0.61
MIC and CH_4 (bridge)	B10	-1.52	-1.37	-1.47	-0.63	-1.51	-1.34
MIC and CH_4 (tail)	B11	-0.85	-0.73	-0.81	-0.43	-0.77	-0.74
MIC and CH_4 (nitrogen)	B12	-1.12	-1.02	-1.11	-0.59	-1.14	-1.02
MIC and CH_2O (c)	B13	-5.32	-5.22	-5.58	-5.91	-5.13	-5.03
MIC and CH_2O (t)	B14	-5.08	-4.89	-5.31	-5.73	-4.96	-4.85
IC and MIC	B15	-5.09	-5.00	-5.29	-5.04	-5.00	-4.87
MIC dimer (NH:NH)	B16	-2.79	-2.98	-3.03	-2.61	-2.95	-2.80
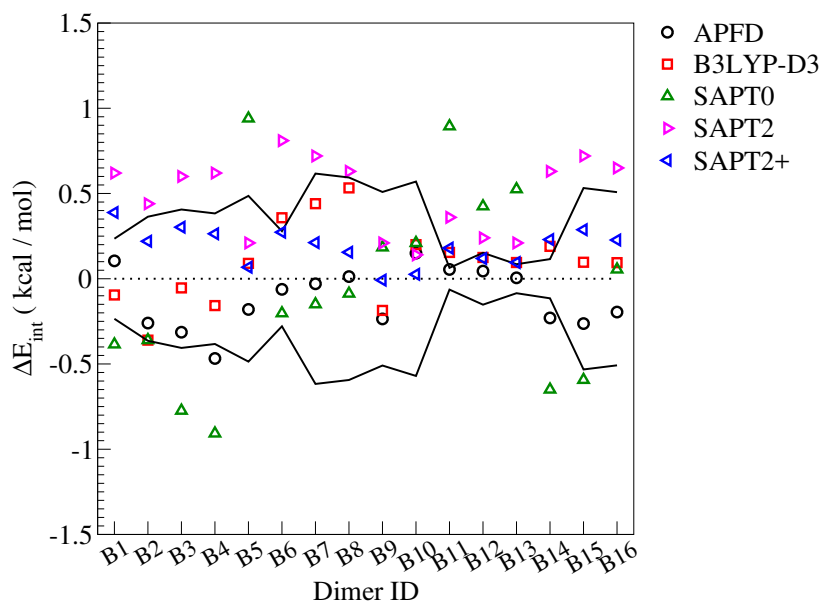
Figure 16: Difference between the reference CCSD(T)/CBS energy and the results of the various methods tested, for the isocyanate test set. Solid lines denote 10 % accuracy w.r.t. the reference energies.

particularly evident for the ICU-CH4 dimer. To further compare these methods, the S22 [116, 203] benchmark was used, revealing that B3LYP-D3BJ/6-311++G(d,p), with a MAE of 0.25 kcal/mol, represents an overall better choice, while APFD/6-311++G(d,p), with a MAE of 0.86 kcal/mol, greatly overestimated the interaction energy of both dispersion-dominated and strong H-bound complexes.

For perturbative methods, a comparison on the isocyanate test set has been performed between the SAPT0/jun-cc-pvdz, SAPT2/aug-cc-pVDZ and SAPT2+/aug-cc-pVDZ, the last of which was suggested as a possible reference method for medium-size problems [114]. Higher order SAPT methods were precluded due to the size of the studied systems. It was found that SAPT0/jun-cc-pVDZ and SAPT2/aug-cc-pVDZ provide a similar, poor, accuracy. In particular, SAPT2 method systematically underestimates the interaction energies. In turn, SAPT2+ method provided much better results, with a MAE of 0.20 kcal/mol on the isocyanate set and of 0.34 kcal/mol for the S22 benchmark [114], making it the best available choice for SAPT calculations in this context.

4.2.2   Interaction energies of model bimolecular complexes

Isocyanurates interactions could be decomposed as the sum of independent contributions, that is NCO-NCO (NN), NCO-isocyanurate ring (NR) and ring-ring (RR) contacts. Considering dimers of simple molecules, these interactions can be isolated, getting rid of the conformational complexity of larger systems,

and their E_{int} readily calculated. The molecules considered were methyl isocyanate (MIC), ethyl isocyanate (EIC) and ethylene diisocyanate (EDI), propyl isocyanate (PIC) and propylene diisocyanate (GDI), hexyl isocyanate (HIC) and hexamethylene diisocyanate (HDI), trimethyl symmetric (3MIC) and asymmetric (A3MIC) trimer, triethyl isocyanurate (3EIC) and propylene diisocyanate trimer (3GDI). A graphical representation of all dimers considered is drawn in figure 17, while their E_{int} calculated by DFT and SAPT methods are reported in table 3 and figure 18.

Table 3: Interaction energies (in kcal/mol) of model dimers, calculated at the B3LYP-D3BJ level of theory and using SAPT2/SAPT2+ methods.

Dimer	ID	Contact type	E_{DFT} (kcal/mol)	E_{SAPT2} (kcal/mol)	E_{SAPT2+} (kcal/mol)
MIC-MIC	1	NCO-NCO	-5.81	-5.36	-5.89
EIC-EIC	2		-6.06	-5.97	-6.47
EDI-EDI	3		-6.68	-6.60	-7.17
PIC-PIC	4		-6.26	-6.27	-6.78
PIC-GDI	5		-7.18	-7.08	-7.61
GDI-GDI	6		-7.85	-7.66	-8.21
HIC-HIC	7		-6.37	-6.44	-6.98
HIC-HDI	8		-6.68	-5.41	-5.84
HDI-HDI	9		-6.92	-6.86	-7.45
3MIC-MIC	10	NCO-Ring	-7.08	-7.07	-7.55
3MIC-EIC	11		-7.38	-7.62	-8.11
3MIC-PIC	12		-7.71	-7.96	-8.46
3EIC-EIC	13		-7.02	-7.33	-7.91
3GDI-3GDI	14		-13.49	n/a	n/a
3GDI-3GDI	15		-17.58	n/a	n/a
3MIC-3MIC	16	Ring-Ring	-13.75	-13.28	-14.18
A3MIC-A3MIC (a)	17		-11.64	-12.54	-13.13
A3MIC-A3MIC (b)	18		-12.36	-13.06	-13.60
A3MIC-3MIC	19		-13.16	-13.65	-14.40
3EIC-3EIC (a)	20		-12.13	-12.74	-13.72
3EIC-3EIC (b)	21		-13.08	-14.51	-15.31
3EIC-3EIC (c)	22		-10.02	-10.06	-10.84

NCO-NCO bound dimers

1   2   3   4

5   6   7

8   9

NCO-Ring bound dimers

10   11   12   13

14   15

Ring-Ring bound dimers

16   17   18   19

20   21   22
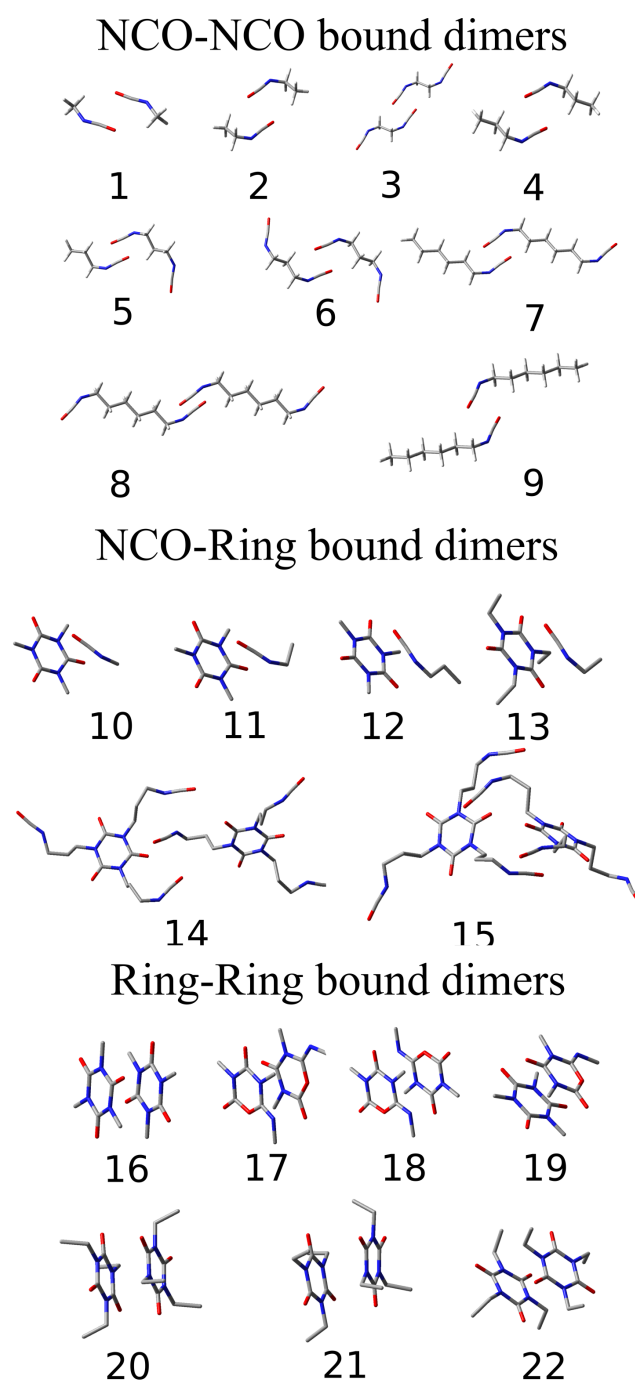
Figure 17:   Representation of the isocyanate dimer geometries used to calculate the interaction energies reported in table 3. For NCO-Ring and Ring-Ring dimers, hydrogen are not shown.
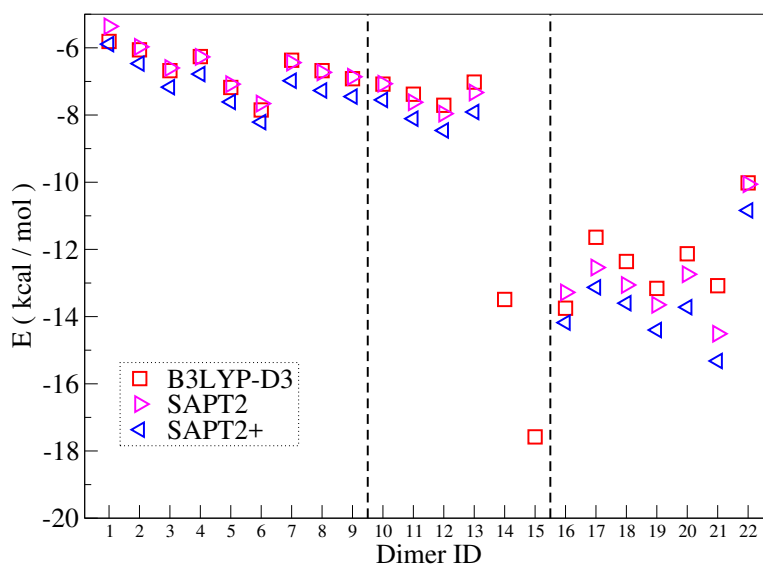
Figure 18: Interaction energy for the dimers of table 3. The plot is subdivided by interaction type in NCO-NCO (NN) dimers, NCO-ring (NR) dimers and ring-ring(RR) dimers. Dimer IDs are the same as in table 3.

The first group, which contains dimers involved in NN contacts, has the weakest E_{int}. The interaction energy seems to be weakly dependent on the alkyl chain length, while being influenced by the presence of NCO groups not directly involved in the contact, undergoing long-range electrostatic interactions. These effects are stronger for shorter molecules, in which the peripheral NCO groups are generally closer.

NR interactions, in the second group of table 3, are a specific feature of systems containing both isocyanurate rings and isocyanate groups. For all the systems investigated, the geometrical optimization always led to a structure similar to that reported in figure 22: the NCO carbon adopts a bridge position with respect to the underlying ring N-C bond, whereas the NCO oxygen places itself approximately along the ring axis. Their interaction energy is of the same order of magnitude as NN contacts.

The strongest binding can be achieved with RR-type interactions, with E_{int} always lower than -10 kcal/mol. The lowest interaction energies were obtained with a perfectly parallel stacking of the two molecules along the axis that passes through their ring centres, with a relative rotation of $\pi/6$. This conformation is invariant under $\pi/3$ rotations of one of the molecules around its axis. Longer alkyl chains extent always normally to the ring plane(i.e. either up or down), leading to several possible stable minima, all of which showed comparable energies.

A3MIC dimers provided slightly weaker E_{int} than 3MIC dimers. The presence of two minima in table 3 is due to the fact that the asymmetric ring dimer breaks the rotational symmetry and allows for two

parallel stacked stable conformations, with different rotation angles.

Comparing DFT and SAPT results, it is evident that SAPT2/SAPT2+ energies are always lower than B3LYP ones, especially for RR-type interactions. Yet trends are in excellent agreement everywhere, except for the RR-type interaction branch, in which DFT indicates the 3MIC/3MIC dimer as the lowest energy one, in contrast with SAPT calculations. This discrepancy could be related to the difference in treatment of dispersion between these methods and higher level of theory calculations would be required to establish which predictions are more accurate.

Finally, to get an insight into the expected order of magnitude of the E_{int} of larger molecules, the interaction energy of two stable conformations exhibiting NCO-ring interactions (see figure 19) of 3GDI isocyanurates was calculated. This revealed a relatively strong E_{int}, probably arising from the cooperation effect of different contributions, in which NR type interactions could play a crucial role. To verify this assumption, the most energetic 3GDI dimer was modified by sequentially replacing the NCO groups by a hydrogen atom, whose position was relaxed while keeping all other atoms fixed. In figure 19, along with the starting dimer representation, the resulting E_{int} are reported.
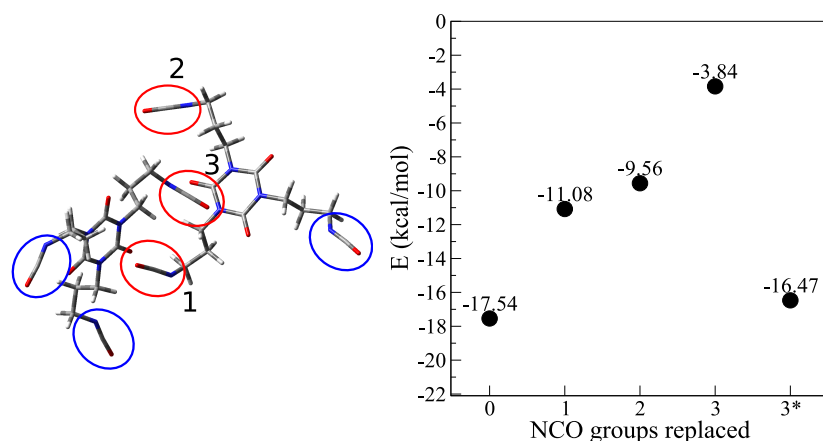
Figure 19: Interaction energy of a stable 3GDI dimer as a function of replacement of NCO groups involved in the bimolecular contact. In the left, a representation of the 3GDI dimer is shown, along with the substituted NCO groups (red circles). Related numbers indicate the replacement order. The 3^* point represents the 3GDI dimer with all the peripheral NCO groups (blue circles) substituted.

The substitution of NCO groups labelled 1 and 3 increases the initial E_{int} by 6.86 and 5.72 kcal/mol, respectively. In contrast, the removal of the NCO group labelled 2 accounts for an increase in E_{int} of 1.52 kcal/mol only. NCO groups 1 and 3 could then be identified as involved in NR contacts, accounting for 71.5 % of E_{int}. This also proves the consistency of the interaction decomposition scheme proposed, as the residual contribution of the aliphatic chains and methane groups is small. Interestingly, if the distant

NCO groups are substituted, only a small increase of E_{int} of 1 kcal/mol can be observed, indicating that these groups bring a marginal contribution, likely only due to long-range electrostatic forces.

The data presented so far reveals that the isocyanurate ring, in both of its symmetric and asymmetric variants, is a strong noncovalent interaction site. In particular, it has been shown how it is capable of forming a perfectly stacked structure with a strong interaction energy, and to bind in a peculiar way with NCO groups. In fact, the NR contact seems to be the key mechanism to cooperatively build strong interaction energies between functional isocyanurate molecules. This assumption agrees with the simulations reported in section 3.3.3, in which, by simulating pure n=6 3HDI liquid with different functionalities, a sensible viscosity change was observed only for $\nu \geq 2$.

4.2.2.1   SAPT energy decomposition and NCI analysis

The use of SAPT methods naturally provided a decomposition of the dimers interaction energy in terms of a clear physical meaning, allowing for a precise analysis of the nature of the different contacts. The decomposition of the attractive part of E_{int}^{SAPT} for the studied dimers is reported in figure 20.
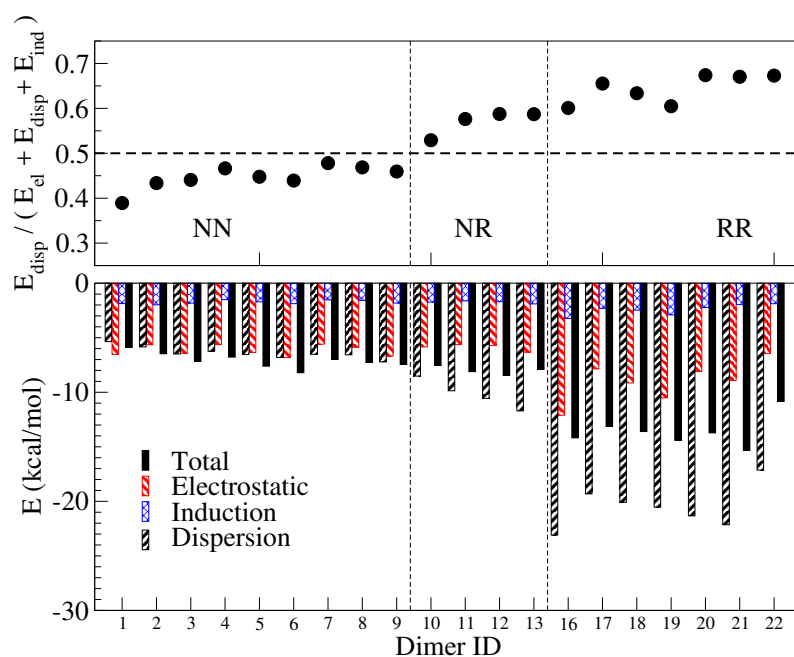
Figure 20: bottom: Total E_{int}^{SAPT} (black bar) and its attractive contributions, for the dimers of table 3, calculated using the SAPT2+/aug-cc-pVDZ method. 3GDI trimers, too large for SAPT2+ calculations, are not reported. The plot follows the same subdivision in NCO-NCO (NN), NCO-ring (NR) and ring-ring dimers (RR) as figure 18.

Top: ratio between the dispersion contribution and the attractive part of E_{int}^{SAPT} for each dimer.

The SAPT energy decomposition revealed a net differentiation between NN contacts and the other

types, with dispersion and electrostatic energies contributing almost equally to E_{int}^{SAPT}. Conversely, the dispersion energy accounts for 60-70 % of the attractive part of E_{int}^{SAPT} in NR contacts and, by a greater extent, in RR contacts. These calculations indicate that the interactions involving an isocyanurate ring are essentially similar, with the same prevalence of dispersion forces. The induction term provides a small contribution, being more relevant for NN and NR dimers, for which it accounts for 10-12 % of the total attractive contribution.

Furthermore, an NCI analysis was performed on three model dimers, each representative of a contact type, to investigate the extension of the contact area and to gain further information on the nature of their interactions.
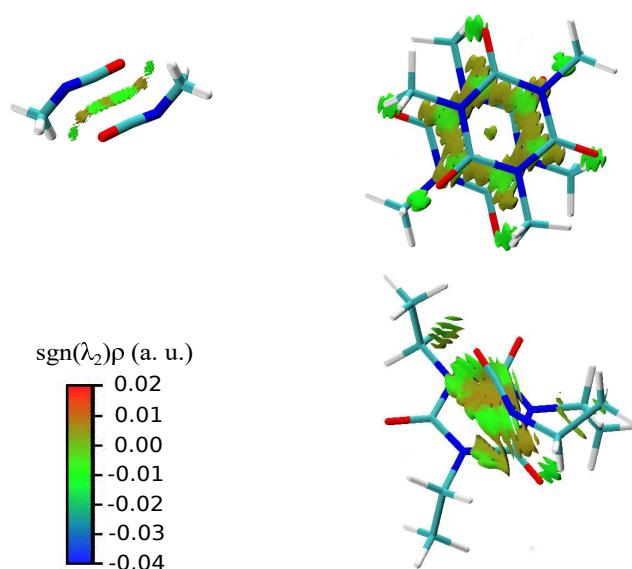
Figure 21: Reduced density gradient s isosurfaces (s=0.4) of methyl isocyanate dimer (top left), trimethyl isocyanurate stacked dimer (top right) and ethyl isocyanate-triethyl isocyanate dimer (bottom). The isosurfaces are coloured according to $\mathrm{sgn}(\lambda_2)\rho$ [128]. Intramolecular isosurfaces were omitted for clarity.

As it can be seen in figure 21, delocalized interactions are present, as expected for weak noncovalent interactions [128]. This is true in particular for NR and RR contacts, in which the interaction region is widespread and covers almost the entire isocyanurate ring. This indicates that the interactions involve a large area of the electron density above it, due to the π orbitals normal to the ring plane from $sp2$ hybridized atoms. The NCI analysis suggests that ring-based dispersion forces are mostly caused by $\pi \cdots \pi$ interactions involving the π orbitals of an isocyanurate ring interacting with, for example, those of a neighbouring isocyanate group or a second isocyanurate ring. The strong dispersion forces observed for the isocyanurate rings also suggest a possible use as an alternative for non-covalent functionalization

of two-dimensional materials.

There results are fully compatible with those presented in Chapter III, where the existence of weak NR contacts was introduced and justified by the positive deviation from ideal behaviour in the viscosity of isocyanates and non functional isocyanurates. Their dispersion-dominated nature also relates the with lack of experimental data.

4.2.3   Local structure properties of isocyanate/isocyanurate liquids

4.2.3.1   Free energy calculations in gas and liquid phase

In previous sections, it was demonstrated that the different contact types between isocyanurates possess distinctive aspects. In particular, NR contacts showed very interesting features, such as a collaborative character. The objective of the next section is to investigate the liquid state of isocyanate/isocyanurate systems to understand not only the way these molecules locally organize, but also the presence and stability of the discussed interactions and how they influence the local structure.

The free energy of binding ΔG_b provides information on the stability of a given dimer at non zero temperature, and it was thus calculated, in gas and liquid phase, for the different contacts. The adaptive biasing force (ABF) method was used to obtain the potential of mean force (PMF) as a function of a properly defined collective variable. Specifically, the distance between ring and NCO group geometric centres was employed. The gas and liquid phase simulations were performed under NVE conditions. The liquid phase was simulated using a pure MIC as a solvent. This simplification, both in solution and in the dimers involved, is necessary in order to obtain converged curves in reasonable times, since more complex molecules would have required much longer simulations, because of their conformational complexity. Table 4 reports the $\Delta G_b^{gas,liq}$ for 3MIC/MIC possible dimers, along with the shortest distance of approach, corresponding to the global PMF minimum.

In the gas phase there is only one free energy minimum that corresponds to the most stable structure. Interestingly, the MIC-3MIC dimer has a ΔG_b^{gas} that is twice than that of the MIC-MIC dimer, while the DFT-calculated interaction energies were equal. The strength of ring-ring interactions is confirmed here by the strong ΔG_b^{gas} of 3MIC-3MIC dimer. Thus, the different interactions can be clearly ordered by ΔG_b^{gas}. Concerning liquid phase calculations, the obtained PMF curves are reported in figure 22, showing a slightly different behaviour. The 3MIC-3MIC PMF curve exhibits several stable minima, with the closest (CM) being also the strongest, with a ΔG_b^{liq} of -0.81 kcal/mol, and corresponding to the parallel stacking conformation. In addition, there are two solvent separated minima at 5.4 and 8.2 Å, with a ΔG_b^{liq} of
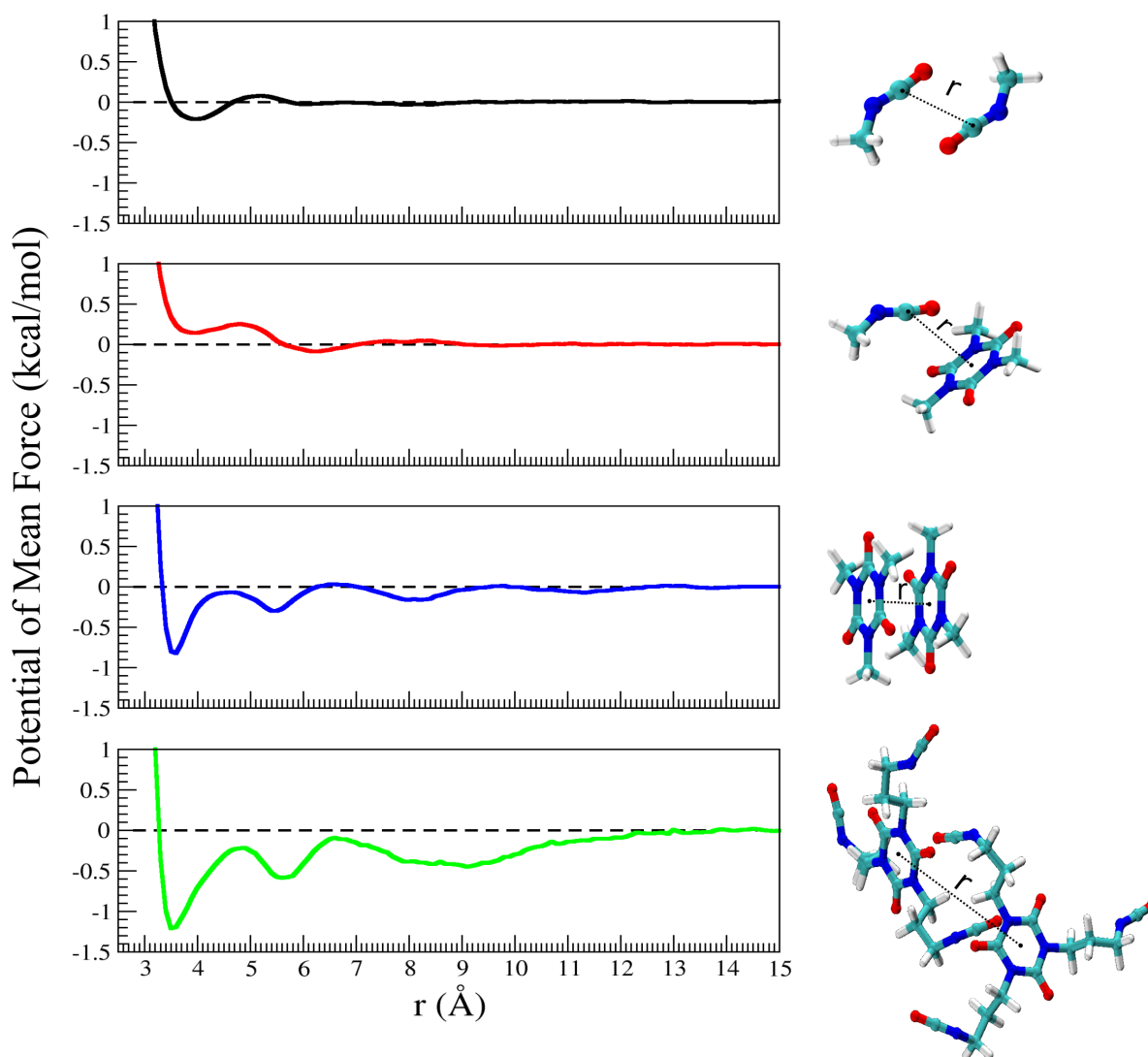
Figure 22: PMF curves obtained at 298.15 K and 1 atm, in a pure MIC liquid solution, for different possible contact types, exemplified by MIC-MIC (black), MIC-3MIC (red), 3MIC-3MIC (blue) and 3GDI-3GDI (green) dimers. On the right side of each plot, a representation of the molecules and respective collective variable is shown.

Table 4: Free energies of binding of 3MIC and MIC dimers in the gas and liquid phase. Minimum distances refer to the gas phase. The zero value was set as the value of G_b at 14 Å. The depth of the liquid MIC-3MIC minimum was measured on the metastable minimum at 3.9 Å.

Molecules	r_{min} (Å)	ΔG_b^{gas} (kcal/mol)	ΔG_b^{liq} (kcal/mol)
MIC-MIC	3.9	-0.94	-0.18
MIC-3MIC	3.9	-2.22	$-0.10*$
3MIC-3MIC	3.5	-6.02	-0.81

-0.22 and -0.18 kcal/mol, respectively. In the case of the MIC-MIC dimer, a relatively shallow PMF curve was found, with one weak minimum at 3.8 Å. The MIC-3MIC PMF curve, conversely, is more structured, showing one metastable minimum at 3.9 Å and another around 6 Å. It is interesting to observe how the more complex 3GDI-3GDI dimer produces a richer PMF, with a large and shallow minimum located at large ring-ring distances, centred around 9 Å, and probably caused by NR and NN contacts, although in this case a simple interpretation of the PMF curve in terms of elementary interactions is not obvious.

RR contacts are dominant in liquid systems, due to their stronger ΔG_b^{liq}, and the longer range, producing appreciable effects up to 12 Å. Concerning the other contacts types, the NN PMF has a clear minimum, however the NR curve is not trivial, confirming that both could play a significant role in the liquid phase, as also suggested by the 3GDI-3GDI PMF.

4.2.3.2   Local structure characterization

MD simulations of isocyanurate liquids were performed under NVE conditions, using the GAFF-IC force field, considering different alkyl chain lengths containing $n = 3-6$ CH_2 groups. Non functional aliphatic isocyanurates were also included to study systems capable of RR contacts only. For each molecule, the ring geometric centre is the most convenient choice as reference point, and it was used to calculate the intermolecular ring-ring pair correlation function $g(r)$ on systems equilibrated at 298 K and 1 atm (figure 23). Furthermore, the $g(r)$ was decomposed by calculating, for each molecular pair, their relative tilt angle, that is the scalar product of their ring normal unit vectors, $\hat{n}$, according to

$$\theta_{ij} = \cos^{-1}(\hat{n}_i \cdot \hat{n}_j)$$

in order to get the relative tilt angle distribution $g(r, \theta)$ (figure 24).

The ring-ring $g(r)$ shows several important features. Closest neighbours are located approximately at 3.5 Å, followed by a major peak around 6 Å, more pronounced for non functional molecules. A third,
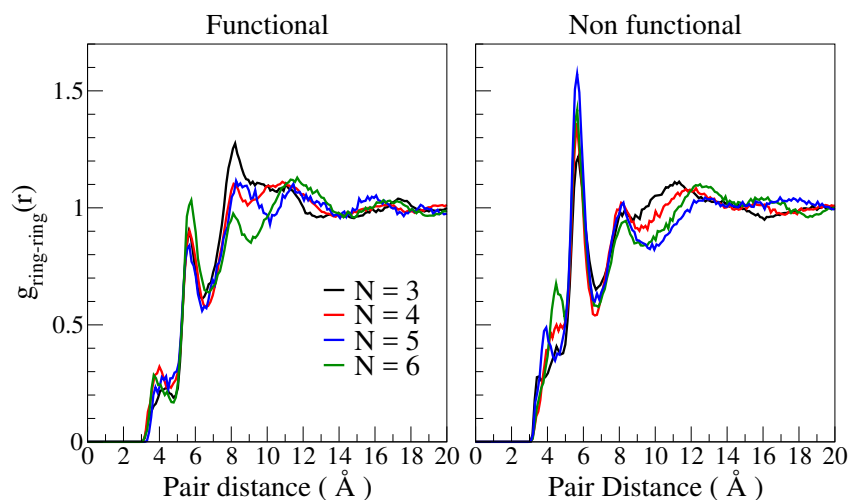
Figure 23: Intermolecular ring-ring $g(r)$ for functional and non functional isocyanate trimers, as a function of the ring-ring distance r. N denotes the number of $-(CH_2)-$ in the alkyl chains.

smaller, peak can be identified at 8 Å, the height of which strongly depends on the alkyl chain length for functional trimers, while it is almost unchanged for non functional ones. In the region above 10 Å, a weak modulation of the g(r) around unity can be observed for both families. Regarding the $g(r,\theta)$, closest neighbours appear to stack, with a net majority of small angles. For the second peak, relative tilt angles are higher, indicating an abundance of tilted rings, that is in a "T" conformation. At larger distances, it is impossible to extract useful information, as angular isotropy is recovered.

The analysis of $g(r)$ and $g(r,\theta)$ showed that RR interactions define the liquid microscopic structure, as already indicated by PMF calculations. Indeed, the $g(r)$ peaks and the PMF minima for the RR contacts correspond and their position is independent of either alkyl chain length or presence of NCO groups. Additionally, $g(r,\theta)$ showed that close rings prefers a parallel arrangement. Thus it is expected that, in this region, RR contacts constitute the main intermolecular contact type. It is important to note that non functional molecules display larger $g(r)$ at short distances, when compared to their functional counterparts. This indicates that, for the latter, RR-type interactions are partly screened. Based on the results presented in previous sections, this can be explained by the presence of NR contacts.

4.2.4   Characterization of NR contacts

As already mentioned, non functional isocyanurates, at parity of conditions (alkyl chain length, temperature, pressure), typically exhibit viscosities that are 3-5 times lower compared to functional ones. This difference was already attributed in chapter III to the NR-type interactions, which were deeply investigated
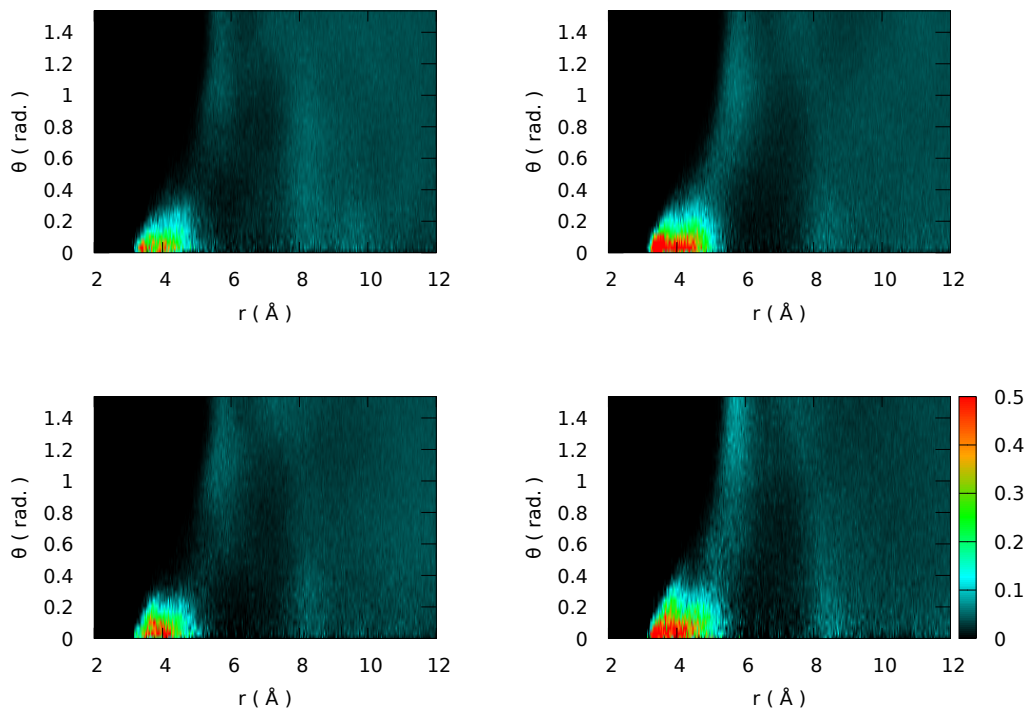
Figure 24: $g(r,\theta)$ as a function of the ring-ring pair distance for functional (left) and non functional (right) isocyanurates, calculated for trimers with N=3 (top) and N=6 (bottom) carbons in the alkyl chains.

in the preceding sections. Based on the low viscosity of linear diisocyanates, NN contacts are not expected to play a significant role. Therefore, the characterization of NR-type interactions in the liquid isocyanurates will help to verify the consistency of this hypothesis. In this regard, the distance r_c between rings and -NCO group centres, belonging to different molecules, was measured for each possible pair and an NR contact was acknowledged if $r_c < 4.0$ Å. In figure 25 the radial NR contact density $n_c(r)$ is reported as a function of the intermolecular ring distance, normalized in such a way that

$$N_{NR} = \int_0^\infty 4\pi r^2 \mathrm{d}r n_c(r)$$

is the number of contact points per molecule.

It can be observed that the NR contact density is greatly influenced by the alkyl chain length, in such a way that the maximum of the distribution decreases and the width increases, for increasing alkyl chain length. The only constant feature is the small peak at 6 Å, corresponding to the first $g(r)$ peak. The other peak at 8.2 Å, corresponding to the second $g(r)$ peak, is clearly visible for the lighter molecules, up to N=5, but then disappears for N=6, which displays a different contact distribution, more skewed towards larger distances. The difference could be due to the fact that, for short alkyl chains, terminal isocyanates are constrained in their movements while, in the opposite case, the space they can explore is much larger,
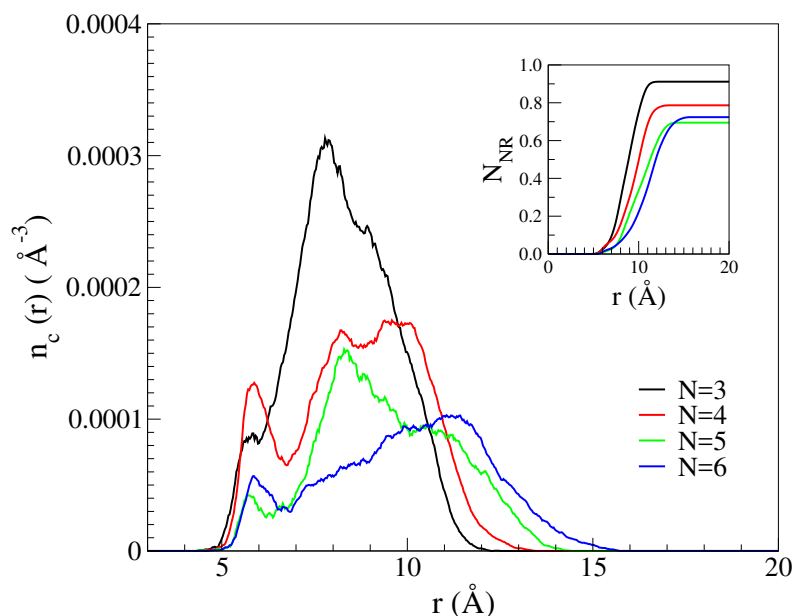
Figure 25: Distribution $n_c(r)$ of NR contacts per molecule and per unit volume of functional isocyanurates as a function of the intermolecular ring-ring distance r, at 298.15 K and 1 atm. N denotes the number of $-(CH_2)-$ in the alkyl chains.

Inset: integral of $n_c(r)$, yielding the number N_{NR} of NR contacts per molecule.

hence a broader distribution of chain lengths is expected. At the same time, the probability of NR contacts at shorter distances is reduced, due to excluded volume effects.

The smallest system has $N_{NR} = 0.9$ NR contacts per molecule, meaning that ca 90 % of the molecules are bound in this way. N_{NR} seems to be proportional to the alkyl chain length, although there is a net change from N=5 to N=6, caused by the different character of their $n_c(r)$. It can be observed that N_{NR} correlates with the experimental viscosity trends of functional isocyanurates reported in chapter III, with higher values corresponding to higher viscosities.

In the range of short ring-ring distances, the NR contacts are absent and the interactions are dominated by the RR contacts, as already indicated by $g(r)$ and $g(r, \theta)$. However, at longer ranges, the RR contribution drops significantly, as dispersion forces decay more rapidly than dipole-dipole or any electrostatic interaction, and NR contacts provide the strongest intermolecular interaction energies. To prove this, a liquid phase simulation snapshot from the 3GDI liquid was analysed and, by using the ring-ring distance as radial variable, the DFT interaction energy of all pairs at a fixed distance, within a bin 0.1 Å wide, was calculated. Because of the large number of calculations on large systems (90 atoms), the basis set was reduced to 6-31+G(d,p). The results, divided according to the presence or absence of NR contacts, are

Table 5: Averaged DFT interaction energies of all intermolecular pairs at the indicated ring-ring distance, for a 3GDI liquid at 298.15 K and 1 atm. In each bin, the pairs were divided in two complementary sets, according to the presence or absence of NR contacts.

Distance (Å)	NR pairs	$\langle E_{int} \rangle$ (kcal/mol)	no NR pairs	$\langle E_{int} \rangle$ (kcal/mol)
6.65 ± 0.05	5	-10.7 ± 4.0	10	-6.0 ± 1.6
7.65 ± 0.05	13	-11.0 ± 2.5	34	-5.9 ± 2.2
8.65 ± 0.05	14	-8.8 ± 2.6	49	-4.7 ± 1.8

collected in table 5. Although they occur less frequently, in each bin, NR-bound pairs on average have a stronger E_{int} than non-NR bound pairs, roughly by a factor 2. This proves that the presence of NR contacts helps to strengthen the cohesive forces in the liquid, because they add a significant contribution to the intermolecular interaction energies.

4.3   Non-covalent interactions of isocyanurate rings with 2D materials

In previous sections it was highlighted the strong dispersion character of the interactions with isocyanurate rings. This makes them attractive candidates for non-covalent functionalization agents of 2D materials, since their interaction does not involve the formation of new bonds, and thus preserves the functionalized surface and, by consequence, its properties. This possibility would make 2D materials easily embeddable into a crosslinked PU matrix, enabling the crafting of functional and smart polyurethanes.

Graphene [204], certainly the most important 2D material due to its very peculiar properties and its great range of applications, was chosen as model system to test the non-covalent functionalization capabilities of isocyanurates. Other 2D materials, namely fluorinated graphene(FC), boron nitride (BN) and heptazine-based carbon nitride(CN) were also tested, due to their interesting properties. FC is a transparent insulator [205] that could be processed to provide magnetic properties [206]. Boron nitride is an insulator with excellent mechanical and thermal conduction properties [207] and heptazine-based CN[2] is renown for its strong piezoelectric behaviour [208] and for its role as a photocatalyst for water dissociation [209, 210].

---

[2]In the following, heptazine-based is the only type of CN considered, thus we will refer to it simply as CN.

4.3.1   Isocyanurate-graphene adhesion properties

To obtain the adsorption energy between graphene and another molecule, a non-periodic approach is possible, in which the substrate is substituted by polycyclic aromatic hydrocarbons(PAH), which size is progressively increased. In figure 26 is reported the so-calculated E_{ad} of a triethyl isocyanurate on graphene, at the B3LYP-D3BJ/6311++g(d,p) level of theory. It is evident that this non-periodic approach is prone to large size effects. The asymptotic value represents the interaction between the adsorbate and an infinite graphene sheet, which can be extracted by fitting with an exponential function of the type $E(x) = E_\infty - g_0 e^{-x/g_1}$, where E_∞, g_0 and g_1 are fitting parameters, and resulted to be $E_\infty =$-24.56 kcal/mol. However, since calculations of larger substrates are impractical, it is not guaranteed that it is actually converged.
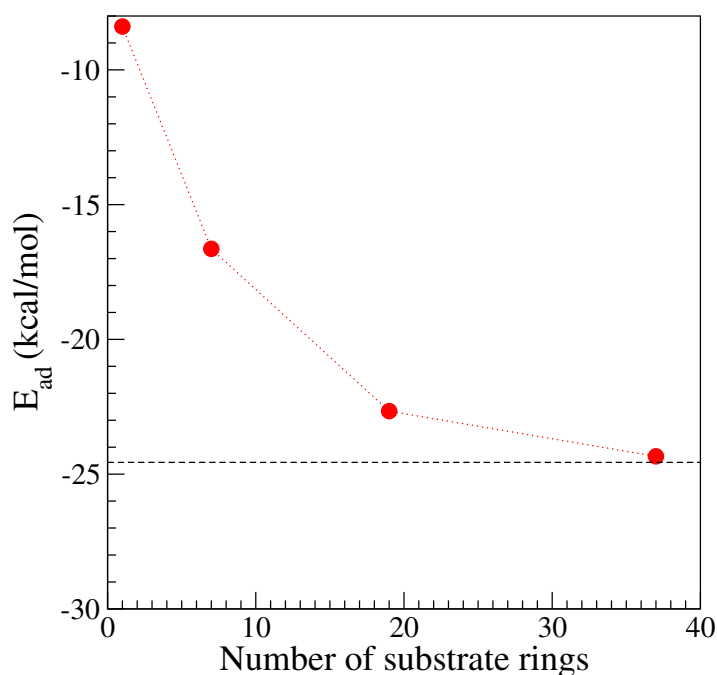
Figure 26: Adsorption energy of a triethyl isocyanurate molecule on polycyclic aromatic hydrocarbons. The black dashed line represents the asymptotic value obtained through fitting of an exponential law.

To avoid this issue, and also obtain a better description of the electronic structure of the substrate, periodic DFT calculations were employed, using the PAW approach as built in VASP with the GGA approximation and the PBE functional. Due to the mainly non-covalent nature of the phenomena studied,

Grimme's empirical dispersion correction terms were also included at the D3BJ level.

A pristine graphene monolayer supercell, comprising 6x6 unit cells was used, with a lattice parameter in the z direction of 20 Å, to minimize spurious interactions between sheets. Under these conditions, a plane wave energy cut-off of 1000 eV was found to be sufficient to achieve a total energy convergence below 1 meV. Concerning the k-point grid used, it was found that 6x6 K-point grid was sufficient to ensure an energy convergence of 10 meV. Geometrical optimizations were performed using the smaller 3x3 K-point grid, and the finer one was used to get single point energies. Unless otherwise specified, the stopping criterion adopted for relaxations is when all forces are smaller than 20 meV/Å. To calculate the interaction energies, the isolated molecule and bare graphene sheet total energies were calculated using the same periodic cell and same conditions (k-points, cutoff).

Methyl isocyanurate (3MIC) ring was placed initially parallel with respect to the graphene plane, at a distance of 3.5 Å, and several adsorption sites were considered, as shown in figure 27. The calculated

C-top

C-bridge

N-top

N-bridge

Ring-top

MIC on G

Bridge
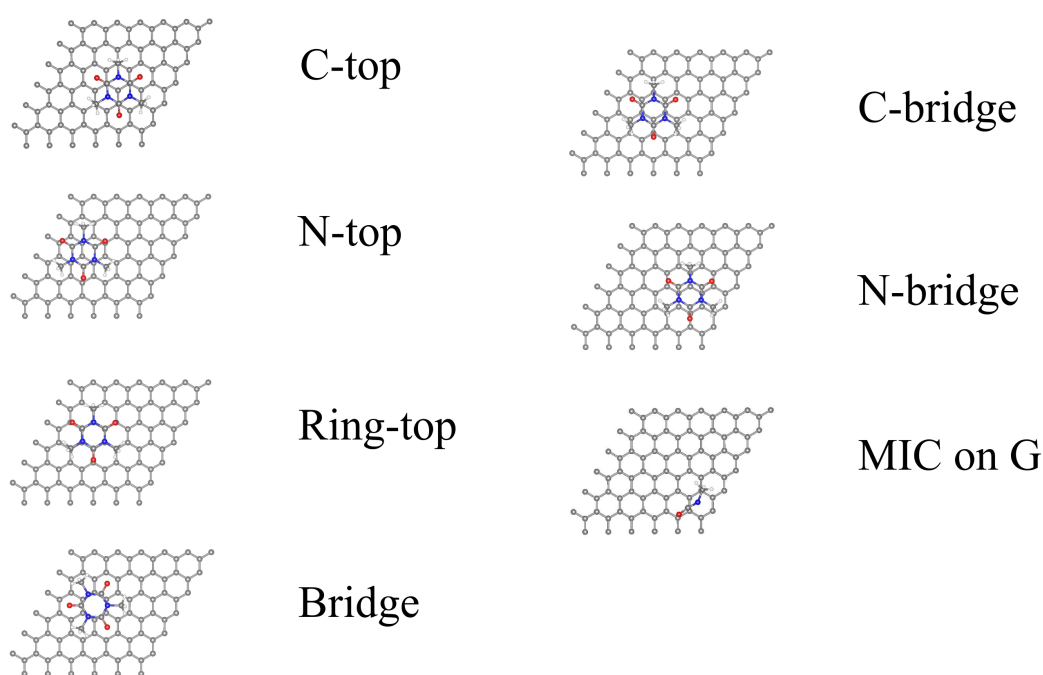
Figure 27: Representation of the stable geometries employed to calculate the adsorption energies of trimethyl isocyanurate on graphene, reported in table 6. Regarding the nomenclature, x-top indicates that the isocyanurate ring center is on top of atom x, while x-bridge indicates that the x-atom of the ring is in a bridge position with respect to the substrate atoms. For other 2D systems, the same convention is followed.

adsorption energies are reported in table 6.

All the tested adsorption sites provided E_{ad} between -16.36 and -17.54 kcal/mol, with the strongest

Table 6: Adsorption energies, calculated at the PBE-D3BJ level of theory, using a 6x6 Γ-centered K-point grid. A graphical representation of the 3MIC and MIC adsorbed geometries is drawn in figure 27.

Adsorbate	Configuration	Supercell size	E_{ad} (kcal/mol)
3MIC	C Top	4x4	-17.61
3MIC	C Top	6x6	-17.50
3MIC	N Top	"	-16.82
3MIC	Ring-Top		-16.36
3MIC	C-Bridge		-16.73
3MIC	N-Bridge		-16.67
3MIC	Ring-Bridge		-16.75
3MIC	Vacancy Top	6x6	-24.78
MIC		6x6	-6.62
PYR	Top	6x6	-21.97
PYR	Hollow	6x6	-23.94

adsorption occurring in a carbon-top configuration, in which the when ring centre and all ring carbons lie on top of graphene atoms (see figure 28). For this configuration, the effects of the periodic box size were checked by calculating E_{ad} for a 4x4 graphene sheet, and a difference below 1% was found, indicating that the 6x6 graphene size is a good choice for 3MIC adsorption studies.

The adsorption energy of methyl isocyanate on graphene was calculated as well, for a conformation where the isocyanate group is parallel to the substrate plane, and found to be only 6.62 kcal/mol, a much smaller value compared to 3MIC. This was expected due to the lower capability of NCO groups to undergo dispersion-dominated interactions.

To have a more general term of comparison,the adsorption energy of pyrene on graphene was calculated, as it is a four-ringed PAH widely used for noncovalent functionalization [211, 212]. The two conformation tested showed larger energies, with the hollow position being more tightly bound with $E_{ad} = -23.94$ kcal/mol. When compared to this value, the 3MIC E_{ad} is only 75 %, however, if E_{ad} is distributed by the number of heavy atoms, 3MIC has the largest value, around -1.98 kcal/mol per atom, compared to the value -1.48 kcal/mol found on pyrene.

The effect of a graphene single vacancy on the adhesion strength has been evaluated by removing, in the C-top configuration, the carbon atom lying exactly under of the ring centre. On the defect, E_{ad} is
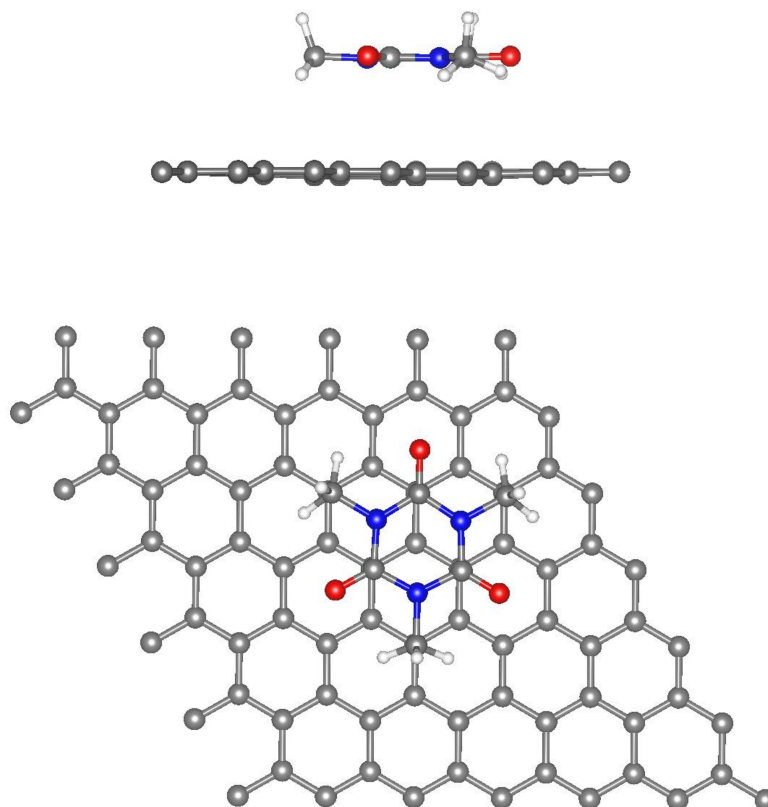
Figure 28: Representation of the c-top adsorption site of 3MIC on graphene, as seen from the c and the a axis.

sensibly improved, with a value of -24.78 kcal/mol found.

    To check whether the substrate properties of graphene might be altered by the presence of 3MIC, the band structures of the graphene sheet with and without the adsorbate were calculated along the $\Gamma K M \Gamma$ path and are reported in figure 29. The Fermi energy of the substrate-adsorbate system (-1.86 eV) is slightly higher when compared to that of the pristine system (-2.21 eV), however,when the bands are compared in terms of $E - E_f$ an almost exact match is found, confirming that the electronic structure of graphene is barely affected by the presence of 3MIC. In fact, a very small band-gap opening of 0.005 eV is found when 3MIC is adsorbed, but this value is too small to be significant and further higher-level calculations are required to confirm the presence of this effect.

4.3.2   Other 2D materials: fluorographene, boron and carbon nitrides

The calculated adsorption energies, obtained considering the same cutoff, k-point grid, vacuum spacing and supercell size as for graphene and considering several conformations for each material, are reported
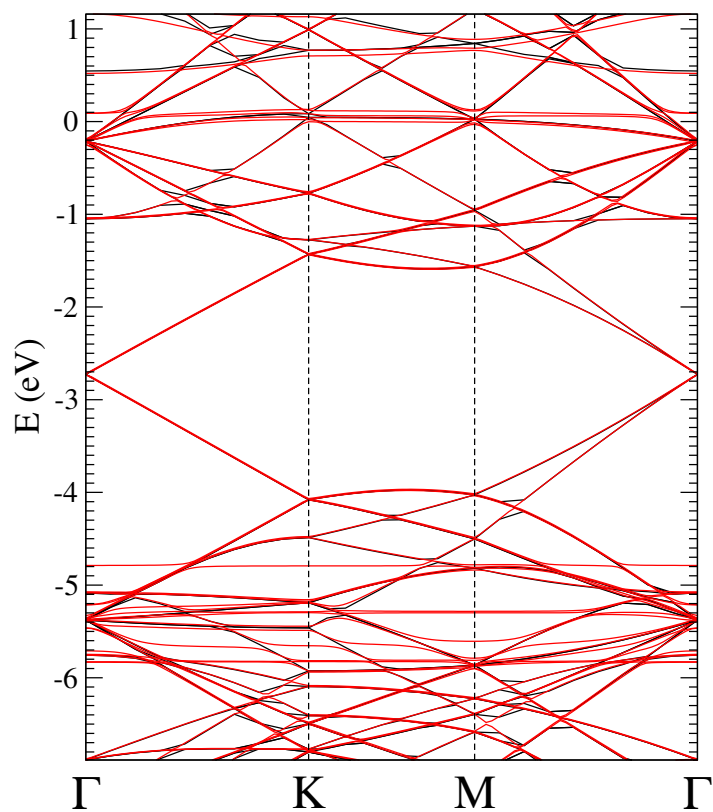
Figure 29: Band structure of pristine graphene (black) and graphene + adsorbate system (red) in the C-Top conformation(see figure 28), calculated along the ΓKMΓ path. Fermi energies were matched to that of pristine graphene to allow a direct comparison. The straight red lines are the energy levels of 3MIC. Due to band folding, the Dirac point is located at Γ.

in table 7.

Fluorinated graphene presents a sparse fence of fluorine atoms on its surface, which clearly reduce the π-π interaction ability of the material. It is therefore not surprising that the lowest adsorption energies are found for 3MIC with this material, with values ranging between -10 and -11 kcal/mol. On the other hand, BN and CN have a much more graphene-like structure, and larger energies are expected. It was found that the 3MIC-BN E_{ad} is slightly lower when compared to graphene (see table 6). However, the differences are small, therefore it can be concluded that, in terms of non-covalent isocyanurate functionalization, both BN and graphene are alike.

Concerning CN, its structure is very peculiar, with heptazine triangles alternated by triangular holes, being responsible for its strong piezoelectric behaviour. It is natural to expect that adsorption energies will strongly depend upon the position of the adsorbate molecule on the sheet. In fact, the highest E_{ad} were found for 3MIC when it is positioned at the centre of the heptazine triangle, while the lowest when it is located on top of a hole.

Table 7: Adsorption energies, calculated at the PBE-D3BJ level of theory, of 3MIC on FG, BN and CN sheets.

Substrate	Adsorbate position	Supercell size	E_{ad} (kcal/mol)
FC	Ring top	6x6	-10.68
FC	H top	"	-11.02
FC	C top		-10.79
BN	Top		-15.21
BN	Bridge		-16.73
BN	N top		-15.97
BN	C top		-16.44
CN	Heptazine centre top	2x2	-17.32
CN	Heptazine side top	"	-13.27
CN	Hole top		-6.87

Resuming, it was found that 3MIC-substrate adsorption energies of the same order of magnitude for graphene, BN and CN, while for FC significantly lower energies were found. Therefore, BN and CN might be non-covalently functionalized by isocyanurate moieties as well as graphene.

4.3.3   On the distortion of heptazine-based carbon nitride

An important factor distinguish CN from the other materials, is the fact that in its lowest-energy state it shows large out of plane distortions, or *buckling* [213]. This introduces an ambiguity in the determination of E_{ad}, because, if it is known that the surface distortion affects adsorption processes [214], it is not clear whether distorted geometry is unique. In addition, although the cause of distortion can intuitively be explained by the repulsion of nitrogen lone pairs that surround triangular holes [213, 214], this statement is not corroborated by theoretical calculations and its origin is not well-established. Driven by these findings, it was decided to investigate more in detail the properties of heptazine-based carbon nitride.

4.3.3.1   Origin of buckling: possibility of a pseudo Jahn-Teller effect

In this section, we wish to establish whether pseudo Jahn-Teller effect can explain the buckling of heptazine-based CN, and various arguments will be presented to sustain this hypothesis. As a first step, the lowest-energy states for an unit cell of g-C3N4 single sheet, containing 14 atoms, were determined. Calculations were performed using a 1000 eV cut-off, a vacuum of 15 Åand a 7x7 k-point grid. As expected, both flat and buckled structures (see figure 31 further in text) could be obtained with the geometrical optimization. The lattice constants are $a = b = 7.124$ Å in the first case, and $a = 6.952$ Å, $b = 6.927$ Å in the second. The buckled geometry has a total energy of -119.84 eV, lower than the flat one by 0.57 eV. This value matches well the difference of 0.59 eV found by Wu and collaborators [215].

The flat geometry has been further refined using a tight convergence criterion for total forces of 10^{-6} eV/Å. Internal symmetry routines of the code, reducing the number of calculations by using the system's symmetries, were switched off to rule out the possibility that they could artificially stabilize the flat geometry. In fact, it was reported that it could not be obtained if not by using constraints [213], but in our case well-converged flat CN sheets were obtained. The Hessian matrix was calculated on the final structures, using a central differences method with displacements of 0.001 Å. All forces resulted to be vanishing, indicating that the flat geometry is located at a minimum of the potential energy landscape (PES), hence it can be regarded as a *high-symmetry reference state* [216]. This rules out the possibility of a Jahn-Teller effect, which would give rise to destabilizing non zero forces. The same argument excludes the presence of steric repulsions cause by nitrogen lone pairs. Once that the JTE possibility is ruled out, the presence of a PJTE is the only possible source of instability for the CN high-symmetry reference state, as predicted by the instability theorem [216]. The normal modes analysis revealed the presence three imaginary frequencies, all describing different out-of-plane buckling distortions modes that are probably related to active PJTE coordinates.

To check for the presence of vibronic couplings between occupied and unoccupied bands, 9 interme-
diate structures were obtained by interpolating the flat and buckled carbon nitride single sheets structures,
and the band structure calculated for each one of them, along the closed $\Gamma K M \Gamma$ path in the first Brillouin
zone.
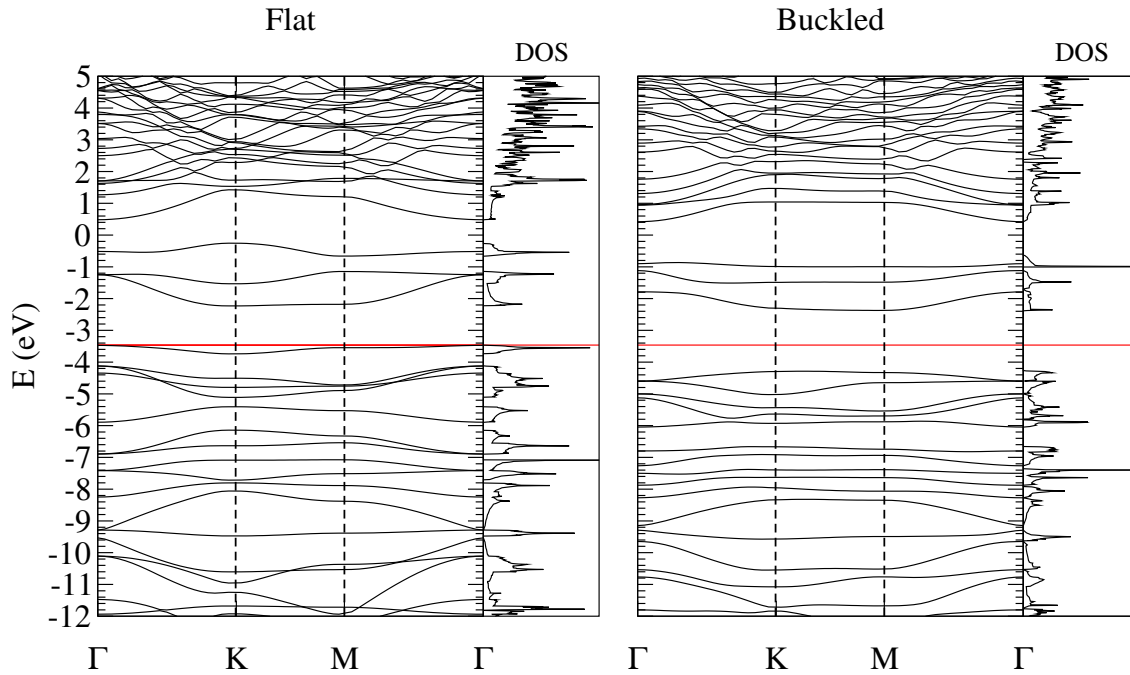
Figure 30: Band structure of a CN sheet, calculated for an unit cell, in its flat (left) and buckled (right) geometry.
The total density of states (DOS) is reported aside each plot. The red horizontal lines denotes the Fermi energy as
obtained from the flat geometry.

Figure 30 shows the band structures of the initial and final conformations. Firstly, a clear effect of the
buckling is a sensible widening of the band-gap, from 1.25 eV to 1.86 eV, mainly due to the lowering of
valence bands energies, particularly evident for the highest energy occupied band. Due to the use of PBE,
these values underestimate the reference value of 2.71 eV and 3.02 eV for the flat and buckled structure,
respectively [215], although the reported band gap type change, from indirect $\Gamma - K$ to direct $K - K$
is correctly reproduced.

By following the evolution of band energies at the Γ point as the structure is progressively distorted,
it is possible to identify pairs of valence and conduction bands with an anti-crossing behaviour, a potential
signature of a PJTE interacton between them [216, 217]. Therefore, possible PJTE active band pairs
could be identified, although a more detailed analysis is required to assess which ones are effectively
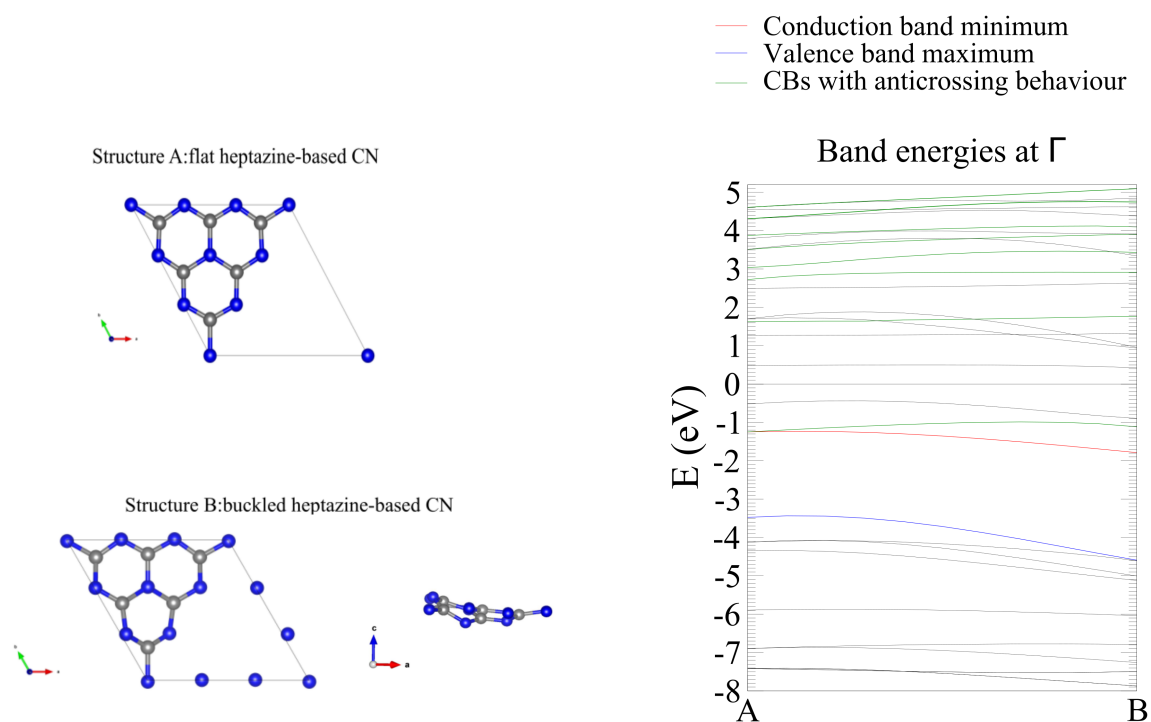
Figure 31: Representation of flat (A) and buckled (B) minimized structure of a CN sheet. For the buckled structure, a side view along the b axis is also provided. The plot on the right reports the change of band energies as the structure is progressively distorted. The valence band maximum (VBM) and conduction band minimum (CBM) are highlighted. The bands coloured in green represent those which could potentially contribute to the PJTE. Distortion path was obtained by interpolating the initial and final conformation geometries.

contributing to the distortion. As part of further research, the states effectively coupled will be identified by studying their simmetry, and their vibronic coupling strength evaluated by a characterization of the electron-phonon interactions. While established methods exists to estimate the PJTE coupling strength for non-periodic systems, their extension to infinite systems is still an open field of research. Nevertheless, the result obtained here strongly points out the PJTE as the main mechanism of instability of the flat structure.

4.3.3.2   Size effects

It is well established that the lowest-energy conformation of heptazine-based carbon nitride sheets is buckled, and in previous section results supporting the PJTE origin of distortion have been presented. At this point, it is important to assess the role of periodic boundary conditions on the distortion modes. To our knowledge, this point has not been addressed in literature.

For this purpose, CN monolayers of different sizes (1×1, 2×2 ad 3×3 unit cells were created, and

97

optimized to their high symmetry reference state, using 7×7, 5×5 and 3×3 K-point grids, respectively. In all cases, the optimization successfully converged and the electronic energy per unit cell resulted to be -119.27 eV, with differences below 1 meV. The results obtained are reported in table 8.

Table 8: Electronic energies for different-size CN sheets, considering flat and buckled structures. For 2x2 and 3x3 sheets, SP stands for smaller periodicity, i.e. the same as in the 1x1 sheet, and LP stands for long periodicity.

Cell size	Conformation	E (kcal/mol)	E (kcal/mol per unit cell)
1x1	Flat	-119.27	-119.27
1x1	Buckled	-119.84	-119.84
2x2	Flat	-477.08	-119.27
2x2	Buckled SP	-479.36	-119.84
2x2	Buckled LP	-479.94	-119.99
3x3	Flat	-1073.44	-119.27
3x3	Buckled LP	-1083.33	-120.37

When a small distortion is induced by means of a displacement of the atomic positions, the optimization leads to buckled structures. In the smallest system, the energy of the distorted systems is -119.84 eV, and clearly has a unit-cell periodicity. A 2x2 buckled supercell can be obtained simply by replication of the unit cell. In this case, the distortion obviously has a periodicity of one unit cell, and the total energy is practically identical with respect to the buckled unit cell.

If, alternatively, the distortion is obtained by a perturbation of the 2x2 flat sheet, another buckling conformation is obtained, and is found to have a lower total energy, of -119.99 eV. Considering a larger 3x3 sheet, yet another motif is found, with an even lower energy of -120.37 kcal/mol. By looking at figure 32, it is evident that the distortion pattern is heavily dependent upon the periodic cell size: each one of them would only allow those patterns with a spacial periodicity equal or smaller than the cell dimension itself, artificially filtering out the larger wavelength modes. Therefore, an ambiguity is found about the determination of the lowest-energy geometries of distorted heptazine carbon nitrides: the periodic box size allows -or prevents- some distortion modes. In principle, it is not excluded that, by considering larger or non-squared cells, other distortion modes might be found.

An important consequence of this is that adsorption energies calculated on them should be carefully verified, because each possible conformation of the CN sheet is slightly different from the others in terms of the relative orientation of heptazine triangles. Whereas this effect could be neglected for chemisorption,

1x1

2x2

3x3
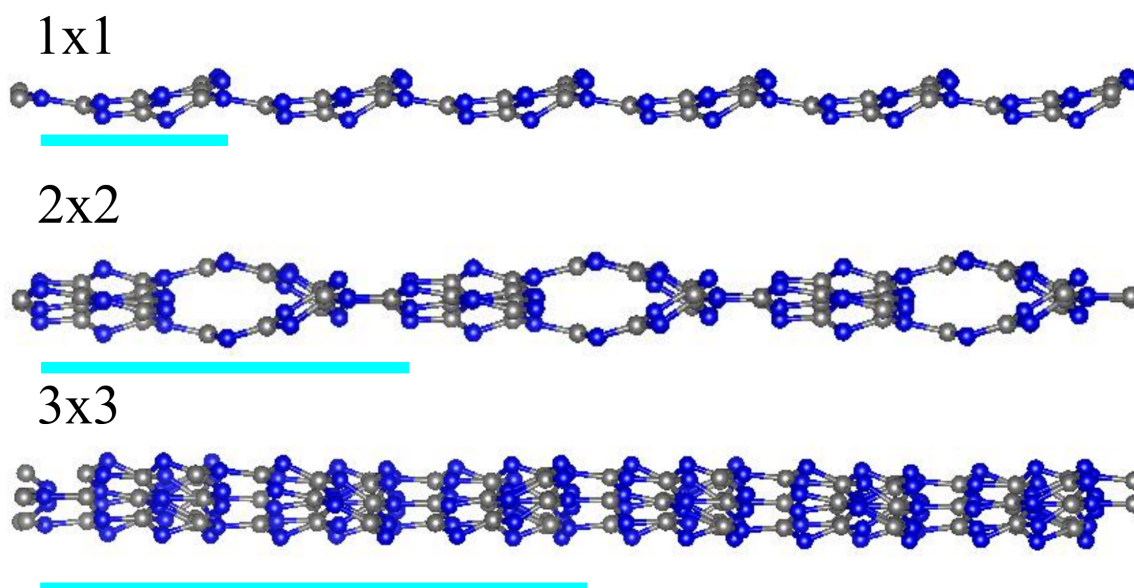
Figure 32: Distortion modes of CN single sheet for different supercell sizes. The sheets are seen along the b axis and the size of periodic box is highlighted.

where most of the interaction energy can be localized in the correspondence of the created chemical bond(s) with the substrate, in the case of physisorption this could have a significant impact, due to the long-range nature of non-covalent interactions. For instance, the 3MIC-CN energies presented in the previous section were obtained considering a 2x2 CN sheet in the same large-periodicity conformation as in figure 32. Yet, it is not guaranteed that the same energy can be found considering larger sheets.

More generally, it should be critically assessed to which extent the periodic cell size might select the permitted deformation modes of CN and, by consequence, how all the properties that directly or indirectly depend upon them are affected.

4.3.4 Formation and stability of isocyanurate monolayers on graphene

The strong non-covalent binding of isocyanurates on various substrates naturally leads to the question whether a stable isocyanurate monolayer could be self-assembled on them. To answer this, it is necessary to evaluate the cohesive energies of such arrangement and its stability against the dissolution in a solvent.

As a first step, the cohesion energy of a free-standing 3MIC monolayer has been determined by DFT calculations. A periodic structure was found, characterized by an hexagonal cell with $a = b = 8.41$ Å and $\gamma = 60$ degrees, as it can be seen in figure 33. Each ring is rotated by $\pi/6$ degrees with respect to its neighbours, in such a way that each oxygen establish $CH \cdots O$ bonds with one of neighbouring

molecules' methyl group hydrogens. The cohesive energy of the crystalline monolayer was found to be -7.00 kcal/mol. Since $CH \cdots O$ bonds are among the weakest non-covalent bonds [218], this relatively low value is not surprising.
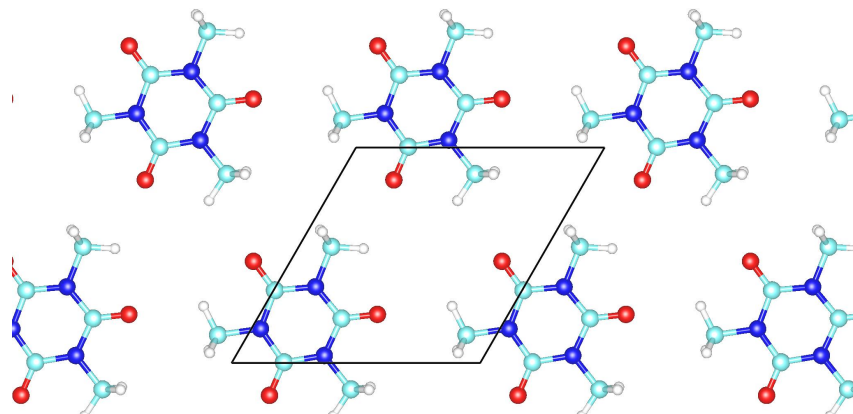
Figure 33: Predicted crystal structure for a trimethyl isocyanurate monolayer, as seen from the c axis. The lattice parameters are a=b=8.41 Å.

Considering a stacking type as the one discussed earlier for 3MIC dimers, a 3D graphitic-like structure can be devised, in which rings are stacked along the z axis, each one rotated by $\pi/6$ with respect to the lower one. This arrangement was found to have a larger cohesive energy of -17.99 kcal/mol and an interlayer spacing of 3.391 Å.

For comparison, the crystal structure of 3MIC, measured by Thalladi and collaborators [219] and reported into the Crystallographic Open Database(COD) [143], was optimized at the PBE-D3 level of theory, with a plane-wave cutoff of 1000 eV and a $2 \times 2 \times 3$ k-point grid, and shown in figure 34. No flat planes are present in the 3MIC crystal, rather it is formed by layers of rings, forming dyads, with different reciprocal orientation. Its cohesive energy was found to be -22.27 kcal/mol, representing the most stable structure.

The relatively low cohesive energy of 3MIC monolayers makes them very unlikely to be found as free-standing sheets, as it is expected that the weak $CH \cdots O$ bonds will be easily disrupted at higher temperatures. However, the presence of a flat substrate such as graphene could trigger its formation and help to stabilize it due to non-covalent interactions. To prove this, MD simulations were performed of 3MIC on a graphene monolayer substrate of ca 50×50 Å made by 1008 atoms, for which the standard GAFF parameters were used, while retaining GAFF-IC for the isocyanurate. Simulations employed a box periodic in the x and y directions and non-periodic along the z direction, and were conducted under NPT conditions at 298 K and a barostat coupled to the x and y directions and a target pressure of 0 atm. Non-bonded interactions were cut at 13 Å, and no long-range scheme was employed. A reflective wall,
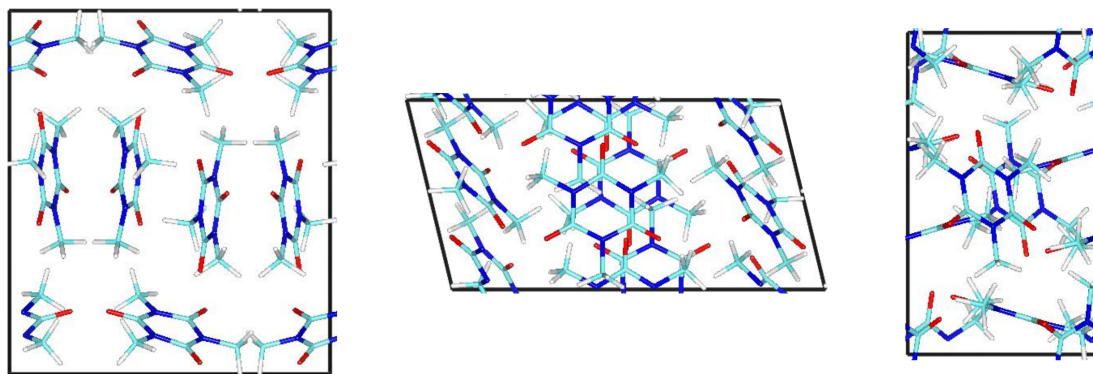
Figure 34: Crystal structure of trimethyl isocyanurate, obtained from [219], observed along the a (left), b(center) and c(right) axis.

which inverts the z component of momentum of all incoming atoms, was set at the upper bound of the box, in order to prevent atoms to escape the box.

By adding 64 3MIC molecules to the substrate in vacuum conditions, a crystalline 3MIC monolayer is quickly formed, with 42 molecules entirely covering the graphene sheet. The excess isocyanurate was removed and the system's temperature lowered to 0.15 K. As can be observed in figure 35, the monolayer reproduces almost exactly the hexagonal packing predicted by DFT methods, with the MD lattice constants, estimated from the square root of the area per molecule, found to be approximately 7.81 Å, smaller by 7.1 %. At 0.15 K, the graphene-3MIC layer interaction energy is -22.20 kcal/mol/molecule, slightly overestimating PBE results (see table 6), but underestimating the non-periodic B3LYP-D3 E_{int}. In view of a force field reparametrization to improve the description of ring-based interactions, this means that the reference DFT method should be chosen with care.

To obtain information upon the stability of the 3MIC monolayer, the desorption ΔG_d free-energy was estimated by calculating the potential of mean force with respect ot the collective variable ξ defined as the distance between the centre of mass of 3MIC and that of the graphene sheet. PMF curves are reported in figure 35, right top panel, for a single adsorbed molecule and a fully formed monolayer. In the first case, the PMF unsurprisingly shows one minimum, corresponding to the 3MIC adsorbed on the substrate, with $\Delta G_d = -16.22$ kcal/mol. On the other hand, the desorption process of a single molecule from the substrate is very different. In particular, the global PMF minimum correspond to the desorbed molecule stacked on the 3MIC monolayer, and not to the fully adsorbed state. Removing a molecule from the monolayer appear to be a two-step process in which firstly the molecule abandons the layer and reabsorbs on the 3MIC substrate, with a barrier of 5.1 kcal/mol in this case, and then it completely abandons the
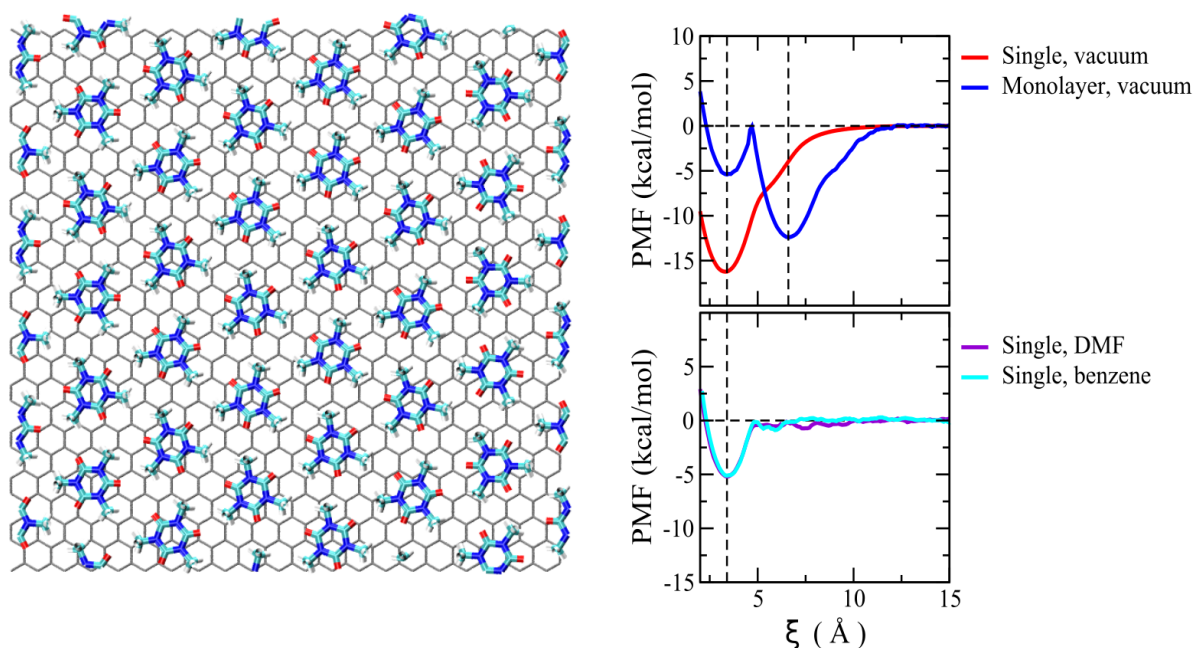
Figure 35: On the left, the self-assembled monolayer os 3MIC at 0.15 K of 3MIC on graphene, seen from the top. The hexagonal packing, driven by weak hydrogen bonds and stabilized by the substrate is clearly visible. On the right, PMF desorption curves calculated in vacuum (top) and solvated(bottom) conditions.

surface, with a ΔG_d in this case is -12.3 kcal/mol, and a (global) minimum a 6.8 Å as reference point.

The stability of monolayers was further tested by calculating the PMF of desorption process in presence of a solvent. For this purpose, dimethyl formammide (DMF) and benzene were used as a polar and an apolar solvent, respectively, and parametrized using GAFF. A thousand molecules were added to the graphene-3MIC substrate and the system equilibrated until the solvent formed a thin film and a liquid-gas interface. During this step, no desorption from the monolayer was observed. Once the systems were equilibrated, the PMF was calculated at 298 K, initially for the desorption process of a single attached molecule. As can be appreciated in figure 35, bottom right panel, the solvent presence significantly lowers the desorption free energy, with DMF and benzene greatly reducing ΔG_d to -5.00 kcal/mol.

Due to the two-step nature of the monolayer dissolution, PMF calculations for monolayers are very difficult to obtain. Despite this, the initial ΔG_d required to remove one molecule from the monolayers can still be estimated by a PMF calculation in which an upper bound of 5 Å is set for ξ. In this way, barriers of 4.80 kcal/mol and 5.58 kcal/mol are found for benzene and DMF respectively. These are very close to the barrier obtained in vacuum, suggesting that once the 3MIC layer is formed, its stability is marginally influenced by the environment. In fact, the monolayer entirely prevents the solvent molecules to attach onto the substrate, rendering the dissolution process very difficult. Concerning their formation, while in

vacuum the process is very fast and directly observable by means of simulations, the same does not hold in solvent, because its presence considerably slows down the assembly dynamics, making a direct simulation not practical due to the long times required.

4.4   Conclusions

In this chapter, intermolecular interactions between isocyanurates and isocyanates have been studied in detail, both using ab-initio methods and liquid-phase MD simulations. The nature of intermolecular interactions of aliphatic isocyanurate has been clarified, as well as their effect in the microscopic structure of isocyanurate liquids.

It was shown by SAPT calculations that isocyanate groups only weakly interact with one another through a combination of dispersion and electrostatic forces due to their dipole moments. Isocyanurate rings on the other hand were proven to be strong non-covalent interaction sites, with stacked dimers exhibiting a large intermolecular interaction energy. This interaction is dominated by dispersion contributions, arising from the many π orbitals perpendicular to the ring plane. Such strong dispersion character suggests a possible application of isocyanurates as non-covalent functionalization agents of two-dimensional materials. Moreover, ring-ring interactions modulate the microscopic structure of isocyanurate liquids, either functional or not.

The third interaction type that was investigated, namely between isocyanates and isocyanurates, lies in between the other two, and turned out to be the key to understanding the viscosity of functional isocyanurate liquids. This interaction is of the same order of magnitude as the isocyanate-isocyanate interactions, but, unlike them, is dispersion-dominated because of the $\pi \cdots \pi$ interactions with the isocyanurate ring. In functional systems, containing both isocyanates and isocyanurates, this leads to two effects. At short distances, the presence of isocyanate-isocyanurate contacts reduces the occurrences of ring-ring stacked assemblies. At longer distances, the presence of isocyanate-isocyanurate contacts increases the intermolecular interaction energies by means of cooperative effects, in conjunction with the isocyanate dipole-dipole interactions. This second effect causes a significant increase in the cohesive forces in the liquid state, leading to increased viscosity. Thereby, it was possible to relate the viscosity of isocyanate-isocyanurate liquids to the density of isocyanate-isocyanurate (NR) contacts.

Further, it was shown that the isocyanurate ring is capable to bind strongly and non-covalently to a graphene substrate, with calculated adsorption energies only 25 % smaller with respect to pyrene. The electronic properties of graphene, in terms of its band structure, are not affected by the presence of the

3MIC, confirming its capability to keep intact the substrate properties. On the other materials tested, good adsorption energies were found for boron and carbon nitride, while lower values were encountered in the case of fluorinated graphene, because of the lack of the former to host strong non-covalent interactions.

The structure of heptazine-based carbon nitride sheets was investigated more in depth, revealing that, on one hand, the distorted minimum energy structure is probably consequence of a pseudo Jahn-Teller effect and, on the other hand, distorted geometries are dramatically affected by the periodic size effects.

MD simulations performed in vacuum conditions demonstrated that 3MIC molecules self-assemble into an hexagonally packed monolayers, which stability at ambient temperature has been confirmed by desorption free energy calculations. It also appeared to be stable under the presence of a polar and an apolar solvent. These results indicate that not only isocyanurates could functionalize non-covalently various 2D materials, but also that the so-obtained functionalization is stable at room temperature, hence can undergo mild processing routes without being disrupted.

Chapter 5

Formation and study of isocyanate-crosslinked networks

The simulation of the formation of crosslinked networks and nanogels from isocyanate end-functionalized chains is presented. After defining the dissipative particle dynamics scheme and the implementation of chemical reaction in the model, networks and nanogels are investigated by characterizing their swelling and topological properties. Different processing conditions and simulation strategies are compared, in order to assess their impact on the network properties.

5.1 Motivation

In previous chapters, isocyanates and isocyanurates were studied from an atomistic point of view, to understand their liquid state dynamic properties. However, in the majority of applications, they are always reacted to generate larger structures, such as linear or crosslinked polyurethanes, which typical length and time scales usually exceed those accessible by atomistic methods. Here, the formation of crosslinked networks will be addressed, and methods to investigate their features introduced and applied. A coarse-grained approach, namely dissipative particle dynamics (DPD), has been used to effectively simulate these structures, conjugated with a relatively simple scheme for the crosslinking chemical reactions. In particular, nanogels were adopted as a case study, not only because they allow a simpler study of their swelling properties, but also for their interesting biomedical applications, as reviewed in the first chapter.

5.2   Definition of the simulation model

5.2.1   Assignment of DPD parameters

The simulated system consists of a melt of polyethylene glycol (PEG) chains end-functionalized by iso-cyanates. To define the DPD (see section 2.5.4) interaction parameters, all-atomistic MD simulations were performed to obtain the ΔH_{vap} and δ_i, for each constituent of the precursor system. In particular, simulations of 100 PEG-28 chains, 1000 ethyl isocyanate molecules and 343 propyl isocyanurate molecules were performed under NPT conditions at 298 K and 1 atm, using GAFF-IC for isocyanate-containing molecule and standard GAFF for PEG. To calculate the Flory-Huggins χ_{ij} an unique average bead volume of $v \equiv 110\,\text{\AA}^3$ was used. Incidentally, this also defines the length scale of the simulation: $r_{DPD} = (\rho v)^{\frac{1}{3}} = 6.91\text{\AA}$. The repulsion parameters a_{ij} are equal to 25 when $i = j$, and the DPD density was kept fixed to 3.0 DPD units in all simulations. The interaction parameters are reported in table 9 for the different types of beads.

Table 9: DPD interaction parameters for all species appearing in the simulations. Concerning the not fully crosslinked beads, their DPD parameters are assumed to be equal to those of isocyanate beads.

Bead type	PEG	Urethane	Isocyanate	Ring	Alkyl
PEG	25	25.69	25.03	26.32	36.02
Urethane		25	25.42	25.10	31.9
Isocyanate			25	25.93	34.85
Ring				25	29.70
Alkyl					25

Polymers were modeled as a bead-spring chains , with harmonic bond and bending potentials. Regardless their type, all DPD beads are assumed to have the same mass and volume. The equilibrium length of all bonds was set to $0.434\,r_{DPD}$ and a stiff spring constant $K_{bond} = 500$ was used. Such choice reflects the MD monomer-monomer distance, calculated to be 3.03 Å, while the large bond force constant helps to prevent unphysical chain crossings. To further enforce this condition, a segmental repulsive pair (SRP) potential [178] was used with a range of 0.4 r_{DPD} and a force constant of 100 DPD units. Equilibrium angles of $\pi/2$ radians and a spring constant $K_{bend} = 0.5$ were adopted as well, to better match the PEG bending angle distribution observed in MD. When crosslinking (CL) beads are present, they

represent symmetric isocyanurate trimers. In view of this, a bending potential with an equilibrium angle $\theta_{eq} = 3\pi/2$ radians and $K_{bend} = 1$ was employed for all those angles having a CL bead as vertex.

Concerning solvent-gel interactions, the solvent has been made insensitive of polymer bead type and only one repulsion parameter a_{sg} was used to describe all the interactions between nanogel and solvent. To replicate the swelling transition, a_{sg} was varied from 15 (very good solvent) to 50 (very poor). When mentioned, good solvent conditions are equivalent to $a_{sg} = 25$.

Initial polymer and polymer-solvent configurations were randomly generated in a cubic periodic box at the target density, and equilibrated for 50000 τ_{DPD}. Three independent runs were considered for every system. All simulations were performed using LAMMPS [156] and the DPD implementation therein.

To verify whether the final melts are equilibrated, the mean squared internal distances (see section 2.5.1) can be calculated and compared to the expected behaviour for the mean square end-to-end extension [168].
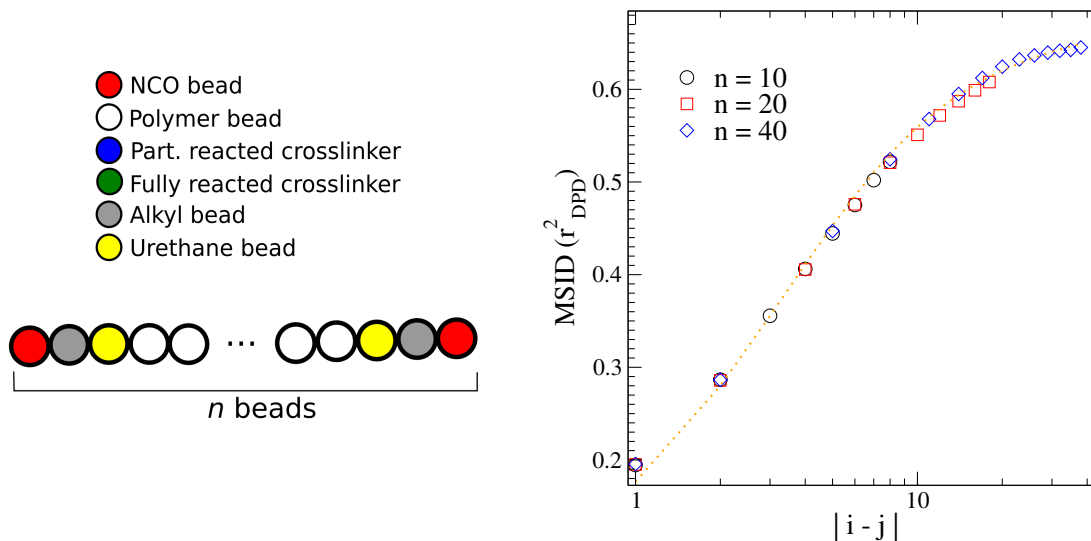
Figure 36: On the left, a scheme of the chain model adopted for isocyanate-end functionalized PEG chains. On the right, mean square internal distance for melts of chains of n=10, 20 and 40 beads. The x axis is the chemical distance between beads of the same chain. The orange dotted line is a fit to equation (3) of reference [168].

As reported in figure 36, where the MSIDs of equilibrated melts of 4000 n=10 and n=20 beads and 2000 chains of n=40 beads are compared, all curves show the expected behaviour for equilibrated melts, thus representing reasonable initial states for the network formation process. Concerning the presence of entanglements, calcualted using the Z1 code, the averaged number of kinks per chain $< Z >$ was

0.009, 0.135 and 0.554 for n=10, 20 and 40, respectively. Since the simulated chains are relatively small, all melts are weakly entangled. The obtained values are in line with those calculated for equilibrated melts of Kremer-Grest polymer chains [173], confirming that the DPD model represents well the chain entanglement.

5.2.2 Crosslinking reaction modelling

To simulate the crosslinking reaction, a distance-based routine, written in C and interfaced to LAMMPS output files, has been written. The reaction scheme is shown in figure 37. When invoked, the code searches for all the reactive beads closer than $d = 0.8$ distance units. Each reaction has a predetermined probability to happen, under the constraint that any bead cannot react more than once per iteration. To take into account reversibility, bond-breaking reactions were also included into this scheme. Equal probabilities $p = 0.4$ were set for dimerization and trimerization, while a $p = 0.04$ was chosen for dimer dissociation. After every reaction step, the system connectivity and topology is updated. Reactive
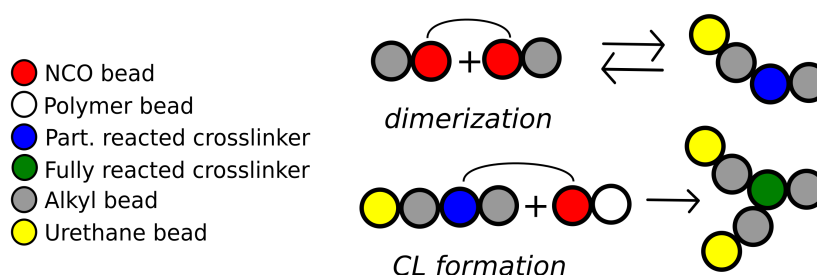
Figure 37: Scheme of the reaction model adopted. The dimerization reaction is reversible, while the trimerization is not.

iterations are performed every 2.5 τ_{DPD}, to guarantee proper relaxation and diffusion between reaction steps. Abrupt changes in potential energy or temperature were never observed. The formation process was carried on until at least 90 % of the initial reactive bead content is fully reacted. To achieve this, 5000 to 40000 iterations were required, depending upon the reactive ends density of the system under consideration.

To test the end-crosslinking reaction, periodic networks were assembled according to the scheme reported in figure 38, starting from unsolvated melts of 4000 (n=10 and n=20) and 2000 (n=40) chains. As expected, the reaction speed is proportional to the concentration of reactants, which for end-terminated chains depends upon their length. The fraction of linear linkages drops asymptotically to negligible values after reaching an initial maximum, as they are consumed to form CL beads. An asymptotic behaviour is clearly observed for the CL bead formation, indicating that a fully reacted network in which all end-crosslinking
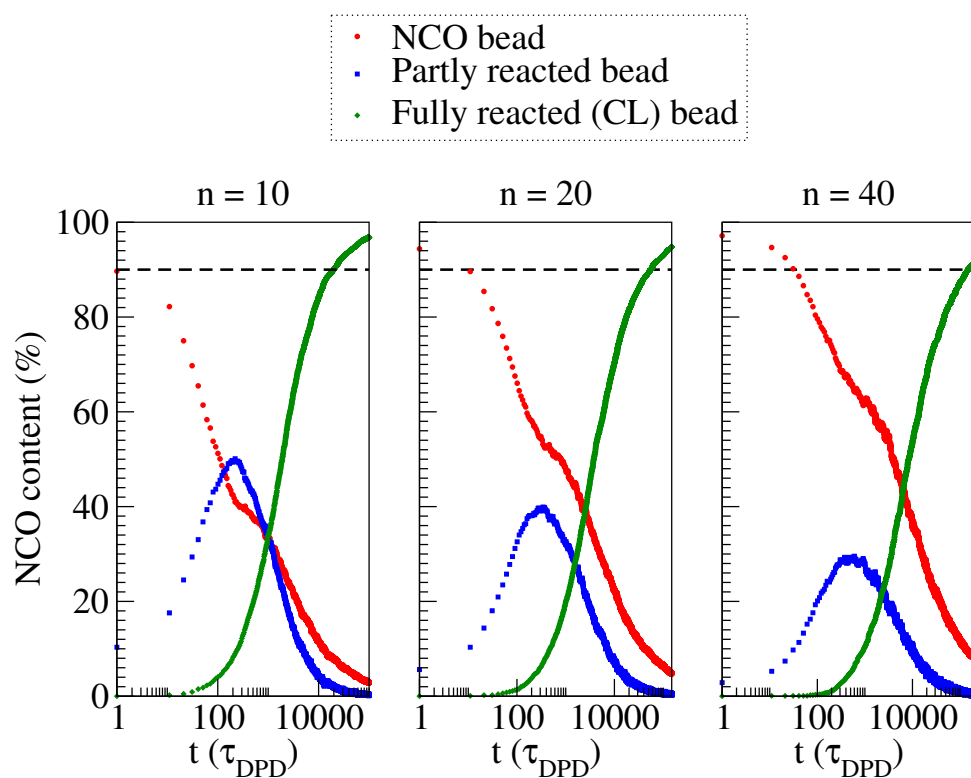
Figure 38:   Time change of the reactants and products content, expressed as percentage with respect to the

initial reactant content, for different precursor lengths. For longer chains the reaction is slower, due to the lower

concentration of reacting beads.

beads trimerized into CL beads is reachable in the long time limit. This agrees with experimental findings, which show full conversion of isocyanate groups [41].

It is interesting to test the hypothesis of reversible linear linkages, by comparing the results obtained for the case of irreversible dimerization (by zeroing the dissociation probability). As reported in figure 39, the ratio of crosslinkers quickly saturates as the reaction continues and cannot proceed further because the reactive ends are 'blocked' within the linear linkages, leading to a final network with a significantly lower amount of crosslinkers. Thus, the dimerization step reversibility is fundamental to obtain highly crosslinked networks.
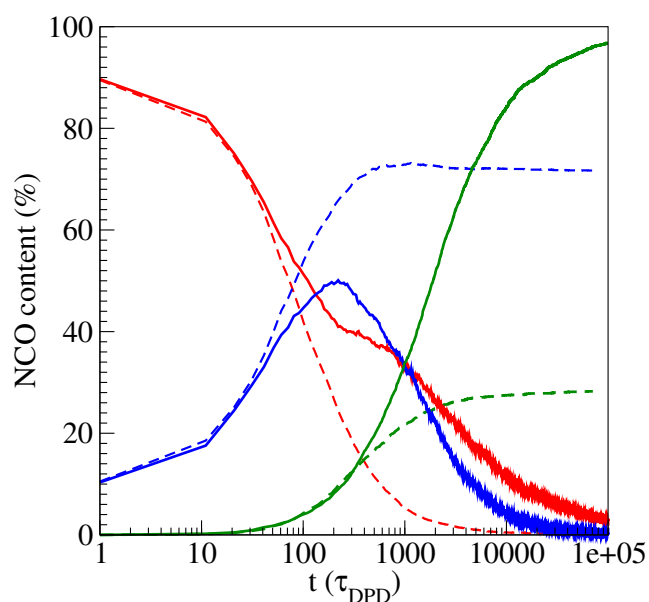
Figure 39: Comparison of the reactants (chain ends) and products (crosslinking beads) for the cases of a reversible (full lines) and irreversible (dashed lines) dimerization reaction scheme. Colour legend is the same as in figure 38.

The network topology has been inspected by counting CL and linear linkage (LL) beads, as well as CL beads concentration and CL functionality, that is the average number of bonds involving both CL and LL beads. Since crosslinked structures are obtained in a realistic way, it is natural to encounter defects in the network structure, which affect its elastic behaviour. In an ideal network, CL points are evenly distributed in space and fully reacted, and connected to its nearest neighbours through unentangled and monodisperse chains. On the other hand, a real network will certainly contain a series of defects, depicted in figure 40, which change their mechanical properties. Dandling ends are polymer chains that are attached to the network by one end but not by the other while 'tadpoles' are chains whose both ends are attached to the

same CL point. These defects are elastically inactive because when the network is stretched, they do not connect two distinct points of it. A n-loop consists in n crosslinking points connected simultaneously by n chains. 2-loops might contribute in first approximation to the network elasticity as elastic strands, while 3- and 4-loops are not defects in a strict sense and can be regarded as network features. For each crosslinked system, all defects were counted up to 4-loops, by using a specific code that explore the network by means of walkers that, starting from each CL point, travel along its connected chains. Furthermore, the average strand length has been calculated, a strand being defined as a chain connecting two CL beads. A primitive path analysis has been performed to quantify the entanglement of melts and networks.
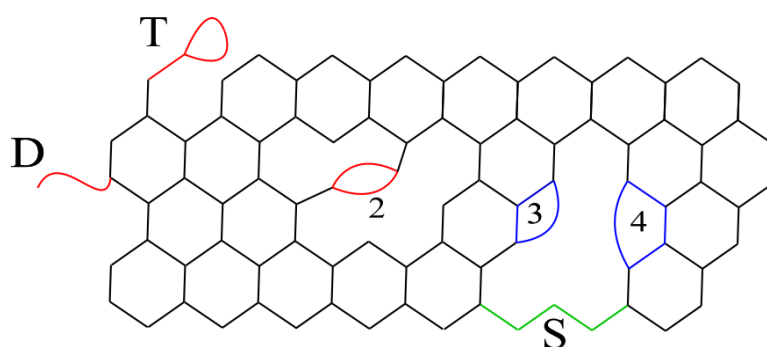
Figure 40: Schematic 2D representation of a crosslinked network, where each segment correspond to a chain and each junction to a CL point. Examples of dandling ends (D), tadpole (T) 2-loops (2), 3-loops (3) and 4-loops (4) are drawn. 3- and 4-loops are not real network defects, thus have been coloured differently. An example of an elastic strand (S) is also provided, in green.

5.2.3   Nanogel synthesis and swelling

Once that the networks are fully formed, the simplest way to take a nanogel is by carving out a sphere from them, in such a way that all chains severed in correspondence of intra-chain bonds are entirely stripped off, and all the resulting small disconnected parts removed. To avoid bonds crossing the periodic boundaries, the maximum allowed cut-off radius is $r_{max} = L/2 - 0.5$, L being the periodic box length. The nanogels obtained in this way have an inner structure corresponding to that of the bulk network and an outer layer with a looser structure, because of the inevitable creation of dandling chains.

Alternatively, the reaction can be performed in spherical confinement region, so that the final reaction product is already a nanogel and no further handling of the system is needed [183]. This method is closer to the synthesis of nanogels in a nano-emulsion, in which the reacting polymer is confined into immiscible droplets of liquid in solution.

A third approach [220] consists in joining a set of randomly distributed CL beads with straight chains of the desired length, under periodic boundary conditions. In this case, the nanogel still needs to be carved out, but the reaction phase is completely skipped. This method is certainly more convenient in terms of computational time and also has the advantage of naturally avoiding many network defects, such as tadpole loops. However, it is expected that such networks would have strong internal forces, as the randomly created chains are generally out of equilibrium.

Independently of the method used to obtain them, nanogels were put into a larger periodic box, with at least $L = 50\,r_{DPD}$ and solvent particles were added in the required amount to have a global total density of $\rho = 3$. The nanogel centre of mass was kept fixed to the simulation box origin. Subsequently. the solvated systems were equilibrated under good solvent conditions for at least $10000\ \tau_{DPD}$ or until stationarity of the radius of gyration R_g was reached.

5.3   Properties of isocyanate-based nanogels

To investigate the properties of isocyanate-based nanogels, swelling transition curves were obtained by tuning the solvent-gel interaction parameter a_{sg}. For every value, simulations of $6000\ \tau_{DPD}$ were run, the last $2000\ \tau_{DPD}$ of which being used for data production. Following this, nanogels' gyration radii, swelling ratios, radial densities and form factors were measured. In the following section, different chain lengths, nanogel creation methods, synthesis routes and solvent presence are considered to understand their effect on nanogel final properties.

5.3.1   Chain length dependence

Nanogels were obtained from reacted networks made from n=10, 20 and 40 chains by carving them out from the melt. When applying this method, the cut-off radius should be chosen in such a way that the final nanogel is large enough to have a well defined internal structure, but not too large in order to ease the computation, especially when solvent is added. In figure 41 it is shown that, in order to have representative nanogels, the resulting collapsed radius of gyration should be of at least 7 DPD units for n=10 and n=20, corresponding to a cutting radius of at least 11.5 DPD units. Whereas enlarging this value slightly affects the swelling ratio, shorter values are insufficient to retain a good internal network structure, and the larger swelling observed are due to the fact that these 'nanogels' open up completely and lose any shape when swollen.

As shown in figure 42, all nanogels undergo the expected swelling transition when put in solvent. In

112
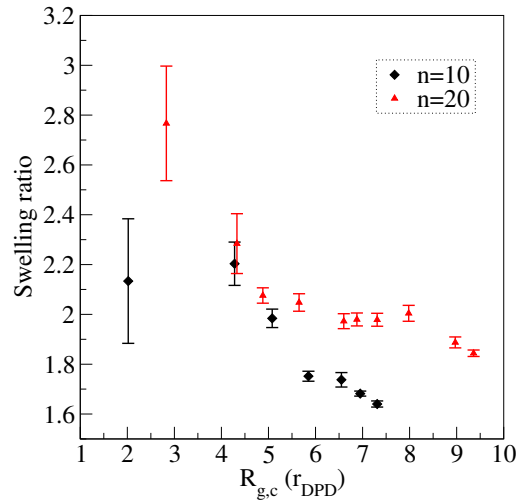
Figure 41: Swelling ratios for n=10 and n=20 nanogels with different collapsed radius of gyration, which is proportional to the cutting radius and the nanogel number of beads.

the collapsed state ($a_{sg} = 50$), they assume a spherical shape with well-defined borders and a central density of 3.5 N/r_{DPD}^3, regardless of the internal structure. This high density value is caused by the short equilibrium bond lengths adopted in this model. By using the typical value of 0.6 r_{DPD}, a density of 3 N/r_{DPD}^3 is recovered. In terms of swelling ratios, the results are unaffected by this change, as setting larger bonds is equivalent to a rescaling of the bead internal distances. It was decided to present here the results with the shorter bond lengths, as they were obtained through a mapping of an all-atom representation to DPD.

On the other hand, nanogels can be clearly differentiated when swollen. As the precursor chain length is increased, lower CL beads densities are found, resulting into an increase of the average elastic strand length, as can be seen in table 10. Consequently, longer chain-made nanogels present larger radii and lower densities in the swollen state. The calculated structure factors confirm these observations, showing the hard-sphere scattering pattern for a collapsed nanogel and fuzzy sphere curves in the swollen state. Regarding the latter, is possible to see that the first $P(q)$ peak, corresponding to length scales typical of the nanogel sizes, are sharper for shorter precursor length nanogels. Finally, it is worth noting that a sharper swelling transition is found for longer chain networks, as predicted by theory [221].

Concerning their topological features, the lower CL functionality encountered in longer chain networks is reflected by the increased percentage of elastically inactive defects, which includes both dandling ends and tadpoles. Interestingly, the increased number of defects for n=40 is mainly due to a larger number of dandling chains, while the number of tadpoles is significantly lower. This is a consequence of the fact
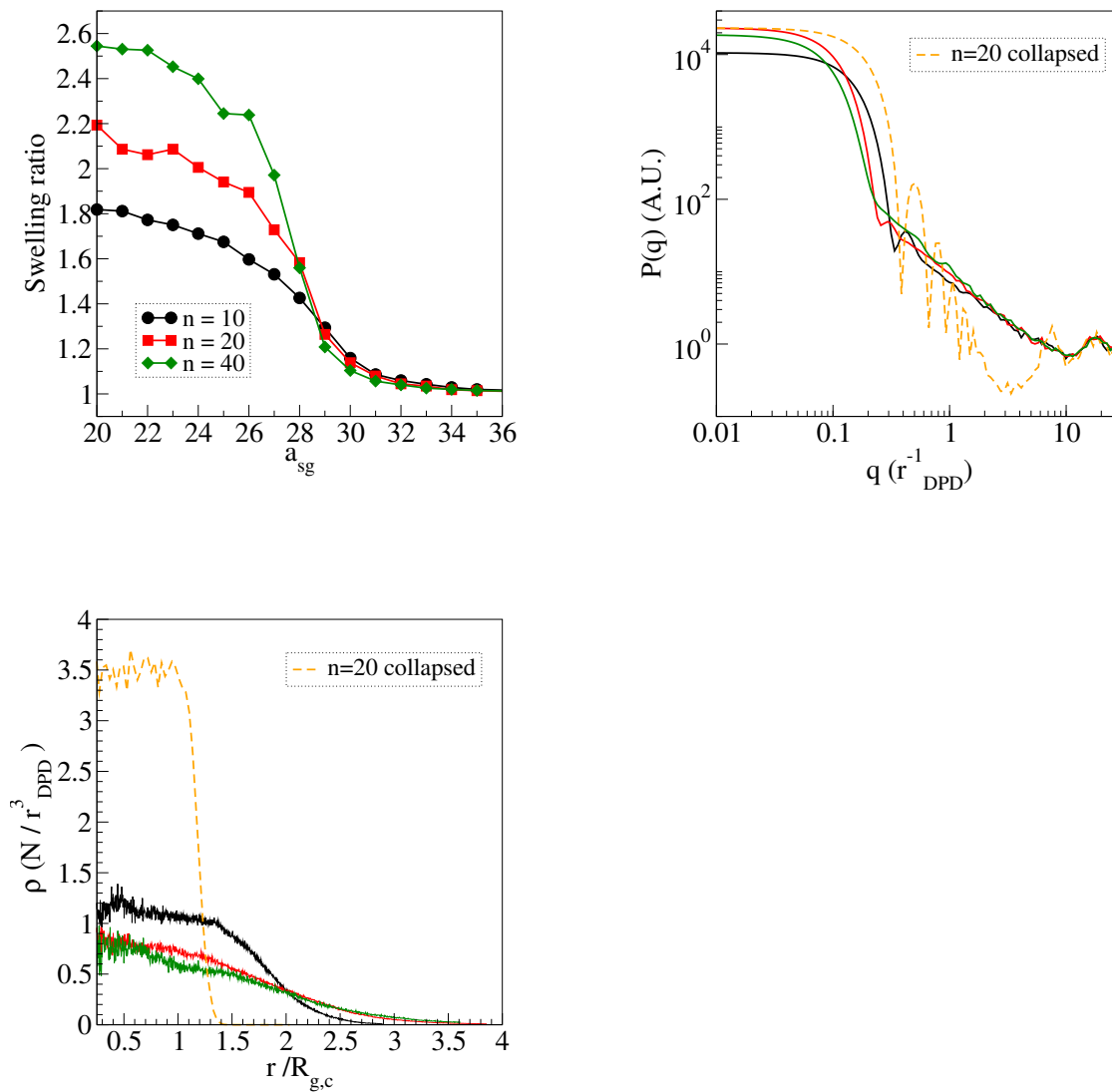
Figure 42: Swelling transition curves(top left), structure factors (top right) and radial density profiles in good solvent(bottom) of n=10,20 and 40 end-crosslinked nanogel beads. The form factor and radial density of the n=20 nanogel in the collapsed state are also shown as a dashed line.

Table 10: Topological characterization polymer networks obtained for different initial chain lengths. The elastically inactive defects (1-defects) and loops are expressed as a percent ratio with respect to the initial chains. $\langle N \rangle$ is the number of beads per strand and $\langle Z \rangle$ is the number of kinks per chain.

System	CL density	CL functionality	1-defects	2-loops	3-loops	4-loops	$\langle N \rangle$	$\langle Z \rangle$
10	5.3 %	2.775	9.25 %	2.75 %	2.77 %	2.90%	11.32	0.034
20	3.02%	2.71	12.92 %	2.80 %	2.02 %	2.60%	21.35	0.152
40	1.14 %	2.63	18.10 %	1.50%	1.65 %	1.40%	41.35	0.464

that the probability for two ends of the same chain to find themselves in the same point is reduced as the chain length increases. As for the entanglements, the network formation freezes the pre-existent state and changes the melt entanglement state only slightly, even if a significant increase has been observed for the very short n=10 chains.

5.3.2   Comparison of in silico nanogel synthesis techniques

Since there are several ways to perform the in silico synthesis of the nanogel, it is important to consider how such a choice could alter the calculated quantities of the simulated system. In figure 43 the swelling curves, structure factors and radial density profiles are reported for three possible ways to obtain nanogel beads from a n=20 precursor melt:

- (random-made) Cl points are randomly joined with linear chains,

- (confinement-made) or by letting the melt self-assemble in a confined region,

- (cut) letting the melt self-assemble under periodic conditions, and cut the nanogel afterwards.

The random-made nanogels show the lowest swelling ratio and the highest density in the swollen state. By contrast, both of the reaction based nanogels allow for larger swollen sizes, the cut one being the largest, and practically equal densities for $r/R_{g,c} < 1.5$. The main difference between the two is actually the skin layer, which is wider and less defined in the cut nanogel. The form factor reflects these differences, with a more compact structure found for the random-made nanogel, with the first peak more visible and shifted at larger q, while the other beads show qualitatively the same $P(q)$.

By looking at table 11, it can be observed that the nanogel made under confinement has a higher CL density and functionality. It is then natural to expect, as observed, a lower swelling ratio. In what concerns

Figure 43: Radial density profiles (top left), form factors (top right) and swelling transition curves (bottom) of n=20 nanogel beads obtained with three different *in silico* methods.

Table 11: Topological characterization of networks made from a n=20 chain melt, using different *in silico* methods. The elastically inactive defects (1-defects) and n-loops are expressed as a percent ratio with re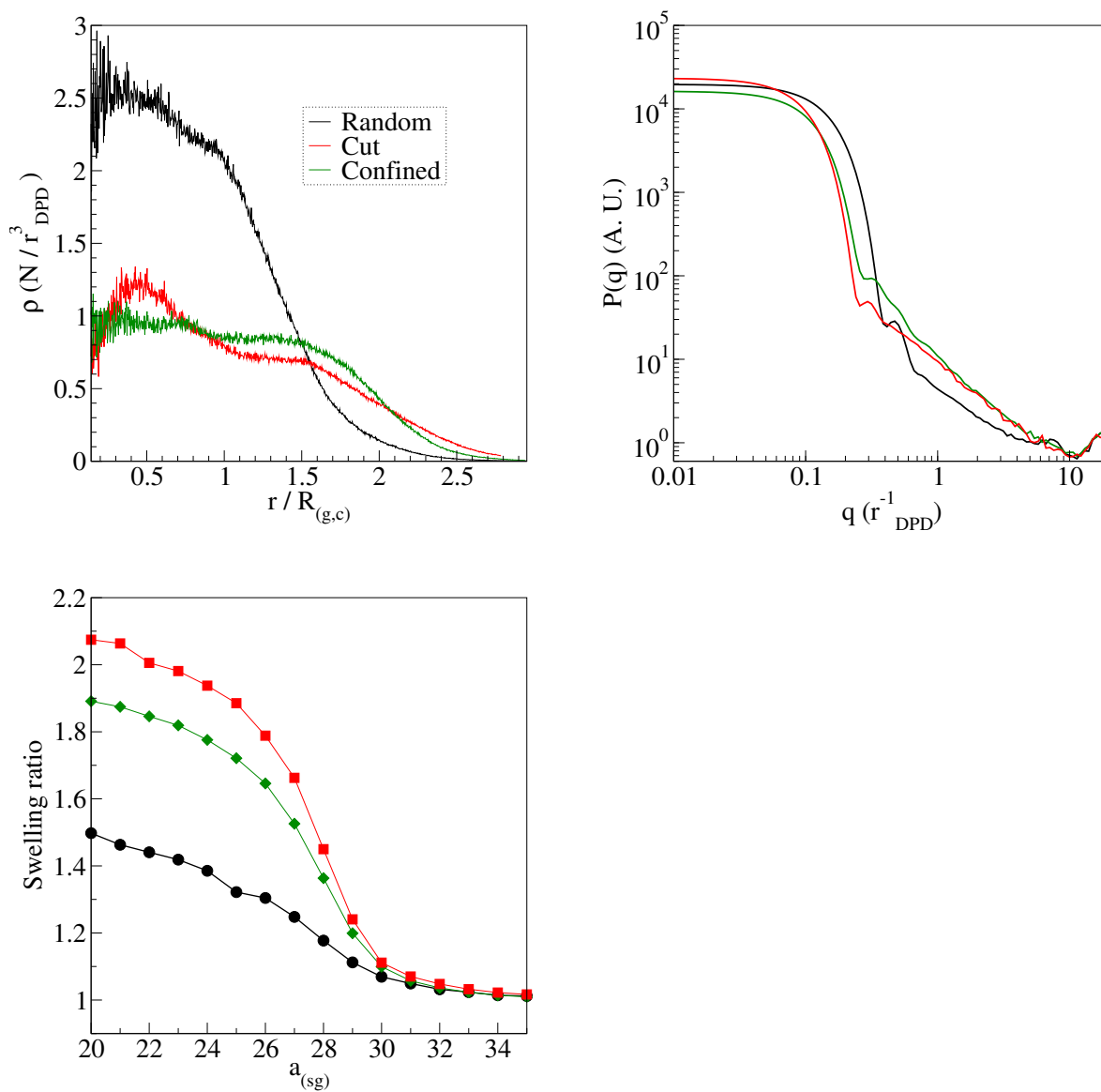spect to the initial chains. $\langle N \rangle$ is the number of beads per strand and $\langle Z \rangle$ is the number of kinks per chain. The first row, already appeared in table 10, is reported here for comparison.

System	CL density	CL functionality	1-Defects	2-loops	3-loops	4-loops	$\langle N \rangle$	$\langle Z \rangle$
20 cut	3.02%	2.71	12.92 %	2.80 %	2.02 %	2.60%	21.35	0.152
20 confined	3.08 %	3.0	17.32%	2.24 %	0.342%	5.43%	21.34	0.094
20 random	1.73%	2.12	4.86%	0.02 %	0	0	21.08	0.568

topology, the confinement-made network has a lower value of $\langle Z \rangle$ when compared to periodic networks, this a being a surface effect. At the same time, the number of elastically inactive defects is slightly larger.

When checking the random-made network, a much lower CL density and functionality is found, although the number of elastically inactive defects is sensibly lower and the higher order loops are virtually inexistent. On the other hand, a much larger $\langle Z \rangle$ is found for them, indicating that random-made networks are much more entangled than the others. This seem contradictory, since a poor CL density suggests larger swelling ratios, while greater $\langle Z \rangle$ suggests the opposite. However, there is also another aspect that should be considered. Due to the formation process, the random-made network is mainly constituted by stretched chains subject to an entropic elastic force which acts to contract them, thereby opposing and hindering any solvent-induced swelling. This can be easily revealed by calculating the MSID for the unreacted N=20 melt and the different networks, reported in figure 44. While the reaction-based network formation results in final structure with chains still having a internal distance distribution very close to that of the precursor melt, the random-made network MSID present a significant deviation, meaning that the chains are overstretched.

5.3.3   Comparison of reaction routes

End-crosslinked nanogels have been compared with those obtained through a more traditional crosslinking technique, in which the end-reactive chains covalently bonds to poly-functional CL small molecules, as sketched in the top left panel of figure 45. Stoichiometric mixtures of trifunctional cross-linkers were mixed to n=16 precursor chains, the ends of which could react with a probability coefficient of 0.4 with the functional CL beads. In this way, network strands would have the same length as for the end-crosslinking case. Two different cross-linker formulations were used: one fully made of trifunctional crosslinker and a
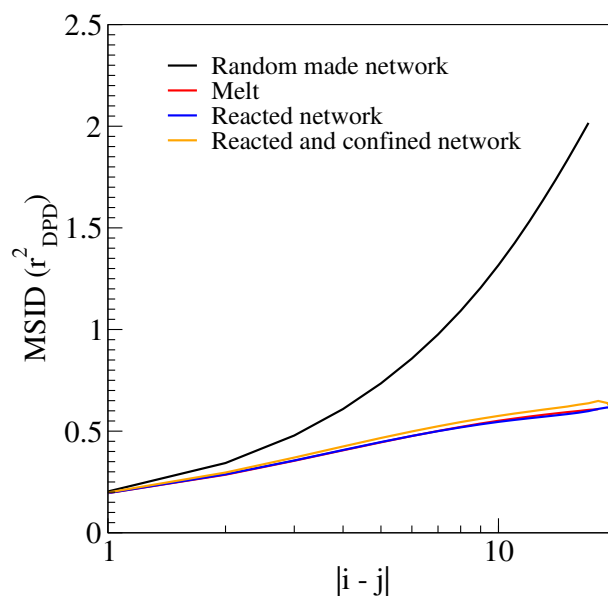
Figure 44: Mean squared internal distance for unreacted n=20 melt, and corresponding networks obtained with different methods and conditions.

more realistic one, containing a 30 % weight ratio of 4-functional impurities. This reflects the fact that a certain degrees of higher functionality impurities is always present in commercial isocyanurate products. Since only a one-step process is considered this time, the reaction speed is significantly faster, and fully formed network can be reached in only 5000 iterations.

All nanogel beads were cut from a periodic network of n=20 chains and contained roughly 10000 beads. During equilibration and network formation, the mixtures always appeared well mixed and no phase separation was observed.

Figure 45 reports the form factors, swelling ratios and radial density profiles at $a_{sg} = 25$, for polymer networks obtained in three different ways, the properties of which are summarized in table 12. For the impure mixture, the stoichiometric ratio between chain and crosslinker ends is not exactly matched, hence lower products are expected.

The structure factor is not revealing significant differences between the differently processed nanogels. However, the end-functionalized ones exhibit slightly larger swelling ratios and lower radial densities, whereas pure and impure chain-crosslinker made nanogels exhibit very similar swelling ratios. Therefore, the two synthesis methods provide negligible differences in terms of swelling properties and also in averaged strand and loop lengths. The enhanced swelling of the end-crosslinked nanogels is related to the lower
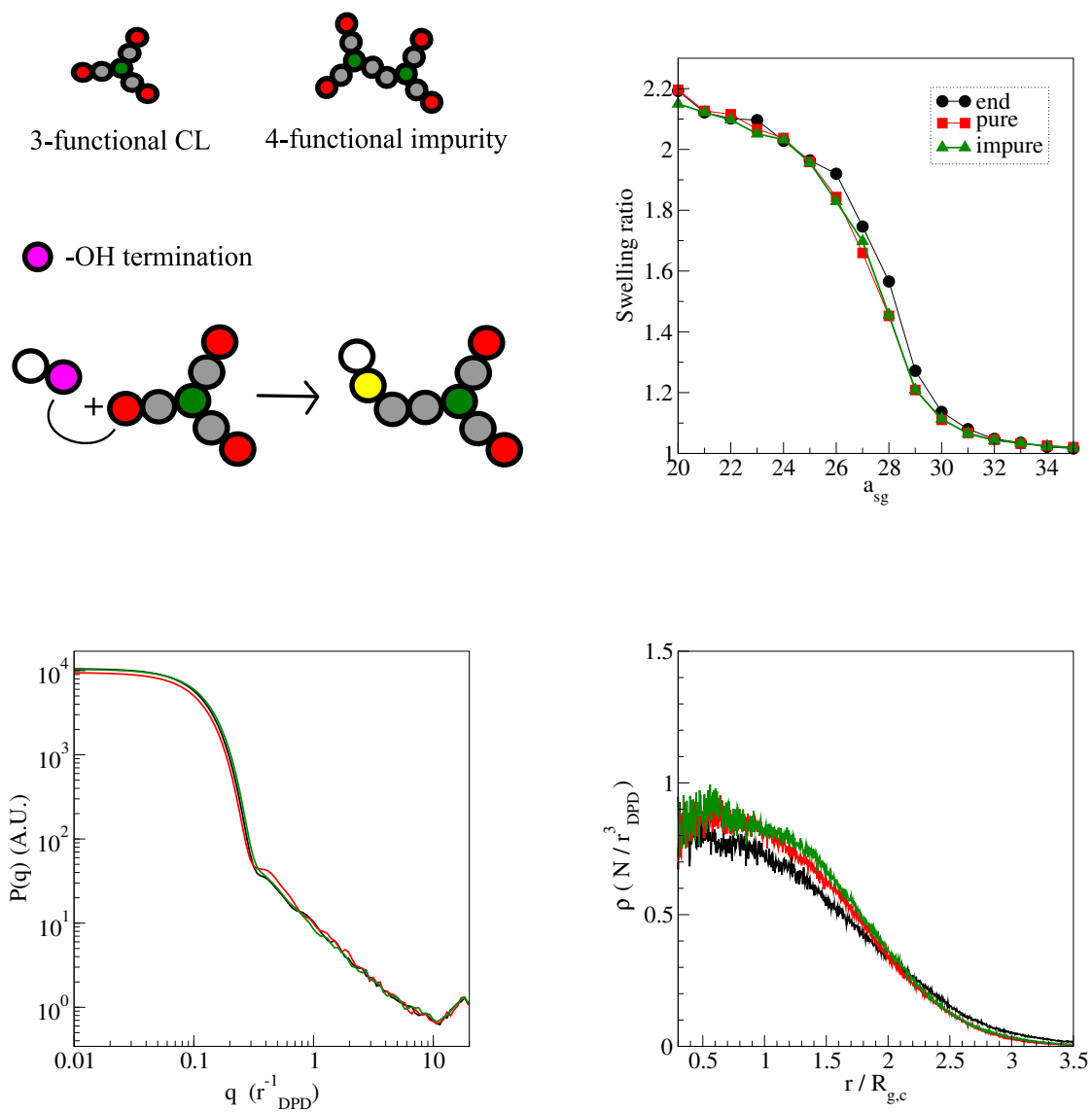
Figure 45: The structure of the crosslinking molecules and schematics of the alternative reaction scheme are in the top left panel. The colour legend is the same as in figure 38. Swelling curves (top right), form factors (bottom left) and radial density profiles (bottom right) in good solvent conditions are also reported for the nanogels obtained considering different chemical routes and crosslinker purity level.

overall content of crosslinking beads.

Interestingly, the presence of impurities in the crosslinker composition seem not to impact significantly the swelling ratios. This is expected as the lower number of bonds due to the stoichiometric impairment is compensated by the presence of effective 4-functional CL beads, tightening the structure, as reflected by the smaller average chain length $\langle N \rangle$. In terms of defects, it is interesting to observe that the mixing approach significantly reduced their occurrence. The number of kinks per chain is also larger for the system containing impurities.

Table 12:   Comparison of topological properties of n=20 networks obtained with different chemical routes. The elastically inactive defects(1-defects) and 2-loops are expressed as a percent ratio with respect to the initial chains. $\langle N \rangle$ is the number of beads per strand and $\langle Z \rangle$ is the number of kinks per chain. The first row, already seen in table 10, is reported here for comparison.

System	CL density	CL functionality	1-defects	2-loops	3-loops	4-loops	$\langle N \rangle$	$\langle Z \rangle$
end-crosslinked	3.02%	2.71	12.92 %	2.80 %	2.02 %	2.60%	21.35	0.152
pure-mix	3.5 %	3.00	12.51 %	2.04%	2.68%	2.18%	21.44	0.174
impure-mix	3.7 %	3.00	12.77%	2.24%	2.70%	2.60%	19.92	0.183

This comparison is useful to assess the effectiveness of an end-crosslinking reaction. Since no phase separation was observed in the 2-component precursor melts, their final network structures are very close to an ideal realization, especially when pure trifunctional crosslinkers are employed. Therefore, having found very similar results with end-crosslinked structures confirms that very well-structured networks can be easily obtained through this technique. This represents a clear advantage because this process, apart form catalyst and solvent, involves only one component.

5.3.4   Effect of explicit solvent inclusion

In real systems, crosslinking processes commonly take place in solvated environments, hence it is important to consider how explicit solvent inclusion during the network formation process can influence the computational predictions. Different solvation levels, from 0 to 66 %, were considered during the network assembly of $n = 10$ chains, from which nanogels containing about 13000 beads were cut. It is expected that the end-crosslinking reaction would be slower due to reduced reactant concentration. This is indeed the case, as it can be observed in figure 46, where the CL bead formation speed decreases as the solvent concentration increases.

Table 13: Topological characterization of networks made from a n=10 chain melt, under the presence of solvent at different weight ratios during their formation. The elastically inactive defects (1-loops) and n-loops are expressed as a percent ratio with respect to the initial chains. $\langle N \rangle$ is the number of beads per strand and $\langle Z \rangle$ is the number of kinks per chain.

Solvent %	CL density	CL functionality	1-defects	2-loops	3-loop	4-loops	$\langle N \rangle$	$\langle Z \rangle$
0	5.33 %	2.775 %	9.25 %	2.75 %	2.77 %	2.90%	11.325	0.034
33	5.66 %	2.84 %	16.35%	3.60 %	3.22%	3.10%	11.304	0.010
50	5.60 %	2.86 %	19.50%	4.80 %	3.37 %	3.90 %	11.271	0.004
60	5.64 %	2.86 %	21.35 %	5.80 %	4.05 %	4.60%	11.273	0.002
66	5.77%	2.87 %	29.92%	6.70 %	2.23 %	3.90%	11.281	0.001

In addition, the explicit solvent inclusion produces a sensible increase of the nanogel swelling in good solvent even though, as shown in table 13, the CL concentrations and functionality are very similar for all the solvent percentages. This increased swelling ratio is due to two key factors. From one side, as the solvent percentage increases, so does the incidence of elastically inactive defects and 2-loops. This can be understood considering that the solvent presence decreases the overall chain density, thereby reducing the probability of two chain ends from different chains to come in close contact and react.

Moreover, as can be appreciated by the $\langle Z \rangle$ values, the number of kinks per chain is decreasing as solvent is added. Clearly, this effect is expected to be more significant for longer chains, as the n=10 presented here are almost unentangled, and the probability of forming tadpoles decreases with the chain length.

The addition of solvent has thus a strong effect on the simulated networks, dramatically changing their topology and, by consequence, their macroscopic properties.

5.4   Conclusions

In this chapter, the assembly of isocyanurate-crosslinked networks from end-functionalized chains has been investigated by using a bead-spring polymer model in conjunction with a scheme for the chemical crosslinking reaction and dissipative particle dynamics simulation with MD-derived parameters.

Realistic nanogels with the typical core-corona structure and the swelling transition were obtained, equivalent to those made from ideal prepolymer-crosslinker mixtures. It is worth noting that the techniques
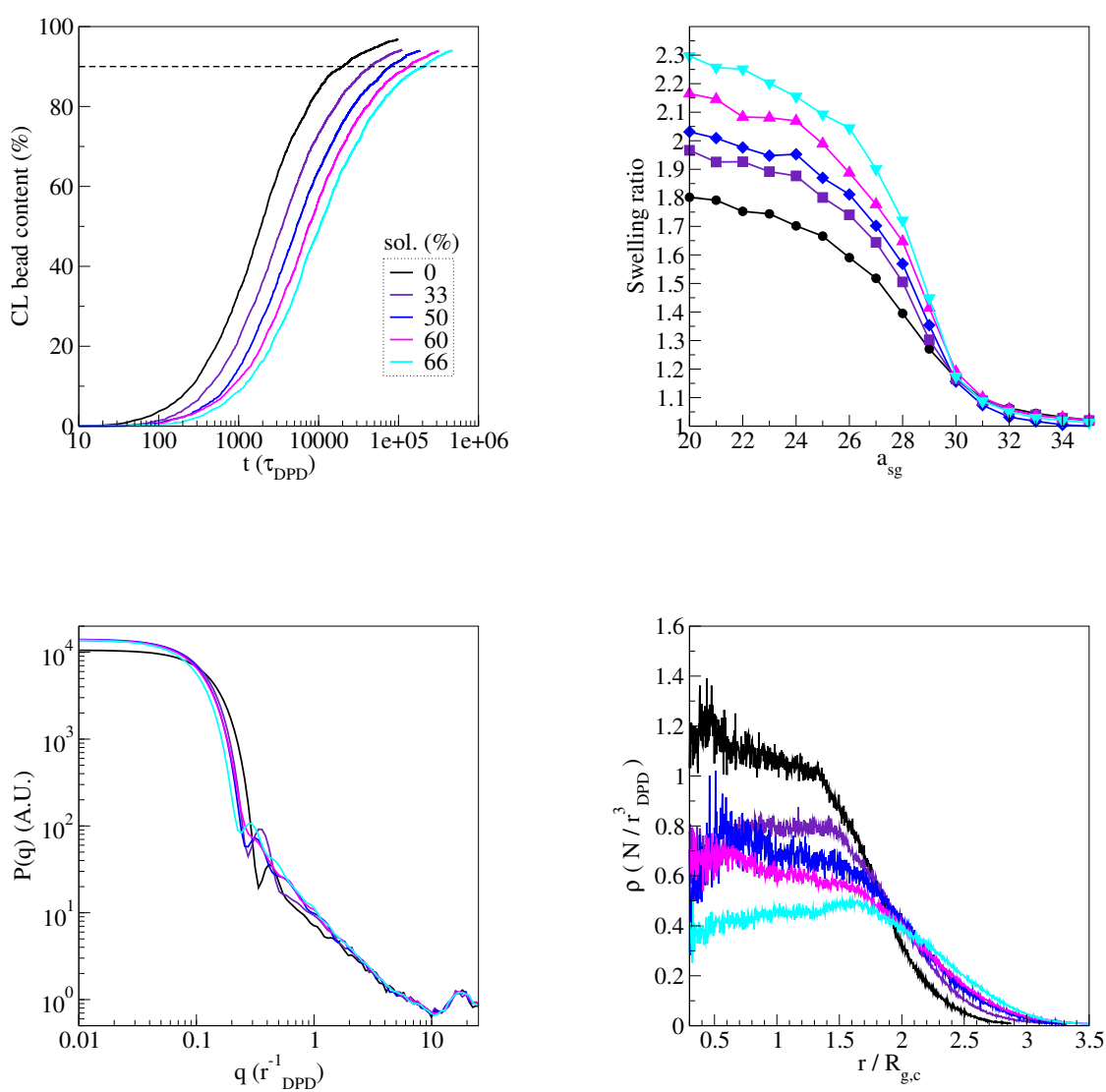
Figure 46: Reaction rates(top left), swelling curves (top right), form factors (bottom left) and radial density profiles (bottom right) in good solvent conditions of n=10 nanogels obtained at different solvation ratios during the network formation phase.

employed in this chapter can be used as well for any isocyanurate-crosslinked material, and the reaction scheme can be easily modified to take into account more complex chemical networks.

Concerning the nanogel properties, it was shown that their swelling ratios are strongly dependent not only the precursor features, such as chain length, but also on the processing route -or simulation design- chosen. Indeed, from the same precursor, it was possible to make nanogels with a dramatically different swelling behaviour, demonstrating that the *in silico* techniques tested here are inequivalent, and the choice upon which one to employ should be made in an informed way. Moreover, apart from the swelling differences, the networks also look structurally different, with degrees of entanglement and concentration of defects.

Nanogel swelling ratios and, by extension, network elastic properties are indeed intimately connected with topological features, in particular with chain entanglement and elastically inactive defects, as shown through their inspection and primitive path analysis. As it is made clear in the solvation study, these two factors are both affecting the final network properties, with less-entangled and more defected networks obtained as the solvent content is increased during the production.

Clearly, the model can be improved in several ways, for instance by introducing extra interaction terms for specific interactions [96, 97], but it is remarkable that it is already capable to capture most of the relevant features of network dynamical properties.

Chapter 6

Conclusions and perspectives

This thesis expanded the level of knowledge on isocyanate and isocyanurates, providing at the same time effective tools for their simulation in all their manifestations, from precursor molecules to crosslinked materials. However the topic is far from being complete, and still offers many possibilities for further research, outlined below.

The optimized MD force field GAFF-IC allows for very accurate predictions of densities, enthalpies of vaporization and viscosities of many aliphatic isocyanate and isocyanurate systems, with an impressive improvement with respect to the previously available parametrization. This permitted the comprehensive simulation study capable of highlighting the complex relationships between, on one side, structure and composition at the molecular scale and, on the other, macroscopic observables.

GAFF-IC is specifically targeted at aliphatic isocyanates and there are two main areas of extension. Firstly, It should be integrated into a wider environment where common solvents used for isocyanates are included, as well as carbamates and ureas, found in isocyanate-derived materials. This way, a classical and reliable all-atom representation would be available not only for isocyanate precursors, but also for the final materials. Secondly, the optimized force-field should include as well other families, such as the aromatic isocyanates, most used in industrial processes. In both cases, it will be very beneficial considering a larger experimental data set for the force-field optimization, including for instance studies on their phase transitions and characterization of mixtures.

Ab initio, DFT methods were employed to investigate the nature of isocyanate-isocyanurate interactions in vacuum conditions, and the role of the isocyanurate ring as a strong dispersion force site has been demonstrated. In this regard isocyanurate-isocyanate interactions were revealed, and further GAFF-IC MD simulations provided strong evidence of them being the main responsible for the high viscosities encountered in polyisocyanate liquids.

The *ab initio* calculations on isocyanates and their derivatives should be expanded with different methods and, when available, higher accuracy calculations to provide a reference for further studies and fill the scarceness of calculations for these molecules. Such knowledge would be beneficial not only for investigating isocyanates in common processing conditions, but also in more extreme environments, such as those of astrophysical interest.

The geometry and strong dispersion interaction of isocyanurates makes them appealing for non-covalent functionalization of 2D materials, and this possibility was investigated through a study on the adsorption energies of these molecules on graphene and fluorographene, boron and carbon nitride. The self-assembly of isocyanurate monolayers on graphene under certain conditions has been demonstrated, as well as their stability upon solvation.

In this aspect, the presented results are promising and further studies, possibly in conjunction with specifically designed experiments, are required to assess the effectiveness and actual feasibility of non the proposed non-covalent functionalization, in view of the synthesis of 'smart' crosslinked materials, such as networks and coatings.

Isocyanate-crosslinked networks and nanogels were simulated using DPD methods coupled with a chemical reaction modelling. This simulation scheme reproduced all the expected behaviours in terms of swelling and allowed to investigate the networks obtained under different conditions. A marked dependence of the network properties upon the processing parameters and simulation scheme adopted was found and characterized in terms of the networks' topology.

Although the DPD approach revealed itself very effective in characterizing the swelling properties of these networks, the proposed model can be certainly improved including specific terms to describe urethane bonds and take into account the isocyanate-isocyanurate interactions. More generally, it will be useful to compare the DPD results with other coarse-grained approaches, for which specific force-field are yet to be developed. Such task has to consider reliable all-atom simulations as a starting point, therefore the GAFF-IC forcefield is the natural choice for this.

Bibliography

[1] A. Wurtz, Recherches sur les Éthers cyaniques et leurs dérivés, Comptes Rendu Chimie 27 (1848) 241–243.

[2] O. Bayer, Das di-isocyanat-polyadditionsverfahren (polyurethane), Angewandte Chemie 59 (9) (1947) 257–272. doi:10.1002/ange.19470590901.
URL http://dx.doi.org/10.1002/ange.19470590901

[3] F. E. Golling, R. Pires, A. Hecking, J. Weikard, F. Richter, K. Danielmeier, D. Dijkstra, Polyurethanes for coatings and adhesives – chemistry and applications, Polymer International (2018). doi:10.1002/pi.5665.
URL https://onlinelibrary.wiley.com/doi/abs/10.1002/pi.5665

[4] E. Delebecq, J.-P. Pascault, B. Boutevin, F. Ganachaud, On the versatility of urethane/urea bonds: Reversibility, blocked isocyanate, and non-isocyanate polyurethane, Chemical Reviews 113 (1) (2013) 80–118. doi:10.1021/cr300195n.
URL http://dx.doi.org/10.1021/cr300195n

[5] S. L. Cooper, J. Guan (Eds.), Advances in Polyurethane Biomaterials, Woodhead Publishing, 2016.

[6] Foam and cork insulation protects deep space rocket from fire and ice.
URL https://cutt.ly/ye14SkW

[7] Global isocyanate market - trends, drivers, challenges, and vendor analysis - technavio (2019).
URL https://www.businesswire.com/news/home/20180127005005/en/Global-Isocyanate-Market---Trends-Drivers-Challenges

[8] M. F. Sonnenschein, Polyurethanes, Science, Technology, Markets, and Trends, John Wiley and Sons, Hoboken, NJ, USA, 2015.

[9] D. Heift, Z. Benko, H. Grutzmacher, A. R. Jupp, J. M. Goicoechea, Cyclo-oligomerization of isocyanates with na(ph2) or na(ocp) as "p-" anion sources, Chemical Science 6 (2015) 4017–4024. doi:10.1039/C5SC00963D.
URL http://dx.doi.org/10.1039/C5SC00963D

[10] P. J. Driest, V. Lenzi, L. Marques, M. M. D. Ramos, D. J. Dijkstra, F. U. Richter, D. Statamatialis, D. W. Grijpma, Aliphatic isocyanurate and polyisocyanate networks, Polymers for advanced technologies 28 (10) (2017) 1299–1304. doi:10.1002/pat.3891.
URL http://dx.doi.org/10.1002/pat.3891

[11] D. Chattopadhyay, K. Raju, Structural engineering of polyurethane coatings for high performance applications, Progress in Polymer Science 32 (3) (2007) 352 – 418. doi:10.1016/j.progpolymsci.2006.05.003.
URL http://www.sciencedirect.com/science/article/pii/S0079670006001365

[12] M. Moritsugu, A. Sudo, T. Endo, Cyclotrimerization of diisocyanates toward high-performance networked polymers with rigid isocyanurate structure: Combination of aromatic and aliphatic diisocyanates for tunable flexibility, Journal of Polymer Science Part A: Polymer Chemistry 51 (12) (2013) 2631–2637. doi:10.1002/pola.26651.
URL http://dx.doi.org/10.1002/pola.26651

[13] H. Renz, B. Bruchmann, Pathways targeting solvent-free {PUR} coatings, Progress in Organic Coatings 43 (1–3) (2001) 32 – 40. doi:10.1016/S0300-9440(01)00239-9.
URL http://www.sciencedirect.com/science/article/pii/S0300944001002399

[14] E. Preis, N. Schindler, S. Adrian, U. Scherf, Microporous polymer networks made by cyclotrimerization of commercial, aromatic diisocyanates, ACS Macro Letters 4 (11) (2015) 1268–1272. doi:10.1021/acsmacrolett.5b00726.
URL http://dx.doi.org/10.1021/acsmacrolett.5b00726

[15] S. Donthula, C. Mandal, T. Leventis, J. Schisler, A. M. Saeed, C. Sotiriou-Leventis, N. Leventis, Shape memory superelastic poly(isocyanurate-urethane) aerogels (pir-pur) for deployable panels and biomimetic applications, Chemistry of Materials 29 (10) (2017) 4461–4477. doi:10.1021/acs.chemmater.7b01020.
URL http://dx.doi.org/10.1021/acs.chemmater.7b01020

[16] F. Borbone, A. Carella, A. Roviello, M. Casalboni, F. De Matteis, G. Stracci, F. Della Rovere, A. Evangelisti, M. Dispenza, Outstanding poling stability of a new cross-linked nonlinear optical (NLO) material from a low molecular weight chromophore, Journal of Physical Chemistry B 115 (42) (2011) 11993–12000. doi:10.1021/jp204545k.

[17] J. Konieczny, K. Loos, Polyurethane coatings based on renewable white dextrins and isocyanate trimers, Macromolecular Rapid Communications 40 (10) (2019) 1800874. doi:10.1002/marc.201800874.
URL https://onlinelibrary.wiley.com/doi/abs/10.1002/marc.201800874

[18] S. Sahoo, H. Kalita, S. Mohanty, S. K. Nayak, Synthesis and characterization of vegetable oil based polyurethane derived from low viscous bio aliphatic isocyanate: Adhesion strenghth to to wood-wood substrate bonding, Macromolecular Research 25 (8) (2017) 772–778. doi:10.1007/s13233-017-5080-2.
URL https://doi.org/10.1007/s13233-017-5080-2

[19] G. Behnken, A. Hecking, B. V. Sánchez, High performance enabled by nature, European Coatings Journal 1 (2016) 46–50.

[20] H. R. Sharpe, A. M. Geer, H. E. L. Williams, T. J. Blundell, W. Lewis, A. J. Blake, D. L. Kays, Cyclotrimerisation of isocyanates catalysed by low-coordinate mn(ii) and fe(ii) m-terphenyl complexes, Chem. Commun. 53 (2017) 937–940. doi:10.1039/C6CC07243G.
URL http://dx.doi.org/10.1039/C6CC07243G

[21] M. A. Bahili, E. C. Stokes, R. C. Amesbury, D. M. C. Ould, B. Christo, R. J. Horne, B. M. Kariuki, J. A. Stewart, R. L. Taylor, P. A. Williams, M. D. Jones, K. D. M. Harris, B. D. Ward, Aluminium-catalysed isocyanate trimerization, enhanced by exploiting a dynamic coordination sphere, Chem. Commun. 55 (2019) 7679–7682. doi:10.1039/C9CC03339D.
URL http://dx.doi.org/10.1039/C9CC03339D

[22] Z. Guo, Y. Wang, J. Yang, X. Wei, Lithium complex of 2-amino-functionalized benzoylpyrrole: Synthesis, structure, and catalytic activity for the cyclotrimerization of isocyanates, Polyhedron 130 (2017) 13 – 17. doi:https://doi.org/10.1016/j.poly.2017.03.058.
URL http://www.sciencedirect.com/science/article/pii/S0277538717302565

[23] Z. Guo, Y. Xu, X. Wu, X. Wei, C. Xi, Potassium complexes containing bidentate pyrrole ligands: synthesis, structures, and catalytic activity for the cyclotrimerization of isocyanates, Dalton Trans. 48 (2019) 8116–8121. doi:10.1039/C9DT01246J.
URL http://dx.doi.org/10.1039/C9DT01246J

[24] C. Li, W. Zhao, J. He, Y. Zhang, Highly efficient cyclotrimerization of isocyanates using n-heterocyclic olefins under bulk conditions, Chem. Commun. (2019) –doi:10.1039/C9CC06402H.
URL http://dx.doi.org/10.1039/C9CC06402H

[25] J. A. Howarter, J. P. Youngblood, Self-cleaning and anti-fog surfaces via stimuli-responsive polymer brushes, Advanced Materials 19 (22) (2007) 3838–3843. doi:10.1002/adma.200700156.
URL http://dx.doi.org/10.1002/adma.200700156

[26] A. R. McDonald, H. P. Dijkstra, B. M. J. M. Suijkerbuijk, G. P. M. van Klink, G. van Koten, "click" immobilization of organometallic pincer catalysts for c-c coupling reactions, Organometallics 28 (16) (2009) 4689–4699. doi:10.1021/om900237g.
URL http://dx.doi.org/10.1021/om900237g

[27] S. Kuypers, S. K. Pramanik, L. D'Olieslaeger, G. Reekmans, M. Peters, J. D'Haen, D. Vanderzande, T. Junkers, P. Adriaensens, A. Ethirajan, Interfacial thiol-isocyanate reactions for functional nanocarriers: a facile route towards tunable morphologies and hydrophilic payload encapsulation, Chemical Communications 51 (2015) 15858–15861. doi:10.1039/C5CC05258K.
URL http://dx.doi.org/10.1039/C5CC05258K

[28] H.-J. Kang, E. J. Cha, H.-D. Park, Protein immobilization onto various surfaces using a polymer-bound isocyanate, Applied Surface Science 324 (Supplement C) (2015) 198 – 204. doi:10.1016/j.apsusc.2014.10.117.
URL http://www.sciencedirect.com/science/article/pii/S0169433214023605

[29] H. Abushammala, J. Mao, A review of the surface modification of cellulose and nanocellulose using aliphatic and aromatic mono- and di-isocyanates, Molecules 24 (15) (2019). doi:10.3390/molecules24152782.
URL https://www.mdpi.com/1420-3049/24/15/2782

[30] Y. Liu, Y. Qin, Z. Peng, J. Zhou, C. Wan, D. Wang, Hexamethylene diisocyanate as an electrolyte additive for high-energy density lithium ion batteries, J. Mater. Chem. A 3 (2015) 8246–8249. doi:10.1039/C4TA07055K.
URL http://dx.doi.org/10.1039/C4TA07055K

[31] X. Xu, Y. Qin, W. Yang, D. Sun, Y. Liu, B. Guo, D. Wang, Influence of hdi as a cathode film-forming additive on the performance of life0.2mn0.8po4/c cathode, RSC Adv. 7 (2017) 41970–41972. doi:10.1039/C7RA04979J.
URL http://dx.doi.org/10.1039/C7RA04979J

[32] D. Sun, Q. Wang, J. Zhou, Y. Lyu, Y. Liu, B. Guo, Forming a stable cei layer on lini0.5mn1.5o4 cathode by the synergy effect of fec and hdi, Journal of The Electrochemical Society 165 (10)

(2018) A2032–A2036. doi:10.1149/2.0211810jes.
URL http://jes.ecsdl.org/content/165/10/A2032.abstract

[33] R. M. Hensarling, S. B. Rahane, A. P. LeBlanc, B. J. Sparks, E. M. White, J. Locklin, D. L. Patton, Thiol-isocyanate "click" reactions: rapid development of functional polymeric surfaces, Polymer Chemistry 2 (2011) 88–90. doi:10.1039/C0PY00292E.
URL http://dx.doi.org/10.1039/C0PY00292E

[34] R. M. Arnold, D. L. Patton, V. V. Popik, J. Locklin, A dynamic duo: Pairing click chemistry and postpolymerization modification to design complex surfaces, Accounts of Chemical Research 47 (10) (2014) 2999–3008. doi:10.1021/ar500191m.
URL http://dx.doi.org/10.1021/ar500191m

[35] M. Huo, N. Wang, T. Fang, M. Sun, Y. Wei, J. Yuan, Single-chain polymer nanoparticles: Mimic the proteins, Polymer (United Kingdom) 66 (2015) A11–A21. doi:10.1016/j.polymer.2015.04.011.
URL http://dx.doi.org/10.1016/j.polymer.2015.04.011

[36] S. Stankovich, R. D. Piner, S. B. T. Nguyen, R. S. Ruoff, Synthesis and exfoliation of isocyanate-treated graphene oxide nanoplatelets, Carbon 44 (15) (2006) 3342–3347. doi:10.1016/j.carbon.2006.06.004.
URL https://doi.org/10.1016/j.carbon.2006.06.004"

[37] A. Kafy, K. K. Sadasivuni, H.-C. Kim, A. Akther, J. Kim, Designing flexible energy and memory storage materials using cellulose modified graphene oxide nanocomposites, Physical Chemistry Chemical Physics 17 (8) (2015) 5923–5931. doi:10.1039/C4CP05921B.
URL http://xlink.rsc.org/?DOI=C4CP05921B

[38] M. Dekamin, F. Mehdipoor, A. Yaghoubi, 1,3,5-Tris(2-hydroxyethyl)isocyanurate functionalized graphene oxide: A novel and efficient nanocatalyst for the one-pot synthesis of 3,4-dihydropyrimidin-2(1: H)-ones, New Journal of Chemistry 41 (14) (2017) 6893–6901. doi:10.1039/c7nj00632b.
URL http://dx.doi.org/10.1039/C7NJ00632B

[39] J. Li, F. Wang, C. yan Liu, Tri-isocyanate reinforced graphene aerogel and its use for crude oil adsorption, Journal of Colloid and Interface Science 382 (1) (2012) 13 – 16. doi:https://doi.org/10.1016/j.jcis.2012.05.040.
URL http://www.sciencedirect.com/science/article/pii/S002197971200584X

[40] S.-h. Hsu, K.-C. Hung, Y.-Y. Lin, C.-H. Su, H.-Y. Yeh, U.-S. Jeng, C.-Y. Lu, S. A. Dai, W.-E. Fu, J.-C. Lin, Water-based synthesis and processing of novel biodegradable elastomers for medical applications, J. Mater. Chem. B 2 (2014) 5083–5092. doi:10.1039/C4TB00572D.
URL http://dx.doi.org/10.1039/C4TB00572D

[41] P. J. Driest, D. J. Dijkstra, D. Stamatialis, D. W. Grijpma, The trimerization of isocyanate-functionalized prepolymers: An effective method for synthesizing well-defined polymer networks, Macromolecular Rapid Communications 40 (9) (2019) 1800867. doi:10.1002/marc.201800867.
URL https://onlinelibrary.wiley.com/doi/abs/10.1002/marc.201800867

[42] A. Fernandez-Nieves, H. M. Wyss, J. Mattsson, D. A. Weitz (Eds.), Microgel Suspensions: Fundamentals and Applications, Wiley-VCH, Weinheim, Germany, 2011.

[43] P. Grossen, D. Witzigmann, S. Sieber, J. Huwyler, Peg-pcl-based nanomedicines: A biodegradable drug delivery system and its application, Journal of Controlled Release 260 (2017) 46 – 60. doi:https://doi.org/10.1016/j.jconrel.2017.05.028.
URL http://www.sciencedirect.com/science/article/pii/S0168365917306004

[44] L. P. Fonseca, R. B. Trinca, M. I. Felisberti, Amphiphilic polyurethane hydrogels as smart carriers for acidic hydrophobic drugs, International Journal of Pharmaceutics 546 (1) (2018) 106 – 114. doi:https://doi.org/10.1016/j.ijpharm.2018.05.034.
URL http://www.sciencedirect.com/science/article/pii/S0378517318303429

[45] Y.-P. Chen, S.-h. Hsu, Preparation and characterization of novel water-based biodegradable polyurethane nanoparticles encapsulating superparamagnetic iron oxide and hydrophobic drugs, J. Mater. Chem. B 2 (2014) 3391–3401. doi:10.1039/C4TB00069B.
URL http://dx.doi.org/10.1039/C4TB00069B

[46] R. Liu, Q. Zhang, Q. Zhou, P. Zhang, H. Dai, Nondegradable magnetic poly (carbonate urethane) microspheres with good shape memory as a proposed material for vascular embolization, Journal of the Mechanical Behavior of Biomedical Materials 82 (2018) 9 – 17. doi:https://doi.org/10.1016/j.jmbbm.2018.02.010.
URL http://www.sciencedirect.com/science/article/pii/S1751616118301036

[47] A. C. Weems, W. Li, D. J. Maitland, L. M. Calle, Polyurethane microparticles for stimuli response and reduced oxidative degradation in highly porous shape memory polymers, ACS Applied Materials & Interfaces 10 (39) (2018) 32998–33009, pMID: 30184426. doi:10.1021/acsami.8b11082.
URL https://doi.org/10.1021/acsami.8b11082

[48] J. Yang, M. W. Keller, J. S. Moore, S. R. White, N. R. Sottos, Microencapsulation of isocyanates for self-healing polymers, Macromolecules 41 (24) (2008) 9650–9655. doi:10.1021/ma801718v.
URL https://doi.org/10.1021/ma801718v

[49] M. Huang, J. Yang, Facile microencapsulation of hdi for self-healing anticorrosion coatings, J. Mater. Chem. 21 (2011) 11123–11130. doi:10.1039/C1JM10794A.
URL http://dx.doi.org/10.1039/C1JM10794A

[50] D. Sun, Y. B. Chong, K. Chen, J. Yang, Chemically and thermally stable isocyanate microcapsules having good self-healing and self-lubricating performances, Chemical Engineering Journal 346 (2018) 289 – 297. doi:https://doi.org/10.1016/j.cej.2018.04.046.
URL http://www.sciencedirect.com/science/article/pii/S1385894718306107

[51] Z. He, S. Jiang, Q. Li, J. Wang, Y. Zhao, M. Kang, Facile and cost-effective synthesis of isocyanate microcapsules via polyvinyl alcohol-mediated interfacial polymerization and their application in self-healing materials, Composites Science and Technology 138 (2017) 15 – 23. doi:https://doi.org/10.1016/j.compscitech.2016.11.004.
URL http://www.sciencedirect.com/science/article/pii/S026635381630954X

[52] Z. He, S. Jiang, N. An, X. Li, Q. Li, J. Wang, Y. Zhao, M. Kang, Self-healing isocyanate microcapsules for efficient restoration of fracture damage of polyurethane and epoxy resins, Journal of Materials Science 54 (11) (2019) 8262–8275. doi:10.1007/s10853-018-03236-3.
URL https://doi.org/10.1007/s10853-018-03236-3

[53] Y. Ma, Y. Zhang, X. Liu, J. Gu, Synthesis of isocyanate microcapsules as functional crosslinking agent for wood adhesive, The Journal of Adhesion 0 (0) (2019) 1–15. doi:10.1080/00218464.2019.1625039.
URL https://doi.org/10.1080/00218464.2019.1625039

[54] G. Gody, C. Rossner, J. Moraes, P. Vana, T. Maschmeyer, S. Perrier, One-pot raft/"click" chemistry via isocyanates: Efficient synthesis of alpha-end-functionalized polymers, Journal of the American Chemical Society 134 (30) (2012) 12596–12603. doi:10.1021/ja3030643.
URL http://dx.doi.org/10.1021/ja3030643

[55] G. Gody, D. A. Roberts, T. Maschmeyer, S. Perrier, A new methodology for assessing macromolecular click reactions and its application to amine–tertiary isocyanate coupling for polymer ligation, Journal of the American Chemical Society 138 (12) (2016) 4061–4068. doi:10.1021/jacs.5b11831.
URL http://dx.doi.org/10.1021/jacs.5b11831

[56] P. Sundberg, M. Karppinen, Organic and inorganic–organic thin film structures by molecular layer deposition: A review, Beilstein Journal of Nanotechnology 5 (2014) 1104–1136. doi:10.3762/bjnano.5.123.
URL https://doi.org/10.3762/bjnano.5.123

[57] M. Müller, Q. U. Huynh, E. Uhlmann, M. H. Wagner, Study of inkjet printing as additive manufacturing process for gradient polyurethane material, Production Engineering 8 (1-2) (2014) 25–32. doi:10.1007/s11740-013-0504-0.
URL http://dx.doi.org/10.1039/s11740-013-0504-0

[58] F. Goesmann, H. Rosenbauer, J. H. Bredehöft, M. Cabane, P. Ehrenfreund, T. Gautier, C. Giri, H. Krüger, L. Le Roy, A. J. MacDermott, S. McKenna-Lawlor, U. J. Meierhenrich, G. M. M. Caro, F. Raulin, R. Roll, A. Steele, H. Steininger, R. Sternberg, C. Szopa, W. Thiemann, S. Ulamec, Organic compounds on comet 67p/churyumov-gerasimenko revealed by cosac mass spectrometry, Science 349 (6247) (2015). doi:10.1126/science.aab0689.
URL https://science.sciencemag.org/content/349/6247/aab0689

[59] L. Majumdar, J.-C. Loison, M. Ruaud, P. Gratier, V. Wakelam, A. Coutens, Methyl isocyanate (CH3NCO): an important missing organic in current astrochemical networks, Monthly Notices of the Royal Astronomical Society: Letters 473 (1) (2017) L59–L63. doi:10.1093/mnrasl/slx157.
URL https://doi.org/10.1093/mnrasl/slx157

[60] C. Schneider, S. Becker, H. Okamura, A. Crisp, T. Amatov, M. Stadlmeier, T. Carell, Noncanonical rna nucleosides as molecular fossils of an early earth—generation by prebiotic methylations and carbamoylations, Angewandte Chemie International Edition 57 (20) (2018) 5943–5946. doi:10.1002/anie.201801919.
URL https://onlinelibrary.wiley.com/doi/abs/10.1002/anie.201801919

[61] B. Maté, G. Molpeceres, I. Tanarro, R. J. Peláez, J. C. Guillemin, J. Cernicharo, V. J. Herrero, Stability of CH3nco in astronomical ices under energetic processing: A laboratory study, The Astrophysical Journal 861 (1) (2018) 61. doi:10.3847/1538-4357/aac826.
URL https://doi.org/10.3847/1538-4357/aac826

[62] A. Ciaravella, A. Jiménez-Escobar, C. Cecchi-Pestellini, C. H. Huang, N. E. Sie, G. M. M. Caro, Y. J. Chen, Synthesis of complex organic molecules in soft x-ray irradiated ices, The Astrophysical

Journal 879 (1) (2019) 21. doi:10.3847/1538-4357/ab211c.
URL https://doi.org/10.3847/1538-4357/ab211c

[63] E. Ozensoy, D. Wayne Goodman, Vibrational spectroscopic studies on co adsorption, no adsorption co + no reaction on pd model catalysts, Phys. Chem. Chem. Phys. 6 (2004) 3765–3778. doi:10.1039/B402302A.
URL http://dx.doi.org/10.1039/B402302A

[64] S. Zhao, Y. Ren, J. Wang, W. Yin, A density functional study of the interaction of nco with small copper clusters, The Journal of Physical Chemistry A 113 (6) (2009) 1075–1085, pMID: 19123856. doi:10.1021/jp8059757.
URL https://doi.org/10.1021/jp8059757

[65] X. J. Kuang, X.-Q. Wang, G.-B. Liu, All-electron scalar relativistic calculation of the adsorption of nco species onto small copper clusters, Journal of the Iranian Chemical Society 8 (3) (2011) 750–761. doi:10.1007/BF03245906.
URL https://doi.org/10.1007/BF03245906

[66] G. R. Garda, R. M. Ferullo, N. J. Castellani, Chemisorption of nco on cu(100): A density functional theory study, Surface Science 598 (1) (2005) 57 – 67. doi:https://doi.org/10.1016/j.susc.2005.09.024.
URL http://www.sciencedirect.com/science/article/pii/S0039602805010435

[67] P. G. Belelli, M. M. Branda, G. R. Garda, R. M. Ferullo, N. J. Castellani, Chemisorption of isocyanate (nco) on the pd(100) surface at different coverages, Surface Science 604 (3) (2010) 442 – 450. doi:https://doi.org/10.1016/j.susc.2009.12.014.
URL http://www.sciencedirect.com/science/article/pii/S0039602809007912

[68] S. Zhao, Y. Ren, J. Wang, W. Yin, Interaction of nco with small silver clusters: A density functional study, Journal of Molecular Structure: THEOCHEM 897 (1) (2009) 100 – 105. doi:https://doi.org/10.1016/j.theochem.2008.11.034.
URL http://www.sciencedirect.com/science/article/pii/S0166128008007197

[69] H. Deng, Y. Yu, H. He, The role of agoal entities in adsorption of nco species and reduction of nox, Catalysis Today 258 (2015) 35 – 40, catalytic science and technology in Sustainable Environment (EECAT, 2014). doi:https://doi.org/10.1016/j.cattod.2015.03.023.
URL http://www.sciencedirect.com/science/article/pii/S0920586115001844

[70] W. Cheuquepán, J. Orts, A. Rodes, J. Feliu, Dft and spectroelectrochemical study of cyanate adsorption on gold single crystal electrodes in neutral medium, Journal of Electroanalytical Chemistry 793 (2017) 147 – 156, sl:Professor Antonio Aldaz. doi:https://doi.org/10.1016/j.jelechem.2016.10.011.
URL http://www.sciencedirect.com/science/article/pii/S1572665716305318

[71] W. Cheuquepán, A. Rodes, J. M. Orts, J. M. Feliu, Formation of cyanuric acid from cyanate adsorbed at gold electrodes, Electrochemistry Communications 74 (2017) 1 – 4. doi:https://doi.org/10.1016/j.elecom.2016.11.005.
URL http://www.sciencedirect.com/science/article/pii/S1388248116302697

[72] I. Czekaj, G. Piazzesi, O. Kröcher, A. Wokaun, Dft modeling of the hydrolysis of isocyanic acid over the tio2 anatase (101) surface: Adsorption of hnco species, Surface Science 600 (24) (2006)

5158 – 5167. doi:https://doi.org/10.1016/j.susc.2006.08.037.
URL http://www.sciencedirect.com/science/article/pii/S0039602806009356

[73] I. Czekaj, O. Kröcher, Decomposition of urea in the scr process: Combination of dft calculations and experimental results on the catalytic hydrolysis of isocyanic acid on tio2 and al2o3, Topics in Catalysis 52 (13) (2009) 1740. doi:10.1007/s11244-009-9344-8.
URL https://doi.org/10.1007/s11244-009-9344-8

[74] J. Evers, B. Krumm, Q. J. Axthammer, J. Martens, P. Blaha, F. X. Steemann, T. Reith, P. Mayer, T. M. Klapötke, Molecular structure of isocyanic acid, hnco, the imide of carbon dioxide, The Journal of Physical Chemistry A 122 (12) (2018) 3287–3292, pMID: 29513983. doi:10.1021/acs.jpca.8b00557.
URL https://doi.org/10.1021/acs.jpca.8b00557

[75] M. Lowenthal, R. Khanna, M. H. Moore, Infrared spectrum of solid isocyanic acid (hnco): vibrational assignments and integrated band intensities, Spectrochimica Acta Part A: Molecular and Biomolecular Spectroscopy 58 (1) (2002) 73 – 78. doi:https://doi.org/10.1016/S1386-1425(01)00524-8.
URL http://www.sciencedirect.com/science/article/pii/S1386142501005248

[76] S. Raunier, T. Chiavassa, A. Allouche, F. Marinelli, J.-P. Aycard, Thermal reactivity of hnco with water ice: an infrared and theoretical study, Chemical Physics 288 (2) (2003) 197 – 210. doi:https://doi.org/10.1016/S0301-0104(03)00024-7.
URL http://www.sciencedirect.com/science/article/pii/S0301010403000247

[77] A. Zabardasti, M. Solimannejad, Theoretical study and aim analysis of hydrogen bonded clusters of water and isocyanic acid, Journal of Molecular Structure: THEOCHEM 819 (1) (2007) 52 – 59. doi:https://doi.org/10.1016/j.theochem.2007.05.032.
URL http://www.sciencedirect.com/science/article/pii/S0166128007003624

[78] E. Sahnoun, L. Wiesenfeld, K. Hammami, N. Jaidane, van der waals interaction of hnco and h2: Potential energy surface and rotational energy transfer, The Journal of Physical Chemistry A 122 (11) (2018) 3004–3012, pMID: 29480723. doi:10.1021/acs.jpca.8b00150.
URL https://doi.org/10.1021/acs.jpca.8b00150

[79] J. N. Gibb, J. M. Goodman, The formation of high-purity isocyanurate through proazaphosphatrane-catalysed isocyanate cyclo-trimerisation: computational insights, Org. Biomol. Chem. 11 (2013) 90–97. doi:10.1039/C2OB26547H.
URL http://dx.doi.org/10.1039/C2OB26547H

[80] J. Helberg, Y. Oe, H. Zipse, Mechanistic analysis and characterization of intermediates in the phosphane-catalyzed oligomerization of isocyanates, Chemistry – A European Journal 24 (54) (2018) 14387–14391. doi:10.1002/chem.201804016.
URL https://onlinelibrary.wiley.com/doi/abs/10.1002/chem.201804016

[81] Y.-S. Han, K.-Y. Jung, Y.-J. Kim, K. K. Baeck, G. M. Lee, S. W. Lee, Reactivities of zero-valent group 10 complexes toward organic isocyanates: synthesis of metallacycles containing dimeric isocyanate units, isocyanate cyclotrimerization, and computational chemistry, New J. Chem. (2019) –doi:10.1039/C9NJ03332G.
URL http://dx.doi.org/10.1039/C9NJ03332G

[82] W. Cheikh, Z. B. Rózsa, C. O. Camacho López, P. Mizsey, B. Viskolcz, M. Szőri, Z. Fejes, Urethane formation with an excess of isocyanate or alcohol: Experimental and ab initio study, Polymers 11 (10) (2019) 1543. doi:10.3390/polym11101543.
URL http://dx.doi.org/10.3390/polym11101543

[83] J. Kim, J. Cho, Y.-S. Lim, Bonding of urethane reactants to aluminum surface, Journal of Materials Science 40 (11) (2005) 2789–2794. doi:10.1007/s10853-005-2409-6.
URL https://doi.org/10.1007/s10853-005-2409-6

[84] S. Tardio, M.-L. Abel, R. H. Carr, J. F. Watts, The interfacial interaction between isocyanate and stainless steel, International Journal of Adhesion and Adhesives 88 (2019) 1 – 10. doi:https://doi.org/10.1016/j.ijadhadh.2018.10.008.
URL http://www.sciencedirect.com/science/article/pii/S0143749618302380

[85] R. Z. Boros, A. Rágyanszki, I. G. Csizmadia, B. Fiser, A. Guljas, L. Farkas, B. Viskolcz, Industrial application of molecular computations on the dimerization of methylene diphenyl diisocyanate, Reaction Kinetics, Mechanisms and Catalysis 124 (1) (2018) 1–14. doi:10.1007/s11144-018-1385-1.
URL https://doi.org/10.1007/s11144-018-1385-1

[86] A. N. Petelski, N. M. Peruchena, S. C. Pamies, G. L. Sosa, Insights into the self-assembly steps of cyanuric acid toward rosette motifs: a dft study, Journal of Molecular Modeling 23 (9) (2017) 263. doi:10.1007/s00894-017-3428-3.
URL https://doi.org/10.1007/s00894-017-3428-3

[87] A. N. Petelski, S. C. Pamies, A. G. Sejas, N. M. Peruchena, G. L. Sosa, Impact of confinement in multimolecular inclusion compounds of melamine and cyanuric acid, Phys. Chem. Chem. Phys. 21 (2019) 8205–8214. doi:10.1039/C8CP07705C.
URL http://dx.doi.org/10.1039/C8CP07705C

[88] W. D. Cornell, P. Cieplak, C. I. Bayly, I. R. Gould, K. M. Merz, D. M. Ferguson, D. C. Spellmeyer, T. Fox, J. W. Caldwell, P. A. Kollman, A second generation force field for the simulation of proteins, nucleic acids, and organic molecules, Journal of the American Chemical Society 117 (19) (1995) 5179–5197. doi:10.1021/ja00124a002.
URL https://dx.doi.org/10.1021/ja00124a002

[89] J. Wang, R. M. Wolf, J. W. Caldwell, P. A. Kollman, D. A. Case, Development and testing of a general amber force field, Journal of Computational Chemistry 25 (9) (2004) 1157–1174. doi:10.1002/jcc.20035.
URL http://dx.doi.org/10.1002/jcc.20035

[90] K. Vanommeslaeghe, E. Hatcher, C. Acharya, S. Kundu, S. Zhong, J. Shim, E. Darian, O. Guvench, P. Lopes, I. Vorobyov, A. D. Mackerell, Charmm general force field: A force field for drug-like molecules compatible with the charmm all-atom additive biological force fields, Journal of Computational Chemistry 31 (4) (2010) 671–690. doi:10.1002/jcc.21367.
URL http://dx.doi.org/10.1002/jcc.21367

[91] K. Vanommeslaeghe, E. Hatcher, C. Acharya, S. Kundu, S. Zhong, J. Shim, E. Darian, O. Guvench, P. Lopes, I. Vorobyov, A. D. Mackerell, Charmm general force field: A force field for drug-like molecules compatible with the charmm all-atom additive biological force fields, Journal of Computational Chemistry 31 (4) (2010) 671–690. doi:10.1002/jcc.21367.
URL http://dx.doi.org/10.1002/jcc.21367

134

[92] A. C. C. Esteves, K. Lyakhova, L. G. J. van der Ven, R. A. T. M. van Benthem, G. de With, Surface segregation of low surface energy polymeric dangling chains in a cross-linked polymer network investigated by a combined experimental–simulation approach, Macromolecules 46 (5) (2013) 1993–2002. doi:10.1021/ma302236w.
URL https://doi.org/10.1021/ma302236w

[93] A. C. C. Esteves, K. Lyakhova, J. M. van Riel, L. G. J. van der Ven, R. A. T. M. van Benthem, G. de With, Self-replenishing ability of cross-linked low surface energy polymer films investigated by a complementary experimental-simulation approach, The Journal of Chemical Physics 140 (12) (2014) 124902. doi:10.1063/1.4868989.
URL https://doi.org/10.1063/1.4868989

[94] K. Lyakhova, A. C. C. Esteves, M. W. P. van de Put, L. G. J. van der Ven, R. A. T. M. van Benthem, G. de With, Simulation-experimental approach to investigate the role of interfaces in self-replenishing composite coatings, Advanced Materials Interfaces 1 (3) (2014) 1400053. doi:10.1002/admi.201400053.
URL https://onlinelibrary.wiley.com/doi/abs/10.1002/admi.201400053

[95] E. Iype, A. C. C. Esteves, G. de With, Mesoscopic simulations of hydrophilic cross-linked polycarbonate polyurethane networks: structure and morphology, Soft Matter 12 (2016) 5029–5040. doi:10.1039/C6SM00621C.
URL http://dx.doi.org/10.1039/C6SM00621C

[96] G. Kacar, Dissipative particle dynamics simulation parameters and interactions of a hydrogel, Journal of the Turkish Chemical Society Section A: Chemistry 5 (2017) 19 – 28. doi:10.18596/jotcsa.309646.
URL http://dx.doi.org/10.18596/jotcsa.309646

[97] G. Kacar, P. T. M. Albers, A. C. C. Esteves, G. de With, Mesoscopic structure and swelling properties of crosslinked polyethylene glycol in water, Journal of Coatings Technology and Research 15 (4) (2018) 691–701. doi:10.1007/s11998-018-0065-4.
URL https://doi.org/10.1007/s11998-018-0065-4

[98] G. Kacar, E. A. J. F. Peters, G. de With, Mesoscopic simulations for the molecular and network structure of a thermoset polymer, Soft Matter 9 (2013) 5785–5793. doi:10.1039/C3SM50304F.
URL http://dx.doi.org/10.1039/C3SM50304F

[99] S. J. Marrink, H. J. Risselada, S. Yefimov, D. P. Tieleman, A. H. de Vries, The martini force field: coarse grained model for biomolecular simulations, The Journal of Physical Chemistry B 111 (27) (2007) 7812–7824, pMID: 17569554. doi:10.1021/jp071097f.
URL https://doi.org/10.1021/jp071097f

[100] H. Ghermezcheshme, H. Makki, M. Mohseni, M. Ebrahimi, G. de With, Martini-based simulation method for step-growth polymerization and its analysis by size exclusion characterization: a case study of cross-linked polyurethane, Phys. Chem. Chem. Phys. 21 (2019) 21603–21614. doi:10.1039/C9CP03407B.
URL http://dx.doi.org/10.1039/C9CP03407B

[101] W. L. Jorgensen, D. S. Maxwell, J. Tirado-Rives, Development and testing of the opls all-atom force field on conformational energetics and properties of organic liquids, Journal of the American Chemical Society 118 (45) (1996) 11225–11236. doi:10.1021/ja9621760.
URL https://dx.doi.org/10.18596/jotcsa.309646

[102] J. J. Sakurai, Modern Quantum Mechanics, 2nd Edition, Addison-Wesley, Boston, MA, USA, 2011.

[103] H. D. R., W. Hartree, Self-consistent field, with exchange, for beryllium, Proceedings of the Royal Society of London. Series A - Mathematical and Physical Sciences 150 (869) (1935) 9–33. doi:10.1098/rspa.1935.0085.
URL https://royalsocietypublishing.org/doi/abs/10.1098/rspa.1935.0085

[104] M. Born, J. R. Oppenheimer, Zur quantentheorie der molekeln, Annalen der Psysik 84 (1927) 457–484. doi:10.1002/andp.19273892002.
URL https://onlinelibrary.wiley.com/doi/abs/10.1002/andp.19273892002

[105] J. C. Slater, The theory of complex spectra, Phys. Rev. 34 (1929) 1293–1322. doi:10.1103/PhysRev.34.1293.
URL https://link.aps.org/doi/10.1103/PhysRev.34.1293

[106] C. C. J. Roothaan, New developments in molecular orbital theory, Rev. Mod. Phys. 23 (1951) 69–89. doi:10.1103/RevModPhys.23.69.
URL https://link.aps.org/doi/10.1103/RevModPhys.23.69

[107] R. Ditchfield, W. J. Hehre, J. A. Pople, Self-consistent molecular-orbital methods. ix. an extended gaussian-type basis for molecular-orbital studies of organic molecules, The Journal of Chemical Physics 54 (2) (1971) 724–728. doi:10.1063/1.1674902.
URL http://scitation.aip.org/content/aip/journal/jcp/54/2/10.1063/1.1674902

[108] M. J. Frisch, J. A. Pople, J. S. Binkley, Self-consistent molecular orbital methods 25. supplementary functions for gaussian basis sets, The Journal of Chemical Physics 80 (7) (1984) 3265–3269. doi:10.1063/1.447079.
URL http://scitation.aip.org/content/aip/journal/jcp/80/7/10.1063/1.447079

[109] T. Clark, J. Chandrasekhar, G. W. Spitznagel, P. V. R. Schleyer, Efficient diffuse function-augmented basis sets for anion calculations. iii. the 3-21+g basis set for first-row elements, li-f, Journal of Computational Chemistry 4 (3) (1983) 294–301. doi:10.1002/jcc.540040303.
URL http://dx.doi.org/10.1002/jcc.540040303

[110] T. H. Dunning, Gaussian basis sets for use in correlated molecular calculations. i. the atoms boron through neon and hydrogen, The Journal of Chemical Physics 90 (2) (1989) 1007–1023. doi:10.1063/1.456153.
URL https://doi.org/10.1063/1.456153

[111] C. Møller, M. S. Plesset, Note on an approximation treatment for many-electron systems, Phys. Rev. 46 (1934) 618–622. doi:10.1103/PhysRev.46.618.
URL https://link.aps.org/doi/10.1103/PhysRev.46.618

[112] M. Head-Gordon, J. A. Pople, M. J. Frisch, Mp2 energy evaluation by direct methods, Chemical Physics Letters 153 (6) (1988) 503 – 506. doi:https://doi.org/10.1016/0009-2614(88)85250-3.
URL http://www.sciencedirect.com/science/article/pii/0009261488852503

[113] K. Szalewicz, Symmetry-adapted perturbation theory of intermolecular forces, Wiley Interdisciplinary Reviews: Computational Molecular Science 2 (2) (2012) 254–272. doi:10.1002/wcms.86.
URL https://onlinelibrary.wiley.com/doi/abs/10.1002/wcms.86

[114] T. M. Parker, L. A. Burns, R. M. Parrish, A. G. Ryno, C. D. Sherrill, Levels of symmetry adapted perturbation theory (SAPT). I. Efficiency and performance for interaction energies, Journal of Chemical Physics 140 (9) (2014). doi:10.1063/1.4867135.
URL https://dx.doi.org/10.1063/1.4867135

[115] J. Paldus, J. Čížek, I. Shavitt, Correlation problems in atomic and molecular systems. iv. extended coupled-pair many-electron theory and its application to the bh_3 molecule, Phys. Rev. A 5 (1972) 50–67. doi:10.1103/PhysRevA.5.50.
URL https://link.aps.org/doi/10.1103/PhysRevA.5.50

[116] T. Takatani, E. G. Hohenstein, M. Malagoli, M. S. Marshall, C. D. Sherrill, Basis set consistent revision of the S22 test set of noncovalent interaction energies, Journal of Chemical Physics 132 (14) (2010). doi:10.1063/1.3378024.
URL https://dx.doi.org/10.1063/1.3378024

[117] P. Hohenberg, W. Kohn, Inhomogeneous electron gas, Phys. Rev. 136 (1964) B864–B871. doi:10.1103/PhysRev.136.B864.
URL https://link.aps.org/doi/10.1103/PhysRev.136.B864

[118] W. Kohn, L. J. Sham, Self-consistent equations including exchange and correlation effects, Phys. Rev. 140 (1965) A1133–A1138. doi:10.1103/PhysRev.140.A1133.
URL https://link.aps.org/doi/10.1103/PhysRev.140.A1133

[119] D. M. Ceperley, B. J. Alder, Ground state of the electron gas by a stochastic method, Phys. Rev. Lett. 45 (1980) 566–569. doi:10.1103/PhysRevLett.45.566.
URL https://link.aps.org/doi/10.1103/PhysRevLett.45.566

[120] Y. Wang, J. P. Perdew, Correlation hole of the spin-polarized electron gas, with exact small-wave-vector and high-density scaling, Phys. Rev. B 44 (1991) 13298–13307. doi:10.1103/PhysRevB.44.13298.
URL https://link.aps.org/doi/10.1103/PhysRevB.44.13298

[121] J. P. Perdew, K. Burke, M. Ernzerhof, Generalized gradient approximation made simple, Phys. Rev. Lett. 77 (1996) 3865–3868. doi:10.1103/PhysRevLett.77.3865.
URL https://link.aps.org/doi/10.1103/PhysRevLett.77.3865

[122] A. D. Becke, Density-functional exchange-energy approximation with correct asymptotic behavior, Phys. Rev. A 38 (1988) 3098–3100. doi:10.1103/PhysRevA.38.3098.
URL https://link.aps.org/doi/10.1103/PhysRevA.38.3098

[123] C. Lee, W. Yang, R. G. Parr, Development of the colle-salvetti correlation-energy formula into a functional of the electron density, Phys. Rev. B 37 (1988) 785–789. doi:10.1103/PhysRevB.37.785.
URL https://link.aps.org/doi/10.1103/PhysRevB.37.785

[124] S. H. Vosko, L. Wilk, M. Nusair, Accurate spin-dependent electron liquid correlation energies for local spin density calculations: a critical analysis, Canadian Journal of Physics 58 (8) (1980) 1200–1211. doi:10.1139/p80-159.
URL https://doi.org/10.1139/p80-159

[125] S. Grimme, J. Antony, S. Ehrlich, H. Krieg, A consistent and accurate ab initio parametrization of density functional dispersion correction (dft-d) for the 94 elements h-pu, The Journal of Chemical Physics 132 (15) (2010) 1–19. doi:10.1063/1.3382344.
URL http://scitation.aip.org/content/aip/journal/jcp/132/15/10.1063/1.3382344

[126] S. Grimme, S. Ehrlich, L. Goerigk, Effect of the damping function in dispersion corrected density functional theory, Journal of Computational Chemistry 32 (7) (2011) 1456–1465. doi:10.1002/jcc.21759.
URL http://dx.doi.org/10.1002/jcc.21759

[127] E. R. Johnson, S. Keinan, P. Mori-Sánchez, J. Contreras-García, A. J. Cohen, W. Yang, Revealing noncovalent interactions, Journal of the American Chemical Society 132 (18) (2010) 6498–6506, pMID: 20394428. doi:10.1021/ja100936w.
URL https://doi.org/10.1021/ja100936w

[128] C. Narth, Z. Maroun, R. A. Boto, R. Chaudret, M.-L. Bonnet, J.-P. Piquemal, J. Contreras-García, A complete NCI perspective: From New Bonds to Reactivity, Applications of Topological Methods in Molecular Chemistry (2016) 491–527doi:10.1007/978-3-319-29022-5_18.
URL http://link.springer.com/10.1007/978-3-319-29022-5

[129] Multiwfn, a multifunctional wavefunction analyzer, last time visited: 27th July 2018.
URL http://sobereva.com/multiwfn/

[130] F. Bloch, Über die quantenmechanik der elektronen in kristallgittern, Zeitschrift für Physik 52 (7) (1929) 555–600. doi:10.1007/BF01339455.
URL https://doi.org/10.1007/BF01339455

[131] C. Herring, A new method for calculating wave functions in crystals, Phys. Rev. 57 (1940) 1169–1177. doi:10.1103/PhysRev.57.1169.
URL https://link.aps.org/doi/10.1103/PhysRev.57.1169

[132] J. C. Phillips, L. Kleinman, New method for calculating wave functions in crystals and molecules, Phys. Rev. 116 (1959) 287–294. doi:10.1103/PhysRev.116.287.
URL https://link.aps.org/doi/10.1103/PhysRev.116.287

[133] E. Antončík, The use of the repulsive potential in the quantum theory of solids, Cechoslovackij fiziceskij zurnal 9 (3) (1959) 291–305. doi:10.1007/BF01557187.
URL https://doi.org/10.1007/BF01557187

[134] Wikipedia contributors, Pseudopotential — Wikipedia, the free encyclopedia, [Online; accessed 28-November-2019] (2019).
URL https://en.wikipedia.org/w/index.php?title=Pseudopotential&oldid=918334982

[135] D. R. Hamann, M. Schlüter, C. Chiang, Norm-conserving pseudopotentials, Phys. Rev. Lett. 43 (1979) 1494–1497. doi:10.1103/PhysRevLett.43.1494.
URL https://link.aps.org/doi/10.1103/PhysRevLett.43.1494

[136] G. B. Bachelet, D. R. Hamann, M. Schlüter, Pseudopotentials that work: From h to pu, Phys. Rev. B 26 (1982) 4199–4228. doi:10.1103/PhysRevB.26.4199.
URL https://link.aps.org/doi/10.1103/PhysRevB.26.4199

[137] D. Vanderbilt, Soft self-consistent pseudopotentials in a generalized eigenvalue formalism, Phys. Rev. B 41 (1990) 7892–7895. doi:10.1103/PhysRevB.41.7892.
URL https://link.aps.org/doi/10.1103/PhysRevB.41.7892

[138] P. E. Blöchl, Projector augmented-wave method, Phys. Rev. B 50 (1994) 17953–17979. doi:10.1103/PhysRevB.50.17953.
URL https://link.aps.org/doi/10.1103/PhysRevB.50.17953

[139] M. J. Frisch, G. W. Trucks, H. B. Schlegel, G. E. Scuseria, M. A. Robb, J. R. Cheeseman, G. Scalmani, V. Barone, B. Mennucci, G. A. Petersson, H. Nakatsuji, M. Caricato, X. Li, H. P. Hratchian, A. F. Izmaylov, J. Bloino, G. Zheng, J. L. Sonnenberg, M. Hada, M. Ehara, K. Toyota, R. Fukuda, J. Hasegawa, M. Ishida, T. Nakajima, Y. Honda, O. Kitao, H. Nakai, T. Vreven, J. A. Montgomery, Jr., J. E. Peralta, F. Ogliaro, M. Bearpark, J. J. Heyd, E. Brothers, K. N. Kudin, V. N. Staroverov, R. Kobayashi, J. Normand, K. Raghavachari, A. Rendell, J. C. Burant, S. S. Iyengar, J. Tomasi, M. Cossi, N. Rega, J. M. Millam, M. Klene, J. E. Knox, J. B. Cross, V. Bakken, C. Adamo, J. Jaramillo, R. Gomperts, R. E. Stratmann, O. Yazyev, A. J. Austin, R. Cammi, C. Pomelli, J. W. Ochterski, R. L. Martin, K. Morokuma, V. G. Zakrzewski, G. A. Voth, P. Salvador, J. J. Dannenberg, S. Dapprich, A. D. Daniels, Ö. Farkas, J. B. Foresman, J. V. Ortiz, J. Cioslowski, D. J. Fox, Gaussian '09 Revision E.01, gaussian Inc. Wallingford CT (2009).

[140] R. M. Parrish, L. A. Burns, D. G. A. Smith, A. C. Simmonett, A. E. DePrince, E. G. Hohenstein, U. Bozkaya, A. Y. Sokolov, R. Di Remigio, R. M. Richard, J. F. Gonthier, A. M. James, H. R. McAlexander, A. Kumar, M. Saitow, X. Wang, B. P. Pritchard, P. Verma, H. F. Schaefer, K. Patkowski, R. A. King, E. F. Valeev, F. A. Evangelista, J. M. Turney, T. D. Crawford, C. D. Sherrill, Psi4 1.1: An open-source electronic structure program emphasizing automation, advanced libraries, and interoperability, Journal of Chemical Theory and Computation 13 (7) (2017) 3185–3197. doi:10.1021/acs.jctc.7b00174.
URL https://doi.org/10.1021/acs.jctc.7b00174

[141] G. Kresse, J. Furthmüller, Efficient iterative schemes for ab initio total-energy calculations using a plane-wave basis set, Phys. Rev. B 54 (1996) 11169–11186. doi:10.1103/PhysRevB.54.11169.
URL https://link.aps.org/doi/10.1103/PhysRevB.54.11169

[142] G. Kresse, D. Joubert, From ultrasoft pseudopotentials to the projector augmented-wave method, Phys. Rev. B 59 (1999) 1758–1775. doi:10.1103/PhysRevB.59.1758.
URL https://link.aps.org/doi/10.1103/PhysRevB.59.1758

[143] S. Gražulis, A. Daškevič, A. Merkys, D. Chateigner, L. Lutterotti, M. Quirós, N. R. Serebryanaya, P. Moeck, R. T. Downs, A. Le Bail, Crystallography open database (cod): an open-access collection of crystal structures and platform for world-wide collaboration, Nucleic Acids Research 40 (D1) (2012) D420–D427. doi:10.1093/nar/gkr900.
URL http://nar.oxfordjournals.org/content/40/D1/D420.abstract

[144] P. P. Ewald, Die berechnung optischer und elektrostatischer gitterpotentiale, Annalen der Physik 369 (3) (1921) 253–287. doi:10.1002/andp.19213690304.
URL http://dx.doi.org/10.1002/andp.19213690304

[145] S. J. Plimpton, R. Pollock, M. Stevens, Particle-mesh ewald and rrespa for parallel molecular dynamics simulations, in: PPSC, 1997.

[146] R. E. Isele-Holder, W. Mitchell, A. E. Ismail, Development and application of a particle-particle particle-mesh ewald method for dispersion interactions, The Journal of Chemical Physics 137 (17) (2012) 174107. doi:10.1063/1.4764089.
URL https://doi.org/10.1063/1.4764089

[147] M. Tuckerman, B. J. Berne, G. J. Martyna, Reversible multiple time scale molecular dynamics, The Journal of Chemical Physics 97 (3) (1992) 1990–2001. doi:10.1063/1.463137.
URL http://scitation.aip.org/content/aip/journal/jcp/97/3/10.1063/1.463137

[148] K. Huang, Statistical Mechanics, 2nd Edition, Wiley, Hoboken, NY, USA, 1987.

[149] W. G. Hoover, Canonical dynamics: Equilibrium phase-space distributions, Physycal Review A 31 (1985) 1695–1697. doi:10.1103/PhysRevA.31.1695.
URL http://link.aps.org/doi/10.1103/PhysRevA.31.1695

[150] C. J. Dickson, L. Rosso, R. M. Betz, R. C. Walker, I. R. Gould, GAFFlipid: a General Amber Force Field for the accurate molecular dynamics simulation of phospholipid, Soft Matter 8 (2012) 9617. doi:10.1039/c2sm26007g.

[151] C. Caleman, P. J. van Maaren, M. Hong, J. S. Hub, L. T. Costa, D. van der Spoel, Force field benchmark of organic liquids: Density, enthalpy of vaporization, heat capacities, surface tension, isothermal compressibility, volumetric expansion coefficient, and dielectric constant, Journal of Chemical Theory and Computation 8 (1) (2012) 61–74. doi:10.1021/ct200731v.

[152] N. J. Boyd, M. R. Wilson, Optimization of the GAFF force field to describe liquid crystal molecules: the path to a dramatic improvement in transition temperature predictions, Physical Chemistry Chemical Physics 17 (38) (2015) 24851–24865. doi:10.1039/C5CP03702F.
URL http://xlink.rsc.org/?DOI=C5CP03702F

[153] K. G. Sprenger, V. W. Jaeger, J. Pfaendtner, The general amber force field (gaff) can accurately predict thermodynamic and transport properties of many ionic liquids, The Journal of Physical Chemistry B 119 (18) (2015) 5882–5895. doi:10.1021/acs.jpcb.5b00689.
URL http://dx.doi.org/10.1021/acs.jpcb.5b00689

[154] G. A. Ozpinar, W. Peukert, T. Clark, An improved generalized AMBER force field (GAFF) for urea, Journal of Molecular Modeling 16 (9) (2010) 1427–1440. doi:10.1007/s00894-010-0650-7.
URL https://dx.doi.org/10.1007/s00894-010-0650-7

[155] R. Woods, R. Chappelle, Restrained electrostatic potential atomic partial charges for condensed-phase simulations of carbohydrates, Journal of Molecular Structure: THEOCHEM 527 (1) (2000) 149 – 156. doi:https://doi.org/10.1016/S0166-1280(00)00487-5.
URL http://www.sciencedirect.com/science/article/pii/S0166128000004875

[156] S. Plimpton, Fast parallel algorithms for short-range molecular dynamics, Journal of Computational Physics 117 (1) (1995) 1 – 19. doi:10.1006/jcph.1995.1039.
URL http://www.sciencedirect.com/science/article/pii/S002199918571039X

[157] D. C. Rapaport, The Art of Molecular Dynamics Simulation, 2nd Edition, Cambridge University Press, New York, NY, USA, 2004.

[158] J. Wang, T. Hou, Application of molecular dynamics simulations in molecular property prediction. 1. density and heat of vaporization, Journal of Chemical Theory and Computation 7 (7) (2011) 2151–2165. doi:10.1021/ct200142z.
URL http://dx.doi.org/10.1021/ct200142z

[159] C. A. Angell, Formation of glasses from liquids and biopolymers, Science 267 (5206) (1995) 1924–1935. doi:10.1126/science.267.5206.1924.
URL http://science.sciencemag.org/content/267/5206/1924

[160] R. Kubo, Statistical-mechanical theory of irreversible processes. i. general theory and simple applications to magnetic and conduction problems, Journal of the Physical Society of Japan 12 (6)

(1957) 570–586. doi:10.1143/JPSJ.12.570.
URL `https://doi.org/10.1143/JPSJ.12.570`

[161] J.-P. Hansen, I. R. Macdonald, Theory of Simple Liquids, 4th Edition, Academic Press, Oxford, UK, 2013.

[162] M. E. Tuckerman, Statistical Mechanics Theory and Molecular Simulation, 1st Edition, Oxford University Press, Oxford, UK, 2010.

[163] P. J. Daivis, D. J. Evans, Comparison of constant pressure and constant volume nonequilibrium simulations of sheared model decane, The Journal of Chemical Physics 100 (1) (1994) 541–547. doi:10.1063/1.466970.
URL `http://scitation.aip.org/content/aip/journal/jcp/100/1/10.1063/1.466970`

[164] E. Darve, D. Rodríguez-Gómez, A. Pohorille, Adaptive biasing force method for scalar and vector free energy calculations, The Journal of Chemical Physics 128 (14) (2008) 144120. doi:10.1063/1.2829861.
URL `https://doi.org/10.1063/1.2829861`

[165] G. Fiorin, M. Klein, J. Hénin, Using collective variables to drive molecular dynamics simulations, Molecular Physics (2013). doi:10.1080/00268976.2013.813594.

[166] E. Carter, G. Ciccotti, J. T. Hynes, R. Kapral, Constrained reaction coordinate dynamics for the simulation of rare events, Chemical Physics Letters 156 (5) (1989) 472 – 477. doi:https://doi.org/10.1016/S0009-2614(89)87314-2.
URL `http://www.sciencedirect.com/science/article/pii/S0009261489873142`

[167] P.-G. De Gennes, Scaling concepts in polymer physics, Cornell University Press, Ithaca, NY, USA, 1979.

[168] R. Auhl, R. Everaers, G. S. Grest, K. Kremer, S. J. Plimpton, Equilibration of long chain polymer melts in computer simulations, The Journal of Chemical Physics 119 (24) (2003) 12718–12728. doi:10.1063/1.1628670.
URL `https://doi.org/10.1063/1.1628670`

[169] R. Everaers, S. K. Sukumaran, G. S. Grest, C. Svaneborg, A. Sivasubramanian, K. Kremer, Rheology and microscopic topology of entangled polymeric liquids, Science 303 (5659) (2004) 823–826. doi:10.1126/science.1091215.
URL `https://science.sciencemag.org/content/303/5659/823`

[170] M. Kröger, Shortest multiple disconnected path for the analysis of entanglements in two- and three-dimensional polymeric systems, Computer Physics Communications 168 (3) (2005) 209 – 232. doi:https://doi.org/10.1016/j.cpc.2005.01.020.
URL `http://www.sciencedirect.com/science/article/pii/S0010465505002808`

[171] S. Shanbhag, M. Kröger, Primitive path networks generated by annealing and geometrical methods: insights into differences, Macromolecules 40 (8) (2007) 2897–2903. doi:10.1021/ma062457k.
URL `https://doi.org/10.1021/ma062457k`

[172] N. C. Karayiannis, M. Kröger, Combined molecular algorithms for the generation, equilibration and topological analysis of entangled polymers: Methodology and performance, International Journal

of Molecular Sciences 10 (11) (2009) 5054–5089. doi:10.3390/ijms10115054.
URL `https://www.mdpi.com/1422-0067/10/11/5054`

[173] R. S. Hoy, K. Foteinopoulou, M. Kröger, Topological analysis of polymeric melts: Chain-length effects and fast-converging estimators for entanglement length, Phys. Rev. E 80 (2009) 031803. doi:10.1103/PhysRevE.80.031803.
URL `https://link.aps.org/doi/10.1103/PhysRevE.80.031803`

[174] W. W. Graessley, Polymeric Liquids and Networks: Dynamics and Rheology, Garland Science, Oxford, UK, 2008.

[175] P. J. Hoogerbrugge, J. M. V. A. Koelman, Simulating microscopic hydrodynamic phenomena with dissipative particle dynamics, Europhysics Letters (EPL) 19 (3) (1992) 155–160. doi:10.1209/0295-5075/19/3/001.
URL `https://doi.org/10.1209/0295-5075/19/3/001`

[176] P. Español, P. Warren, Statistical mechanics of dissipative particle dynamics, Europhysics Letters (EPL) 30 (4) (1995) 191–196. doi:10.1209/0295-5075/30/4/001.
URL `https://doi.org/10.1209/0295-5075/30/4/F001`

[177] R. D. Groot, P. B. Warren, Dissipative particle dynamics: Bridging the gap between atomistic and mesoscopic simulation, The Journal of Chemical Physics 107 (11) (1997) 4423–4435. doi:10.1063/1.474784.
URL `https://doi.org/10.1063/1.474784`

[178] T. Sirk, Y. Sliozberg, J. Brennan, M. Lisal, J. Andzelm, An enhanced entangled polymer model for dissipative particle dynamics, J. Chem. Phys. 136 (2012) 134903.

[179] J. H. Hildebrand, R. L. Scott, The solubility of Nonelectrolytes, Reinhold Publishing Group, New York, 1950.

[180] E. Mayoral, A. G. Goicochea, Modeling the temperature dependent interfacial tension between organic solvents and water using dissipative particle dynamics, The Journal of Chemical Physics 138 (9) (2013) 094703. doi:10.1063/1.4793742.
URL `https://doi.org/10.1063/1.4793742`

[181] P. Español, P. B. Warren, Perspective: Dissipative particle dynamics, The Journal of Chemical Physics 146 (15) (2017) 150901. doi:10.1063/1.4979514.
URL `https://doi.org/10.1063/1.4979514`

[182] E. R. Duering, K. Kremer, G. S. Grest, Structure and relaxation of end‐linked polymer networks, The Journal of Chemical Physics 101 (9) (1994) 8169–8192. doi:10.1063/1.468202.
URL `https://doi.org/10.1063/1.468202`

[183] L. Rovigatti, N. Gnan, L. Tavagnacco, A. J. Moreno, E. Zaccarelli, Numerical modelling of non-ionic microgels: an overview, Soft Matter 15 (2019) 1108–1119. doi:10.1039/C8SM02089B.
URL `http://dx.doi.org/10.1039/C8SM02089B`

[184] A. J. Moreno, F. Lo Verso, Computational investigation of microgels: synthesis and effect of the microstructure on the deswelling behavior, Soft Matter 14 (2018) 7083–7096. doi:10.1039/C8SM01407H.
URL `http://dx.doi.org/10.1039/C8SM01407H`

[185] V. Lenzi, P. J. Driest, D. J. Dijkstra, M. M. D. Ramos, L. S. A. Marques, Gaff-ic: realistic viscosities for isocyanate molecules with a gaff-based force field, Molecular Simulation 45 (3) (2019) 207–214. doi:10.1080/08927022.2018.1554902.
URL https://doi.org/10.1080/08927022.2018.1554902

[186] European chemicals agency (2018).
URL https://echa.europa.eu

[187] M. Ludewig, J. Weikard, N. Stockel, Allophanate-containing modified polyurethanes, uS Patent App. 11/369,483 (Sep. 14 2006).
URL https://www.google.com/patents/US20060205911

[188] C. Dieris, H. Mertes, J. Pedain, F. Richter, Isocyanattrimerisate und isocyanattrimerisatmischungen, deren herstellung und verwendung, eP Patent 0,798,299 (Aug. 27 2003).
URL https://www.google.com/patents/EP0798299B1?cl=it

[189] S. P. Verevkin, D. H. Zaitsau, V. N. Emel'Yanenko, A. V. Yermalayeu, C. Schick, H. Liu, E. J. Maginn, S. Bulut, I. Krossing, R. Kalb, Making Sense of Enthalpy of Vaporization Trends for Ionic Liquids: New Experimental and Simulation Data Show a Simple Linear Relationship and Help Reconcile Previous Data, Journal of Physical Chemistry B 117 (21) (2013) 6473–6486. doi:10.1021/jp311429r.
URL https://dx.doi.org/10.1021/jp311429r

[190] C. J. Dickson, B. D. Madej, Å. A. Skjevik, R. M. Betz, K. Teigen, I. R. Gould, R. C. Walker, Lipid14: The Amber Lipid Force Field., Journal of chemical theory and computation 10 (2) (2014) 865–879. doi:10.1021/ct4010307.
URL http://dx.doi.org/10.1021/ct4010307

[191] L. I. Berger, M. Frenkel, C. A. Koh, P. E. Bradley, J. R. Fuhr, W. H. Koppenol, T. J. Bruno, CRC Handbook of Chemistry and Physics, 95th Edition, CRC Press, Boca Raton, FL, USA, 2014.

[192] J. S. Chickos, W. E. Acree, Enthalpies of vaporization of organic and organometallic compounds, 1880-2002, Journal of Physical and Chemical Reference Data 32 (2) (2003) 519–878. doi:10.1063/1.1529214.

[193] Cheméo - high quality chemical properties (2018).
URL www.chemeo.com

[194] Chemspider - search and share chemistry (2018).
URL www.chemspider.com

[195] I. Leontyev, A. Stuchebrukhov, Accounting for electronic polarization in non-polarizable force fields., Physical Chemistry Chemical Physics 13 (7) (2011) 2613–2626. doi:10.1039/c0cp01971b.

[196] B. Zhmud, Viscosity blending equations, Lube Magazine 121 (2014) 22–27.
URL http://www.lube-media.com/wp-content/uploads/2017/11/Lube-Tech093-ViscosityBlendingEquations.pdf

[197] L. Grunberg, A. H. Nissan, The energies of vaporisation, viscosity and cohesion and the structure of liquids, Trans. Faraday Soc. 45 (1949) 125–137. doi:10.1039/TF9494500125.
URL http://dx.doi.org/10.1039/TF9494500125

[198] W. Marczak, N. Adamczyk, M. Łeżniak, Viscosity of associated mixtures approximated by the grunberg-nissan model, International Journal of Thermophysics 33 (4) (2012) 680–691. doi:10.1007/s10765-011-1100-1.
URL `https://doi.org/10.1007/s10765-011-1100-1`

[199] Z. Shi, P. G. Debenedetti, F. H. Stillinger, Relaxation processes in liquids: Variations on a theme by stokes and einstein, The Journal of Chemical Physics 138 (12) (2013) 12A526. doi:10.1063/1.4775741.
URL `https://doi.org/10.1063/1.4775741`

[200] D. A. Turton, K. Wynne, Stokes–einstein–debye failure in molecular orientational diffusion: Exception or rule?, The Journal of Physical Chemistry B 118 (17) (2014) 4600–4604. doi:10.1021/jp5012457.
URL `http://dx.doi.org/10.1021/jp5012457`

[201] L. Zhang, M. L. Greenfield, Relaxation time, diffusion, and viscosity analysis of model asphalt systems using molecular simulation, The Journal of Chemical Physics 127 (19) (2007). doi:10.1063/1.2799189.
URL `http://scitation.aip.org/content/aip/journal/jcp/127/19/10.1063/1.2799189`

[202] V. Lenzi, P. J. Driest, D. J. Dijkstra, M. M. Ramos, L. S. Marques, Investigation on the intermolecular interactions in aliphatic isocyanurate liquids: revealing the importance of dispersion, Journal of Molecular Liquids 280 (2019) 25 – 33. doi:https://doi.org/10.1016/j.molliq.2019.01.165.
URL `http://www.sciencedirect.com/science/article/pii/S0167732218359555`

[203] P. Jurečka, J. Šponer, J. Černý, P. Hobza, Benchmark database of accurate (MP2 and CCSD(T) complete basis set limit) interaction energies of small model complexes, DNA base pairs, and amino acid pairs, Physical Chemistry Chemical Physics 8 (17) (2006) 1985–1993. doi:10.1039/B600027D.
URL `http://xlink.rsc.org/?DOI=B600027D`

[204] A. H. Castro Neto, F. Guinea, N. M. R. Peres, K. S. Novoselov, A. K. Geim, The electronic properties of graphene, Reviews of Modern Physics 81 (1) (2009) 109–162. doi:10.1103/revmodphys.81.109.
URL `http://dx.doi.org/10.1103/RevModPhys.81.109`

[205] D. D. Chronopoulos, A. Bakandritsos, M. Pykal, R. Zbořil, M. Otyepka, Chemistry, properties, and applications of fluorographene, Applied Materials Today 9 (2017) 60 – 70. doi:https://doi.org/10.1016/j.apmt.2017.05.004.
URL `http://www.sciencedirect.com/science/article/pii/S2352940717301129`

[206] H. Y. Liu, Z. F. Hou, C. H. Hu, Y. Yang, Z. Z. Zhu, Electronic and magnetic properties of fluorinated graphene with different coverage of fluorine, The Journal of Physical Chemistry C 116 (34) (2012) 18193–18201. doi:10.1021/jp303279r.
URL `https://doi.org/10.1021/jp303279r`

[207] Q. Weng, G. Li, X. Feng, K. Nielsch, D. Golberg, O. G. Schmidt, Electronic and optical properties of 2d materials constructed from light atoms, Advanced Materials 30 (46) (2018) 1801600. doi:10.1002/adma.201801600.
URL `https://onlinelibrary.wiley.com/doi/abs/10.1002/adma.201801600`

144

[208] M. Zelisko, Y. Hanlumyuang, S. Yang, Y. Liu, C. Lei, J. Li, P. M. Ajayan, P. Sharma, Anomalous piezoelectricity in two-dimensional graphene nitride nanosheets, Nature Communications 5 (2014). doi:10.1038/ncomms5284.
URL https://doi.org/10.1038/ncomms5284

[209] X. Li, A. F. Masters, T. Maschmeyer, Polymeric carbon nitride for solar hydrogen production, Chem. Commun. 53 (2017) 7438–7446. doi:10.1039/C7CC02532G.
URL http://dx.doi.org/10.1039/C7CC02532G

[210] Z. Zhou, Y. Zhang, Y. Shen, S. Liu, Y. Zhang, Molecular engineering of polymeric carbon nitride: advancing applications from photocatalysis to biosensing and more, Chem. Soc. Rev. 47 (2018) 2298–2321. doi:10.1039/C7CS00840F.
URL http://dx.doi.org/10.1039/C7CS00840F

[211] V. Georgakilas, J. N. Tiwari, K. C. Kemp, J. A. Perman, A. B. Bourlinos, K. S. Kim, R. Zboril, Noncovalent functionalization of graphene and graphene oxide for energy materials, biosensing, catalytic, and biomedical applications, Chemical Reviews 116 (9) (2016) 5464–5519, pMID: 27033639. doi:10.1021/acs.chemrev.5b00620.
URL https://doi.org/10.1021/acs.chemrev.5b00620

[212] G. Bottari, M. n. Herranz, L. Wibmer, M. Volland, L. Rodríguez-Pérez, D. M. Guldi, A. Hirsch, N. Martín, F. D'Souza, T. Torres, Chemical functionalization and characterization of graphene-based materials, Chem. Soc. Rev. 46 (2017) 4464–4500. doi:10.1039/C7CS00229G.
URL http://dx.doi.org/10.1039/C7CS00229G

[213] M. Deifallah, P. F. McMillan, F. Corà, Electronic and structural properties of two-dimensional carbon nitride graphenes, The Journal of Physical Chemistry C 112 (14) (2008) 5447–5453. doi:10.1021/jp711483t.
URL https://doi.org/10.1021/jp711483t

[214] L. M. Azofra, D. R. MacFarlane, C. Sun, A dft study of planar vs. corrugated graphene-like carbon nitride (g-c3n4) and its role in the catalytic performance of co2 conversion, Phys. Chem. Chem. Phys. 18 (2016) 18507–18514. doi:10.1039/C6CP02453J.
URL http://dx.doi.org/10.1039/C6CP02453J

[215] H.-Z. Wu, L.-M. Liu, S.-J. Zhao, The effect of water on the structural, electronic and photocatalytic properties of graphitic carbon nitride, Phys. Chem. Chem. Phys. 16 (2014) 3299–3304. doi:10.1039/C3CP54333A.
URL http://dx.doi.org/10.1039/C3CP54333A

[216] I. B. Bersuker, Pseudo-jahn–teller effect—a two-state paradigm in formation, deformation, and transformation of molecular systems and solids, Chemical Reviews 113 (3) (2013) 1351–1390, pMID: 23301718. doi:10.1021/cr300279n.
URL https://doi.org/10.1021/cr300279n

[217] J. Coutinho, V. J. B. Torres, K. Demmouche, S. Öberg, Theory of the carbon vacancy in $4h$-sic: Crystal field and pseudo-jahn-teller effects, Phys. Rev. B 96 (2017) 174105. doi:10.1103/PhysRevB.96.174105.
URL https://link.aps.org/doi/10.1103/PhysRevB.96.174105

[218] G. R. Desiraju, C–h□o and other weak hydrogen bonds. from crystal engineering to virtual screening, Chem. Commun. (2005) 2995–3001doi:10.1039/B504372G.
URL http://dx.doi.org/10.1039/B504372G

[219] V. R. Thalladi, A. K. Katz, H. L. Carrell, A. Nangia, G. R. Desiraju, Trimethyl Isocyanurate and Triethyl Isocyanurate, Acta Crystallographica Section C 54 (1) (1998) 86–89. doi:10.1107/S010827019701384X.
URL https://doi.org/10.1107/S010827019701384X

[220] S. Nikolov, A. Fernandez-Nieves, A. Alexeev, Mesoscale modeling of microgel mechanics and kinetics through the swelling transition, Applied Mathematics and Mechanics (English Edition) 39 (1) (2018) 47–62. doi:10.1007/s10483-018-2259-6.
URL https://doi.org/10.1007/s10483-018-2259-6

[221] P. J. Flory, J. Rehner, Statistical mechanics of cross□linked polymer networks ii. swelling, The Journal of Chemical Physics 11 (11) (1943) 521–526. doi:10.1063/1.1723792.
URL https://doi.org/10.1063/1.1723792

Appendix A

GAFF-IC parameters

Below are listed all the GAFF-IC force-field parameters. Partial charges are not provided, since they should be obtained from ab-initio calculations by using RESP method. A MOL2 file containing the specifications for an HDI molecule is provided at the end of this document, where RESP partial charges are reported.

Atom types and non-bonded parameters

LJ parameters for the atom types appearing in isocyanates. The source of the parameters is also reported: GAFF-IC is this work, GAFFLipid is from Dickson et al.[150], default means the GAFF standard values.

Atom type	Mass [amu]	σ [Å]	ϵ [kcal/mol]	comment (source)
n2	14.010	1.795	0.155	N in isocyanate (GAFF-IC)
c1	12.010	1.874	0.155	C in isocyanate (GAFF-IC)
o	16.000	1.632	0.175	O in isocyanurate/isocyanate (GAFF-IC)
c3	12.010	2.010	0.055	sp3 carbon (GAFFlipid)
hc	1.008	1.340	0.024	hydrogen in -CH3- (GAFFlipid)
h1	1.008	1.340	0.024	hydrogen in -CH2- (GAFFlipid)
c	12.010	1.908	0.086	sp2 C in isocyanurate (default)
n	14.010	1.824	0.175	sp2 N in isocyanurate (default)

Bond parameters

All bond equilibrium lengths were adjusted to match the B3LYP-6311++G(d,p) calculations. The bond energy term in the force field is:

$$E_{bond} = \frac{k_b}{2}\left(r_{ij} - b_0\right)^2$$

Bond	k_b [kcal/(mol·Å^2)]	b_0 [Å]
c - n	478.20	1.379
c - o	648.00	1.200
n - c3	330.60	1.478
c3 - h1	335.90	1.095
c3 - c3	303.10	1.525
c3 - hc	337.30	1.096
c3 - n2	313.80	1.450
n2 - c1	769.80	1.199
c1 - o	777.00	1.171

Angle parameters

All equilibrium angle values were adjusted to match the B3LYP-6311++G(d,p) calculations. The angle energy term in the force field is:

$$E_{angle} = \frac{k_a}{2} \left(\theta_{ijk} - \theta_0 \right)^2$$

angle	k_a [kcal/(mol·rad^2)]	θ_0 [deg]]
c - n - c	65.33	124.13
c - n - c3	63.92	118.02
n - c - o	75.83	122.03
n - c - n	74.80	115.80
n - c3 - h1	49.82	112.32
n - c3 - c3	65.85	112.13
n - cc - n2	74.78	122.59
c3 - c3 - hc	46.37	109.50
c3 - c3 - c3	63.21	112.69
h1 - c3 - h1	39.18	109.55
h1 - c3 - c3	46.36	110.20
hc - c3 - hc	39.43	106.25
c3 - c3 - n2	66.40	113.13
c3 - n2 - c1	58.67	138.85
h1 - c3 - n2	49.26	109.01
n2 - c1 - o	69.15	173.76

Dihedral parameters

All dihedral values were refitted as described in the main text. The dihedral energy term of the force field is:

$$V_{dihe}(\phi) = \sum_{i=1}^{4} V_i \left[1 + cos\left(i\phi + \delta_i\right)\right]$$

Dihedral	i	V_i [kcal/mol]	δ_i [degrees]
c -n -c -n	2	25.0000	180
c -n -c -o	2	25.0000	180
c -n -c3-c3	4	-0.1439	0
c -n -c3-c3	2	0.3789	0
n -c -n -c3	2	25.0000	180
n -c3-c3-hc	3	0.1353	0
n -c3-c3-c3	4	0.0106	180
n -c3-c3-c3	3	0.1393	0
n -c3-c3-c3	2	-0.0779	180
n -c3-c3-c3	1	-0.4949	0
o -c -n -c	2	25.0000	180
c3-c3-c3-hc	3	0.1392	0
h1-c3-c3-hc	3	0.1827	0
h1-c3-c3-c3	3	0.1827	0
hc-c3-c3-hc	3	0.1392	0
c3-c3-c3-c3	4	-0.0751	180
c3-c3-c3-c3	3	0.1392	0
c3-c3-c3-c3	2	-0.1686	180
c3-c3-c3-c3	1	0.3456	0
c3-c3-c3-n2	4	-0.0493	0
c3-c3-c3-n2	3	0.1827	0
c3-c3-c3-n2	2	-0.1918	180
c3-c3-c3-n2	1	-0.0956	0
c3-c3-n2-c1	3	0.0000	0
hc-c3-c3-n2	3	0.1827	0
c3-n2-c1-o	2	0.0000	0
h1-c3-n2-c1	3	0.0000	0